# MICROMACHINED MAGNETOELASTIC SENSORS AND ACTUATORS FOR BIOMEDICAL DEVICES AND OTHER APPLICATIONS

By

Venkatram Pepakayala

A dissertation submitted in partial fulfilment
of the requirements for the degree of
Doctor of Philosophy
(Electrical Engineering)
in the University of Michigan
2015

Doctoral Committee:

Professor Yogesh B. Gianchandani, Chair
Assistant Research Scientist Scott Ryan Green
Associate Professor Kenn Richard Oldham
Associate Professor Jaesung Park, Pohang University of Science and Technology
Associate Professor Mina Raeiszadeh
Associate Professor Joshua D. Stein

*To my parents, my brother, and my wife.*

## ACKNOWLEDGEMENTS

The work described by this dissertation was funded in part by the United States Food and Drug Administration (FDA), the University of Michigan, and the National Institutes of Health (NIH). Samples for this work were provided by Metglas Inc. and Arnold Magnetic Technologies. Some fabrication and experimental measurements were performed at the Lurie Nanofabrication Facility (LNF), operated by the Solid State Electronics Laboratory (SSEL) and the University of Michigan, and at the Electron Microbeam Analysis Laboratory (EMAL) operated by the University of Michigan. Fabrication assistance was provided by Dr. Yutao Qin and Ms. Yushu Ma.

I would like to thank the committee members for their constructive criticism and suggestions for this research and the dissertation. I am grateful to the Dr. Scott Green for his eagerness and enthusiasm in sharing his considerable knowledge and expertise, and for his constant guidance over the many years I had the pleasure of working with him. Dr. Joshua Stein's knowledge was imperative for the development of the actuators as described in this work, and I am grateful for having the opportunity to work with him. As Chair of the committee and advisor for my doctoral research, Prof. Yogesh Gianchandani has provided me with opportunities that have enabled me to not only increase the depth of my knowledge across a range of fields, but also ingrained in me the skill-set and scientific attitude necessary for research. I am grateful for his guidance.

Over the course of my studies at the University of Michigan, I had the pleasure of having great friends and colleagues. I would like extend my gratitude to the members of the Gianchandani

research group – Yutao, Jun, Xin, Erwin, Yushu, Anup, Ravish, Shiyang, and others. I have had the pleasure of forming great friendships with Tae Hyun, Tal, Stacey, Yi, and hope to keep it alive for years to come. I leave with fond memories of the time that I have spent with them. I would also like to express my sincere thanks to my friends – Mohit, Ashwin, Sahitya, Manoj, Gokul, Ishwarya, Gowthami, among many others – for their support and encouragement.

The support of my family has been the driving force behind my quest for knowledge. My mother, Dr. P. L. A. Satyavathi has been the continuous source of inspiration throughout the years. My father, Mr. P. S. Raju, has imparted in me his zeal and thirst for knowledge, and has been the guiding light throughout my education. I am grateful to my brother Kartik for his support and encouragement.

I am thankful for the unconditional love of my wife Shreevidya, through all the trying times and the happy times. I am looking forward to her company in this journey of life.

## TABLE OF CONTENTS

## LIST OF FIGURES

## LIST OF TABLES

## LIST OF APPENDICES

## ABSTRACT

Magnetoelastic materials exhibit coupling between material strain and magnetization; this coupling provides the basis for a number of wireless transducers. This thesis extends past work on microfabricated magnetoelastic sensors in three ways.

First, a new class of strain sensors based on the ΔE effect are presented. Two sensor types are described – single and differential. The single sensor has an active area of 7×2 $mm^2$ and operates at a resonant frequency of 230.8 kHz with a sensitivity of $13\times10^3$ ppm/mstrain and a dynamic range of 0.05-1.05 mstrain. The differential sensor includes a strain-independent 2×0.5 $mm^2$ reference resonator in addition to a 2.5×0.5 $mm^2$ sensing element. The sensor resonance is at 266.4 kHz and reference resonance is at 492.75 kHz. The differential sensor has a dynamic range of 0-1.85 mstrain, a sensitivity of $12.5\times10^3$ ppm/mstrain, and is temperature compensated in the 23-60°C range.

Second, fluidic actuation by resonant magnetoelastic devices is presented. This transduction is performed in the context of an implantable device, specifically the Ahmed glaucoma drainage device (AGDD). Aspherical 3D wireless magnetoelastic actuators with small form factors and low surface profiles are integrated with the AGDD; the fluid flow generated by the actuators is intended to limit cellular adhesion to the implant surface that ultimately leads to implant encapsulation and failure. The actuators measure 10.3×5.6 $mm^2$ with resonant frequencies varying from 520 Hz to 4.7 kHz for the different actuator designs. Flow velocities up to 266 μm/s are recorded at a wireless activation range of 25-30 mm, with peak actuator vibration amplitudes of 1.5 μm.

Finally, detection techniques for improving the measurement performance of wireless magnetoelastic systems are presented. The techniques focus on decoupling of the excitation magnetic signal from the sensor response to improve measurement sensitivity and noise immunity. Three domains – temporal, frequency, and spatial – are investigated for signal feedthrough. Quantitative results are presented for temporal and frequency domain decoupling. Temporal decoupling is used to measure strain sensors with resonant frequencies in the 125 kHz range, whereas frequency domain decoupling is implemented to measure 44 kHz magnetoelastic resonators.

# CHAPTER 1

# INTRODUCTION

The accelerating pace of advances in the field of sensors and actuators has made possible their expanding roles in implants for multifarious applications. Aided by developments in a wide range of fields including, but not limited to, microfabrication technologies and material sciences, implantable systems are likely to play an increasingly important role in the betterment of human health.

The first successful implantable transducers were relatively simple cardiac muscle stimulators, i.e. pacemakers, developed in the early 1950s [Gre91]. The development of microsensors in the 1970s and microactuators in the 1980s paved the way for new generations of implants for an ever increasing catalog of applications. Leveraging the rapidly maturing silicon IC fabrication industry, micro-electromechanical systems (MEMS) opened up the possibility of scaling down already established technologies for sensing and actuation, which well and truly heralded a new age of implantable system design.

## 1.1 Background

At a systems level, an implantable device has, in general, three components – a transduction mechanism, a communication scheme, and an energy source. An integrated microsystem with micromachined sensors and solid-state circuits for communication and power management presents an attractive architecture for implantable systems. Based on how energy is sourced, implantable systems can be classified as powered or passive systems. A powered system requires

built-in power source (usually a battery) or a capacitor whereas a passive system does not. For chronic implants, a built-in power source must allow wireless charging or be amenable to a surgical replacement of its battery. Percutaneous charging during a drug reservoir refill may also be viable [Eva09]. Wireless power transmission is possible using inductive coupling, although there have been efforts to use microwave radiation as well [Ko77, Pay09]. Data transfer can also be achieved using inductive coupling or radio telemetry [Gho07, Wes09]. Advances in battery technology have not kept pace with the exponential growth in semiconductor and microfabrication technology. Consequently, batteries occupy the bulk of the volume in any powered wireless microsystem.

The inductive link between the implant and external world provides an avenue for innovative and simplistic solutions, especially for design of implantable sensing systems. An example is the intraocular pressure sensor, reported as far back as the 1960s, that measures pressure as a change in the resonant frequency of an inductor-capacitor (LC) tank [Col67]. The resonant frequency was detected through inductive coupling using an external coil. Similar approaches have also been used more recently for detection of, among other parameters, strain [Kro12] and abdominal aortic aneurism pressure [All05], with MEMS technologies enabling further miniaturization and refinement. In such devices, the parameter of interest causes a change in the capacitance of the resonant tank, thereby changing its resonant frequency. The relative simplicity and small count of components necessary for such designs ensures robustness and small form factors, making them good candidates for implantable sensing systems.

Magnetoelastic materials provide another pathway for systems based on inductive links. These materials exhibit a coupling between magnetic and mechanical domains and are, in a way, magnetic analogues of piezoelectric materials [IEE91]. Such materials can be externally activated through a magnetic field, without the need of an implanted coil as required in passive resonant

sensing devices using LC tanks. The goal of this work is the development of implantable devices that build on the significant benefits of the magnetoelastic transduction approach. A comparison of different transduction approaches for biomedical applications based on powering considerations is provided in Table 1.1.

TABLE 1.1. COMPARISON OF DIFFERENT TRANSDUCTION APPROACHES FOR BIOMEDICAL APPLICATIONS BASED ON POWERING CONSIDERATIONS – ACTIVE OR PASSIVE

| **Transduction method, illustrative example** | **Application** | **Active** | **Passive** |
|---|---|---|---|
| **Capacitive** | | | |
| Graefe, 2009 [Gra09] | Blood pressure monitor | ✓ | |
| Allen, 2005 [All05] | Abdominal aortic aneurism pressure sensor | | ✓ |
| Lei, 2006 [Lei06] | Glucose sensor | | ✓ |
| Chen, 2011 [Che11] | Intraocular pressure sensor | ✓ | |
| **Piezoelectric** | | | |
| Lesho, 1989 [Les89] | Core body temperature sensor | ✓ | |
| Wang, 2011 [Wan11] | Middle-ear hearing device | ✓ | |
| **Piezoresistive** | | | |
| Westerhoff, 2009 [Wes09] | Shoulder joint implant force sensor | ✓ | |
| D'Lima, 2005 [D'Li05] | Knee joint implant force sensor | ✓ | |
| **Thermal** | | | |
| Johnston, 1988 [Joh88] | Drug pump | | ✓ |
| Medtronic, Inc. [Med00] | Drug pump | ✓ | |
| Rahimi, 2010 [Rah10] | Drug release microvalve | | ✓ |
| **Optical** | | | |
| Colvin, 2013 [Col13] | Glucose sensor | ✓ | |
| Theodor, 2013 [The13] | Blood pressure sensor | ✓ | |
| **Electrochemical** | | | |
| Li, 2009 [Li09] | Drug release microvalve | | ✓ |
| Armour, 1990 [Arm90] | Glucose sensor | ✓ | |
| **Magnetoelastic** | | | |
| Green, 2009 [Gre09a] | Biliary stent occlusion sensor | | ✓ |
| Viswanath, 2013 [Vis13] | Artery stent occlusion sensor | | ✓ |
| Mouzakis, 2009 [Mou09], Oess, 2009 [Oes09] | Orthopedic implant stress sensor | | ✓ |

## 1.2 Magnetoelastic materials as transducers

### 1.2.1 Introduction

A magnetic field applied to a magnetoelastic material produces strain; this effect is termed Joule magnetostriction. An inverse effect, termed the Villari effect, results in the magnetization of material when strain is applied. Both effects are associated with the rotation of magnetic moments within domains that leads to the magnetization of the material. Joule magnetostriction is caused by moment rotation under an applied magnetic field, whereas the Villari effect is caused by the moment rotation under strain. The simplest visualization for these magnetoelastic effects is provided by considering an atom with an anisotropically-shaped charge cloud in the form of an ellipsoid. In materials with strong spin-orbital coupling, rotation of the electron spins with applied field will cause rotation of charge clouds, effectively causing a change in material dimensions (Fig. 1.1).

### 1.2.2 Mathematical models for magnetoelastic effects

For cubic crystals the saturation magnetostriction (expressed as a fractional change in length $\Delta l/l$ ) is given by the equation [Cla80]:

$$\frac{\Delta l}{l} = \frac{3}{2}\lambda_{100}\left(\alpha_x^2\beta_x^2 + \alpha_y^2\beta_y^2 + \alpha_z^2\beta_z^2 - \frac{1}{3}\right) + 3\lambda_{111}(\alpha_x\alpha_y\beta_x\beta_y + \alpha_y\alpha_z\beta_y\beta_z + \alpha_z\alpha_x\beta_z\beta_x) \quad (1.1)$$

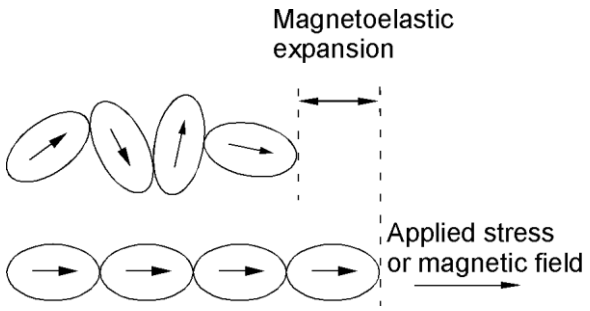


**Fig. 1.1:** Illustration of rotation of the electron charge cloud in an atom with strong spin-orbital coupling. Arrows represent the direction of atomic magnetic moments.

Here, $\alpha_i$ denote the direction cosines of applied magnetization; $\beta_i$ denote the direction cosines along which the strain is measured; $\lambda_{100}$ and $\lambda_{111}$ are the saturation magnetostrictions along [100] and [111] directions. For isotropic polycrystalline and amorphous materials, the magnetostriction is given by [Cul09a]:

$$\frac{\Delta l}{l} = \frac{3}{2}\lambda_s \left(cos^2\theta - \frac{1}{3}\right) \tag{1.2}$$

where $\theta$ is the angle between the saturation magnetization and the measurement direction, and $\lambda_s$ is the isotropic saturation magnetostriction. Equations 1.1 and 1.2 provide the change in dimension when the material is subject to magnetic fields that result in complete rotation of magnetic moments in the direction of applied field. The rotation of magnetic moments and the resulting change in dimension, are also functions of the magnitude of the applied field. For materials showing a two-fold in-plane magnetic anisotropy (i.e. uniaxial anisotropy) (Fig. 1.2), which as-quenched amorphous metals are known to possess [Fuj83], magnetostriction can be related to applied magnetic field, $H$, as:

$$\frac{\Delta l}{l} = \frac{3}{2}\lambda_s \left(\frac{H^2}{H_A^2} - \frac{1}{3}\right) \tag{1.3}$$

where $H_A$ is the anisotropy field [Liv82]. The anisotropy field is a measure of magnetic anisotropy in a material. Under the influence of applied magnetic field, the anisotropy field acts like a magnetic field that opposes the rotation of magnetic domains.

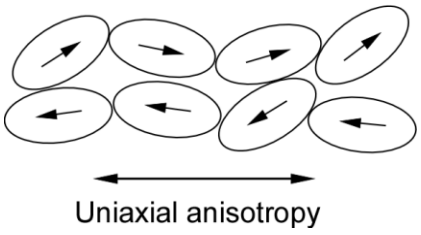


**Fig. 1.2:** Magnetic domains in a material with uniaxial anisotropy. The domains in such materials tend to align along one axis.

When an alternating magnetic field is applied to a magnetoelastic material, the mechanical vibration, associated with Joule magnetostriction, results in a material magnetization, associated with the Villari effect. Although these magnetoelastic effects are non-linear, for small-amplitude oscillations about fixed bias values of magnetic field and stress, the response can be linearized. For a one-dimensional system, considering stress and field intensity as the independent variables, the relationship is given by the following pair of coupled equations [Kat59]:

$$\varepsilon = \left.\frac{\partial \varepsilon}{\partial \sigma}\right|_H \sigma + \left.\frac{\partial \varepsilon}{\partial H}\right|_\sigma H \tag{1.4}$$

$$B = \left.\frac{\partial B}{\partial \sigma}\right|_H \sigma + \left.\frac{\partial B}{\partial H}\right|_\sigma H \tag{1.5}$$

where $\sigma$ is stress, $\varepsilon$ is strain, $B$ is magnetic flux density and $H$ is magnetic field. The partial derivatives are as follows: $\left.\frac{\partial \varepsilon}{\partial \sigma}\right|_H$ is the compliance at constant $H$ field, $s^H$; $\left.\frac{\partial B}{\partial H}\right|_\sigma$ is the permeability at constant stress, $\mu^\sigma$; and $\left.\frac{\partial \varepsilon}{\partial H}\right|_\sigma$ and $\left.\frac{\partial B}{\partial \sigma}\right|_H$ are both represented by $d$, the magnetostrictive coefficient. Equations 1.4 and 1.5 are the linear small-signal approximations of the non-linear magnetoelastic behavior described by Equations 1.1-1.3, while also considering the coupling between the magnetic and elastic physics.

The amplitude of vibration is determined by the magnetostrictive coefficient, $d$, which is dependent on the DC bias conditions. The slope of the magnetostriction curve as a function of an applied DC magnetic field is given by $d$. For amorphous materials, it is given by [Liv82]:

$$d = \frac{3\lambda_s H_{DC} M_S^2}{(2K_u - 3\lambda_s \sigma)^2} \tag{1.6}$$

where $M_s$ is the saturation magnetization, $H_{DC}$ is the applied DC bias field, $\sigma$ is the applied stress in the direction of the field. The constant $K_u$, which is the uniaxial magnetic anisotropy constant, defines the energy stored in the material when the magnetic domains are rotated away from the

easy axis. The value of $K_u$ is material dependent and can be experimentally determined by measuring the torque exerted by a sample as a result of the rotation of its magnetic moments.

The energy transfer efficiency between the elastic and magnetic processes in a magnetoelastic material is defined by the magnetomechanical coupling coefficient, *k*. The fraction of magnetic energy that is converted to elastic energy per cycle, or vice-versa, is equal to $k^2$. It is given by [Cla80]:

$$k^2 = \frac{d^2}{s^H \mu^\sigma} \tag{1.7}$$

The coupling between the stress and magnetic field in a magnetoelastic material also results in the ΔE effect. The ΔE effect is the change in the stiffness of a magnetoelastic material under applied stress or magnetic field. This effect can be quantified as the fractional difference between the Young's modulus at constant magnetization, $E_B$, and the Young's modulus at constant field, $E_H$. For amorphous materials, the fractional difference is given by [Liv82]:

$$\frac{E_B - E_H}{E_H} = \frac{\Delta E}{E_H} = \frac{9\lambda_s^2 E_B H_{DC}^2 M_S^2}{(2K_u - 3\lambda_s \sigma)^2} \tag{1.8}$$

### 1.2.3 Materials

A range of magnetoelastic materials – both crystalline and amorphous – have been used in transducer applications [Eng00, Gri11]. Crystalline rare-earth magnetoelastic alloys such as Terfenol-D ($Tb_{1-x}Dy_xFe_2$, $0.70<x<0.73$) (which is commercially available from Etrema Products, Inc., Ames, IA) allow maximum magnetostrictions of hundreds of microstrains to a few millistrains, and are widely used for actuator applications. These materials can be fabricated using traditional single crystal growth methods such as the Czochralski process. Amorphous alloys can be fabricated by sputtering [Hon93], evaporation [Riz07], or rapid quenching from a molten state [Kle60], and are commercially available as thin foils. Examples of commercial thin foils include

Metglas 2826MB ($Fe_{40}Ni_{38}Mo_4B_{18}$) and 2705M ($Co_{69}Fe_4Ni_1Mo_2B_{12}Si_{12}$) (available from Metglas, Inc, Conway, SC).

Although crystalline magnetoelastic materials have been engineered to allow large magnetostrictions, they are usually brittle and have low tensile strength [Etr00, Dow05]. In addition, these materials can require a high bias field when used in resonant sensors. In contrast, amorphous metals impart significant advantages over crystalline materials. For instance, single-crystal Terfenol-D can require bias fields of the order of hundreds of oersteds whereas Metglas 2826MB, an amorphous alloy, requires a bias field of only a few oersteds [Gol99, Gre10]. The lower bias field allows the use of smaller magnets and reduces the overall device size.

Many properties of amorphous alloys are amenable to customization, providing added flexibility for device design. Amorphous materials can be tailored to have a high magnetomechanical coupling coefficient, *k*, through the process of annealing in a magnetic field – a feature which can be advantageous in transducer applications [Ras83, Bro79, And82]. Additionally, the ΔE effect in amorphous magnetoelastic materials can be modified by annealing under varying temperature and magnetic field conditions [Ber76].

The availability of amorphous magnetoelastic metals in the form of thin sheets that can be machined to small form factors has also contributed to their development for a range of applications. They can be patterned using micro-electrodischarge machining (μEDM) or photo-chemical machining (PCM). The μEDM option offers a micro-scale resolution but a low throughput and is ideal for prototype fabrication [Mas90, Tak02]. In contrast, PCM is a batch-mode process that allows high throughput but a lower resolution [Fri89]. Commercially available PCM facilities provide resolution of a few microns which is adequate considering the millimeter-scale form factors used in most applications.

### 1.2.4 Magnetoelastic Transducers

Transducers based on magnetoelastic effects can be broadly classified as resonant and non-resonant. A resonant transducer is operated at its mechanical resonance which is induced by the application of an excitation magnetic field at appropriate frequency. A non-resonant transducer, as the name suggests, does not rely on induced mechanical resonance. The device can be operated at DC or at frequencies away from its mechanical resonant frequency.

Resonant transducers are commonly employed for sensor systems. An impinging magnetic field at the appropriate frequency excites the sensor to resonance. The response of the sensor can be detected in multiple ways (magnetic, optical, or acoustic) and forms the basis of many implementations of this technology (Fig. 1.3). The resonant frequency is measured by magnetically exciting the sensor over a range of frequencies and simultaneously measuring the response, or by measuring the ring-down response to an impulse magnetic field excitation. For the first case, the received signal exhibits a spike in amplitude when the excitation frequency

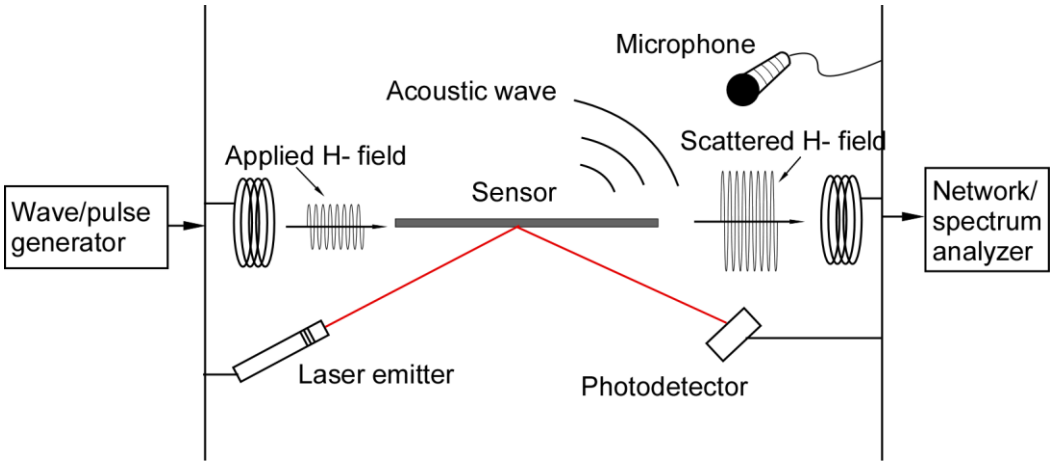


**Fig. 1.3:** Detection of resonance of a magnetoelastic sensor [Gri11]. The sensor is excited by an applied magnetic field. Resonance detection is possible by measuring scattered magnetic field, or the acoustic response, or a reflected laser beam at a photodetector.

matches the sensor resonant frequency. For the second case, the frequency spectrum of the ring-down exhibits a peak at the sensor resonant frequency.

A common sensing technique involves the detection of a change in resonant frequencies of magnetoelastic sensor caused by changes in mass loading, viscosity or magnetic field conditions [Gre09a, Vis13, Bar00, Joh08, Kou00]. For instance, the resonant frequency $f_0$ of a free-standing uniform strip of magnetoelastic material exhibiting a longitudinal resonance mode is given by:

$$f_0 = \frac{1}{2L}\sqrt{\frac{E_B(1-k^2)}{\rho}} \tag{1.9}$$

where $L$ is the length of the strip, $E_B$ is the Young's modulus at constant B, $k$ is the magnetomechanical coupling coefficient and $\rho$ is the density [O'De82]. For a strip of uniform thickness, width and density, the resonant frequency is independent of the sensor width. The change in resonant frequency of a sensor with mass $m_0$, when subject to mass loading of $\Delta m$ is given by [Gri11]:

$$\Delta f = -f_0 \frac{\Delta m}{2m_0} \tag{1.10}$$

Non-resonant sensors detect the change in magnetic permeability that modifies the magnetic coupling between interrogation coils and the sensor. As a result of the Villari effect, applied stress induces a change in the magnetization state of a magnetoelastic material, effectively modifying its permeability. The permeability change can be measured as a change in inductance of a coil or the mutual inductance between two coils wrapped around the magnetoelastic material [Kar00, Tra08, Fle89, Kla09, Sil12].

Tagging applications, used ubiquitously in electronic article surveillance, rely on positive identification of a magnetoelastic resonator. This function is also dependent on the detection of the resonant frequency of the magnetoelastic tag [And85, Kim96] or the measurement of harmonic response when excited at a predetermined frequency [Her03].

Rare-earth crystalline giant magnetostrictive materials are an alternative to piezoelectric materials for some macro-scale applications and are commercially available [Cla97]. Although not mainstream, sputtered thin-films of magnetoelastic materials have been investigated as an alternative to the more traditional electrostatic and piezoelectric materials for actuation [Qua95]. In [Hon94], Honda *et al* described the use of sputtered TbFe and SmFe for actuation of cantilevers. A similar method was used by Lee *et al* for actuation of micro-mirrors using the magnetostriction of sputtered TbDyFe layers under applied magnetic fields [Lee07]. Tang *et al* developed wirelessly actuated rotary micromotors that use resonant thin foil magnetoelastic alloys [Tan13]. Liu *et al* used resonant actuation of thin foils to create "swimming microrobots" for potential applications in pipeline inspection and microsurgery [Liu10].

### 1.2.5 Comparison with piezoelectric transduction

Piezoelectric materials exhibit coupling between electric fields and material stresses and strains and are, in many ways, analogous to magnetoelastic materials. Because of this, a comparison between the performances of magnetoelastic materials and piezoelectric materials is appropriate. The most important parameters of comparison for vibratory transducers fabricated from these materials are the coupling factors, quality factors, and small signal magnetostrictivities or the piezoelectric strain constants. Table 1.2 shows such a comparison between a sample of magnetoelastic and piezoelectric materials. The comparable properties of the piezoelectric and magnetoelastic materials, in addition to the wireless transduction capability of magnetoelastic materials, lend credence to the benefits of the use of magnetoelastic transduction for applications where piezoelectric methods are traditionally employed.

TABLE 1.2. COMPARISON OF SOME PROPERTIES OF REPRESENTATIVE PIEZOELECTRIC AND MAGNETOELASTIC MATERIALS.

| | **Coupling factor, $k_{33}$** | **Piezoelectric strain constant/ small signal-magnetostrictivity** | **Quality factor** |
|---|---|---|---|
| **Piezoelectric materials [Uch03]** | | | |
| Quartz | 0.09 | 2.3 pC/N | >10000 |
| $BaTiO_3$ | 0.38 | 190 pC/N | - |
| PZT4 | 0.51 | 289 pC/N | 500 |
| **Magnetoelastic Materials** | | | |
| Terfenol-D [She07, Cla80] | 0.72 | 15 nm/A | 150 |
| Galfenol [She07] | 0.61 | 46 nm/A | - |
| Metglas 2605SC [She07, Bhu14] | 0.92-0.97 | 910 nm/A | - |
| Metglas 2826MB [Gut13, Bhu14, Tor78] | 0.98 | 12 nm/A | >100 |

## 1.3 Motivation and Previous Work

Section 1.1 highlighted the main requirements of an implantable system – a transduction mechanism, a communication scheme and a power source. Magnetoelastic materials present a unified solution, meeting all the three requirements. This has allowed the development of a range of transducers that measure a variety of physical phenomena, showcasing the wide applicability of the magnetoelastic transduction approach. Because magnetoelastic materials exhibit bidirectional coupling between mechanical motion and magnetic field, magnetoelastic transducers can respond to wireless interrogation by a magnetic field without the need for an antenna to be integrated with the transducer. Moreover, the transduction is passive and requires no additional built-in power source. As such, the transducers are completely self-contained. These features can be highly advantageous in implantable systems allowing considerable miniaturization, simplicity, and

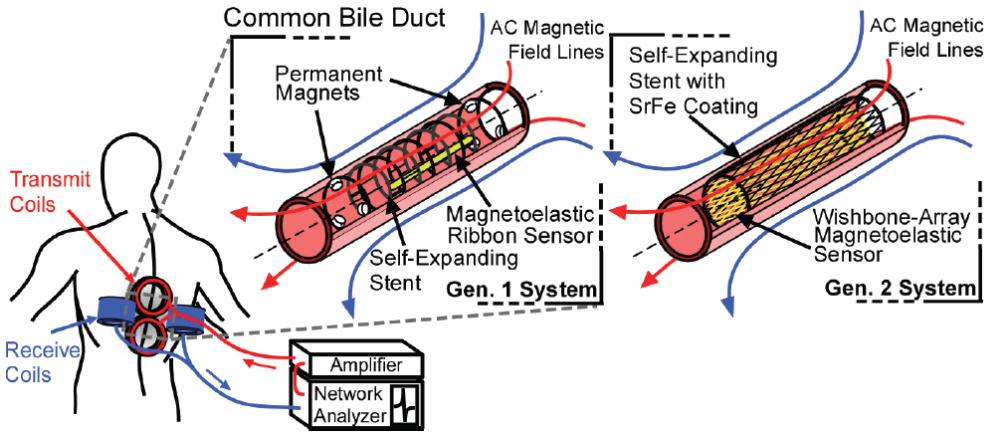


**Fig. 1.4:** Measurement of biliary stent sludge accumulation by a magnetoelastic resonator [Gre09b]. The resonant frequency is observed as a peak in the frequency spectrum of the receive coils.

reliability. With further research, magnetoelastic transduction can facilitate new types of implantable transducers.

Figure 1.4 shows an example of two generations of magnetoelastic resonant sensors as used for detection of sludge accumulation in biliary stents [Gre09b]. Sludge deposited on the sensor reduces the resonant frequency (as given approximately by equation 1.5) which is wirelessly detected by the external interrogation coils. The devices are completely passive, and are integrated with the biliary stent. These sensing devices exemplify the features of magnetoelastic transduction that can be leveraged for implantable biomedical applications.

The built-in coupling between mechanical deformations and magnetic fields in a magnetoelastic material provides an avenue for development of new classes of wireless mechanical transduction devices for biomedical applications. On the sensing side, wireless strain sensing devices based on magnetoelastic coupling can be developed for passive measurement of mechanical strains in implantable devices – an application that will find use in monitoring of orthopedic implants. On the actuation side, magnetically actuated mechanical actuators can modulate cell adhesion on implant surfaces leading to applications in management of implant-

tissue interfaces. Development of transducers for such biomedical applications is the goal of this research.

### 1.3.1 Orthopedic implant load monitoring

The utilization of wireless strain sensors for real-time, *in vivo* measurement of loads on orthopedic implants can enable personalized diagnosis, treatment, and rehabilitation [Led12]. Such sensors can enable the continuous monitoring of loads to which the implant is subject during use. Treatment options and rehabilitation exercises can be prescribed or modified to improve the patient recovery [Bur00]. The sensors can also be applicable for the monitoring of long-term implant health. For biomechanical implants, failure due to overloading is a major concern [Dob82, Hug72]. Real-time measurements can enable detection of conditions that lead to implant failure, and allow remedial steps to be initiated. Additionally, strain measurements taken during *in vivo* experimental studies are a valuable tool for optimization of implant designs [Kom05]. Experimental devices instrumented with strain sensing apparatus can be used to monitor *in vivo* loads in human and animal models, enabling design improvement.

In general, the use of strain gages with wireless telemetry is a common approach for load measurement in orthopedic implants [Ber88]. Westerhoff *et al* used strain gages with telemetry circuitry to implement a system that measured contact forces and moments in an artificial shoulder joint [Wes09]. The device used inductive coupling for wireless transmission of power as well as for communication with external hardware. A similar system was devised for monitoring of femoral fracture treatment orthopedic plates [Bur00]. Figure 1.5 shows two examples of orthopedic implants with instrumented strain gages and wireless telemetry.

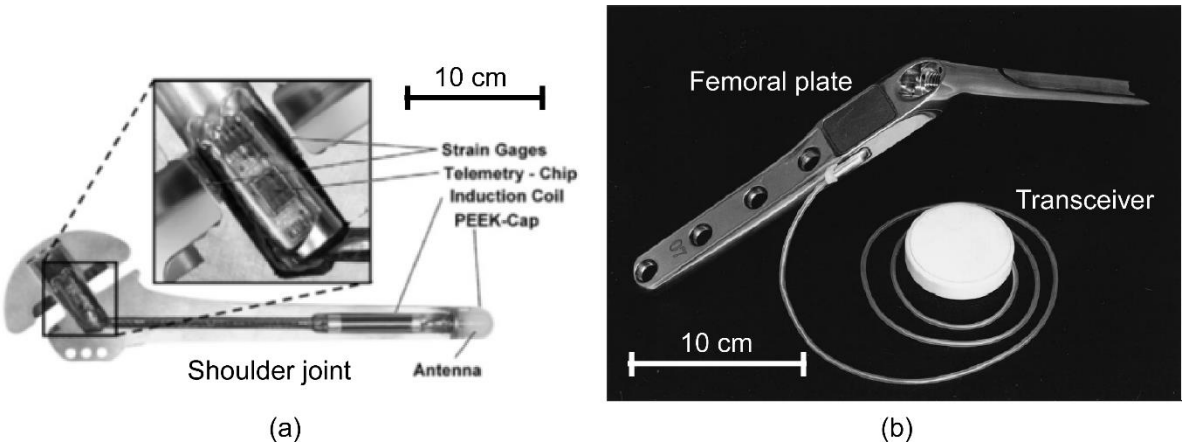


**Fig. 1.5:** Application of strain gages in orthopedic implants. (a) Instrumented shoulder implant with strain gages and passive wireless telemetry [Wes09]. (b) Femoral plate with strain gages and wireless transceiver module [Bur00].

Passive approaches have been reported previously for determination of strain by measurement of resonant frequency of LC tanks [Jia06, Loh07, Kro12]. These approaches can be used for orthopedic implants. For example, the sensor can be designed so that, strain causes a change in the capacitance of the LC tank, which can be remotely determined using a read-out coil. Figure 1.6 shows a few examples of this approach. Other techniques for passive strain sensing have utilized RF electromagnetic backscattering, and surface acoustic waves [Jan13, Chu05, Des10, Kon07].

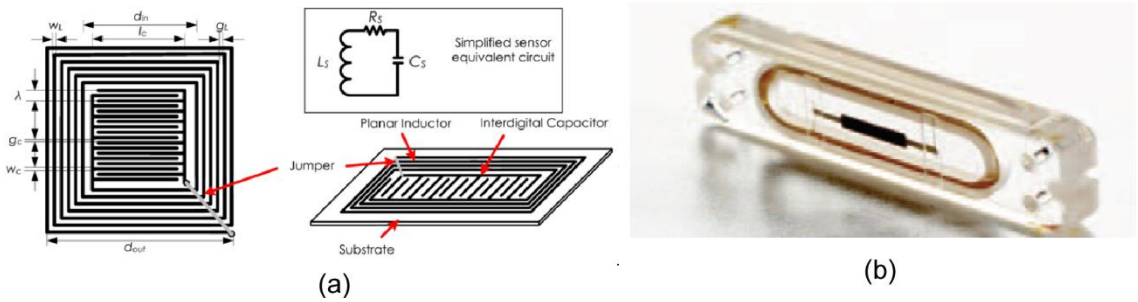


**Fig. 1.6:** LC tank based passive resonant sensors. (a) Sensor using interdigitated electrodes for capacitor [Jia06]. (b) First implantable strain sensor approved by the Food and Drug administration (CardioMEMS, Inc.) [Kro12, Led12].

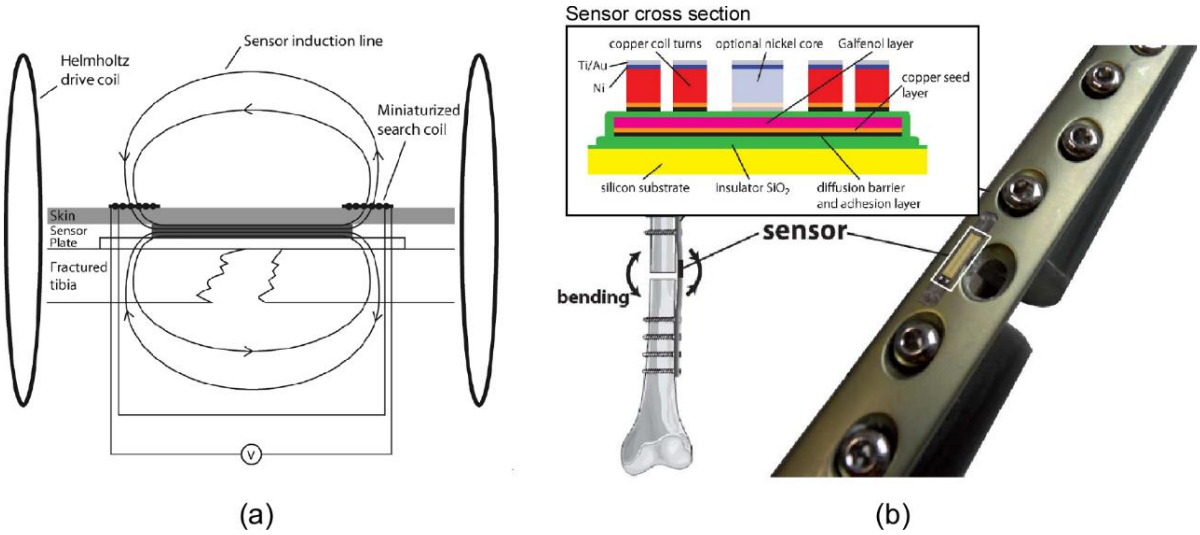


**Fig. 1.7:** Magnetoelastic strain sensor examples as used for orthopedic implants. (a) Strain detected as a change in coupling between drive and search coil [Oes09]. (b) Strain detected as a change in resonant frequency of an LC tank [Sau12].

Magnetoelastic materials have been previously reported for strain measurement in orthopedic implants [Oes09, Odu6, Mou09]. Applied strain changes the permeability of the sensor through the Villari effect, modifying the coupling between the transmit and the receive coils (Fig. 1.7(a)). The signal output at the receive coil is dependent on the coil position. Hence, care must be taken to appropriately account for this potential variability. Permeability change can also be detected as a change in the self-resonant frequency of an LC coil, with the magnetoelastic material coupling with the inductor [Sau12] (Figure 1.7(b)).

### 1.3.2 Regulation of fibrosis in a glaucoma drainage device

Glaucoma is a term that encompasses a set of disorders that cause progressive loss of vision as a result of damage to the optic nerve. It is usually characterized by a high intra-ocular pressure (IOP). It was estimated that there were 60.5 million people with glaucoma worldwide in 2010, with the number expected to rise to 79.6 million by 2020 [Qui06]. Glaucoma is now the second leading cause of blindness globally [Res04].

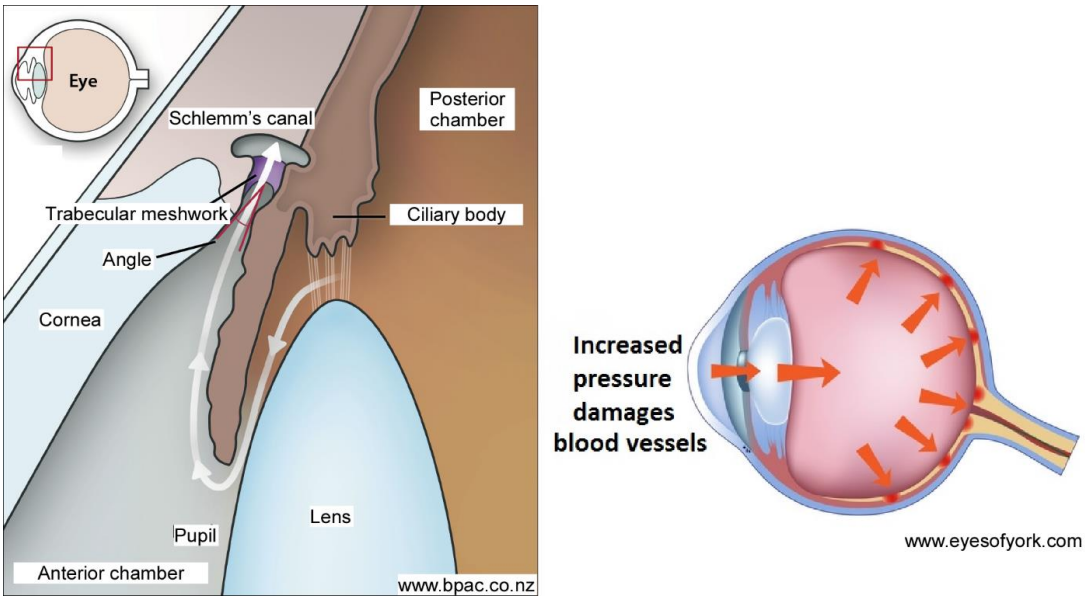


**Fig. 1.8:** (a) Aqueous humor (AH) outflow from the anterior chamber in a normal human eye. Red arrow shows the path of AH outflow. (b) Increased resistance to AH outflow increases the pressure inside the eye, which can lead to damage to the optic nerve.

Aqueous humor (AH) is generated by the ciliary body in the eye. In a healthy eye, AH flows through the posterior chamber into the anterior chamber, and then through the trabecular meshwork into Schlemm's canal. The canal collects the AH and transfers it to the blood stream through the episcleral veins. Figure 1.8(a) shows a close-up of the eyeball with these features highlighted. An increase in outflow resistance of AH leads to elevated pressure which can, over time, damage the optic nerve (Fig. 1.8(b)).

High IOP is typically managed by pharmaceutical treatments or surgical interventions performed by laser or incision [Mig86]. The pharmaceutical treatments are generally administered as eye drops [Tor10], whereas the surgical methods include laser trabeculoplasty and, to a lesser extent, glaucoma filtration surgeries [Tho82, Cai68]. Glaucoma drainage devices (GDDs) are used for cases of intractable glaucoma though findings from recent clinical trials have supported the use of these devices much earlier in the disease course [Ged07]. As a result, utilization of GDDs has increased considerably in the past decade.

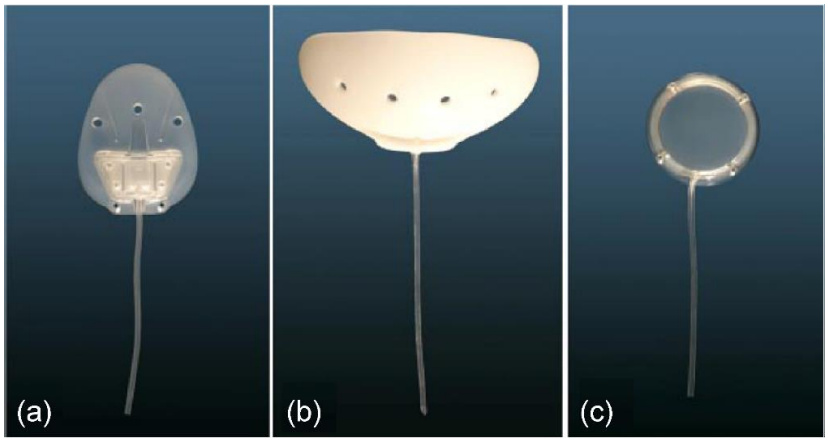


**Fig. 1.9:** Three commonly used GDDs. (a) Ahmed glaucoma valve (FP-7), (b) Baerveldt implant (BG101-350), and (c) Molteno implant (S1) [Cho10].

The history of surgical intervention to aid the outflow of fluid from the anterior chamber can be traced back to 1907, when a horse hair was used to drain inflammatory cells [Lim98]. The first attempt to drain AH was reported in 1912, when a silk thread was used to drain into subconjunctival space [Zor10]. The first use of a tube and plate device was reported in 1969; this introduced the principle that is followed by most glaucoma drainage devices in clinical use currently (Fig. 1.9) [Mol69].

Most modern GDDs bypass the trabecular meshwork with a tube that is inserted into the anterior chamber of the eye, and a plate (connected to the tube) that is placed in the subconjunctival

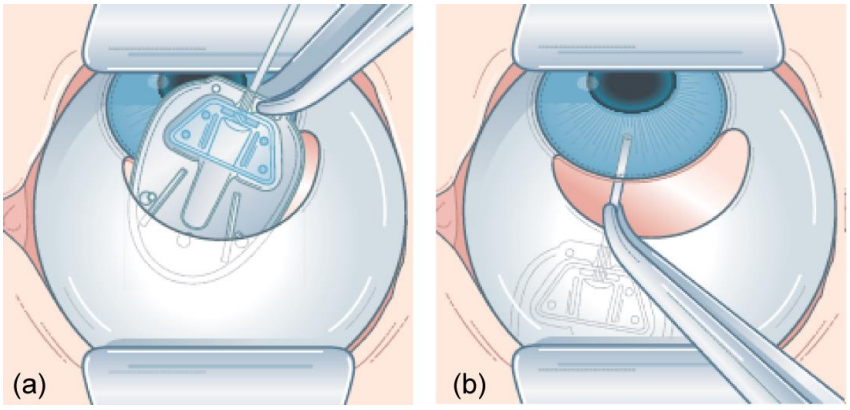


**Fig. 1.10:** Surgical implantation of the Ahmed glaucoma valve. (a) Insertion of the valve in the Tenon's capsule. (b) Insertion of the tube into the anterior chamber [Boy09].

space over the sclera (Fig. 1.10). The tube drains AH into the space created by the plate, thereby relieving the elevated pressure inside the eye. However, a regulatory mechanism is necessary to control the flow of AH. In valveless GDDs, the resistance to flow is provided by fibrous tissue that forms over the plate as a part of the wound healing reaction of the body. A valved device, as the name suggests, has a built in mechanism of flow control that only allows AH outflow when the IOP exceeds a specific pressure. These devices do not rely on the fibrous reaction to create the necessary flow regulation. The Baerveldt and Molteno implants are non-valved devices, whereas the Ahmed valve has an AH flow regulation mechanism.

The response to an implanted glaucoma drainage device is the formation of a fibrous bleb around it with highly organized collagen fibers [Loe88, Mol03, Eib05, Wil07, Lee14, Phi90, Cam88] (Fig. 1.11). The tissue response is complicated by the fact that AH itself influences the fibrosis. Glaucomatomous AH results in an inflammatory response resulting in fibrovascular tissue proliferation (granular tissue formation and foreign body reaction) [Eps59]. Once the IOP has been normalized, the AH initiates a fibrodegenerative response that is characterized by reducing cell count and collagen fragmentation in the inner layers [Her81]. Hence, the fibrous

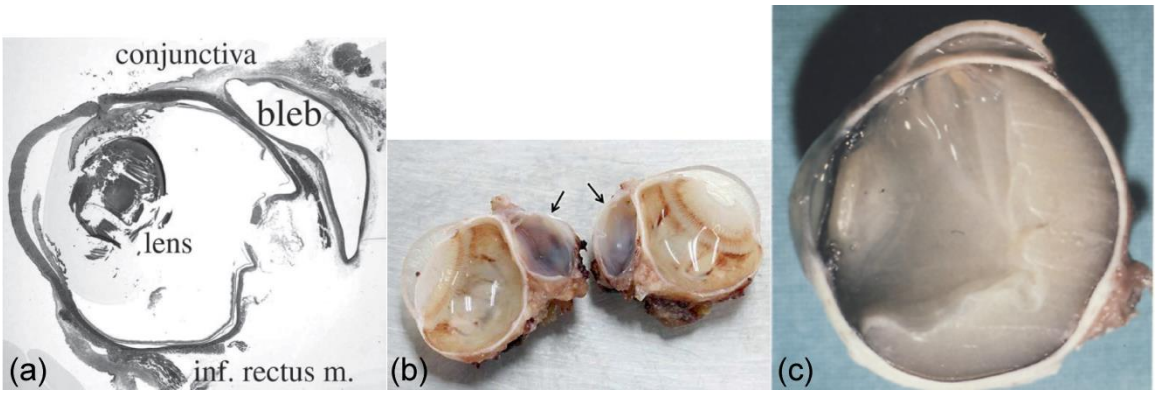


**Fig. 1.11:** Fibrous blebs formed around the implants. (a) Rabbit eye, 6 months post-implantation of a Baerveldt implant [Wil07]. (b) Rabbit eye, 2 months post-implantation of an Ahmed valve [Lee14]. (c) Human eye, 11 months post-implantation of an ADATOMED drainage system [Phi90].

bleb consists of two layers with the avascular inner layer populated with few fibroblasts and myofibroblasts **[**Lee14, Mol03, Phi90]. The outer layer shows presence of blood vessels created by neovascularization. The success of the implant depends on the organization of the collagen in the inner layers. A thin, inner collagen lining would allow the AH to percolate out to the vascular tissues in the outer layers of the bleb, allowing efficient removal of the fluid by the episcleral veins [Cam88, Phi90].

In a well-functioning implant with controlled IOP, the wall of the bleb has a thickness of less than 500 μm [Mol03]. However, in a subset of patients, a thick, dense inner layer of collagen forms around the plate body, reducing the permeability to the AH, and increasing the resistance to its outflow [Hon05, Cho10]. In cases that show encapsulating bleb formation with high IOP, the bleb thickness can be as high as 1.5-2 mm. Such cases are also characterized by thrombosis (i.e., local coagulation) in the vascular tissues, which further reduces the re-absorption capability of the fibrous bleb [Thi11]. The Ahmed valve seems particularly susceptible to encapsulation induced increase in IOP, with up to 80% of the cases exhibiting it; while non-valved devices like the Molteno and the Baerveldt implants show up to 30% incidence of encapsulation [Hon05]. Physical massage, or needling of the bleb, or surgical excision are indicated in these cases.

Chemical and physical surface modification measures such as plasma treatment, deposition of bioactive coatings, and texturing, among other methods, have shown promise in improving tissue integration with implantable biomaterials [Jen12, Zha14, Chu02, Ros03, Bra97]. However, these measures are ineffective at limiting fibrous encapsulation [Jen12, Gra97, Par02]. Surface microstructures have been shown to lower the fibrous response to certain biomaterials [Pic96, Rec95]. Conversely, greater surface roughness has been associated with increased fibrous encapsulation in GDDs [Cho10, Ayy00], calling into question the feasibility of using this approach

for GDDs. Other efforts targeted at reducing encapsulation in GDDs have been focused on the use of anti-fibrotic agents such as mitomycin C, 5-fluorouracil, and triamcinolone acetonide, but these interventions have also met with limited success [Kur05, Tei12, Cos04]. In addition, these measures can lead to complications such as necrosis of the conjunctival tissue or can contribute to an increased risk of complications such as hypotony (i.e., low IOP) or serious infection [Hon05, Ayy98].

The fibrosis response following the implantation of the GDD involves formation of granulation and foreign body reaction tissue at the location of the implant. Implantation of a glaucoma drainage device provides a surface that allows the fibroblasts and vascular endothelial cells to proliferate. Hence, the extent of the fibrovascular tissue response can be correlated to the initial adhesion of these cells to the implant surface [Cho10, Ayy99].

*In vitro* studies have shown that local vibrations and fluid agitation that generate shear stresses can influence the adhesion and proliferation of cells [Tit12, Ito11, Tru90]. Above a specific oscillating stress limit, human fibroblasts fail to adhere to the substrate [Tit12]. Additionally, *in vitro* studies have also shown that vibrations negatively influence the proliferation of certain types of mouse embryonic fibroblasts [Ito11], with vibration amplitudes measuring approximately 100 nm at frequencies of 100 Hz and 1 kHz being tested. Separately, the use of magnetoelastic resonators as planar vibrating substrates has also been evaluated for the control of cell adhesion [Vla11]. A significant reduction in the adhering fibroblast cell count was found for vibration amplitudes of 150 nm, using planar rectangular magnetoelastic resonators operating at 176 kHz.

### 1.3.3 Resonant frequency measurement of magnetoelastic devices

Measurement of the resonant behavior of magnetoelastic structures is an essential component for applications in sensing and tagging [Gri11, Tan14, And85]. Many sensors based on magnetoelastic materials use a change in resonant frequencies to determine the measurand [Vis13, Hub12, Bar00, Jai01, Joh08, Yos05]. Resonant frequency and quality factor measurements are also used for material characterization; for instance, to determine the stiffness, magnetomechanical coupling coefficient, or damping [And82, O'De82, Tor78]. Hence, accurate measurement of resonances is an important element for technologies based on magnetoelastic materials.

As described in section 1.1, the coupling between the magnetic and elastic domains of magnetoelastic material allows the remote excitation of resonances. The backscattered magnetic field associated with the induced resonant vibration is detected by a receiving coil or antenna. The resonant frequencies can be determined from the received voltage using either frequency domain or time domain methods.

In frequency domain detection, a range of frequencies is swept by the transmit coil, while the receive coil simultaneously detects the response from the device under test (Fig. 1.12(a)). The transmit and the receive circuits are synchronized to operate at identical frequencies at a given instance of time. The voltage detected by the receive coil shows a maximum at the device resonant frequency [Gre09a]. A single coil can also be used for resonant frequency detection – the impedance of the coil exhibits a peak at the device resonant frequency [Bar00].

In typical time domain detection, an incident magnetic pulse excites the resonant device, following which the ring-down oscillations are measured (Fig. 1.12(b)). Excitation and detection can be performed using separate coils or a single coil that is switched between the transmit and the

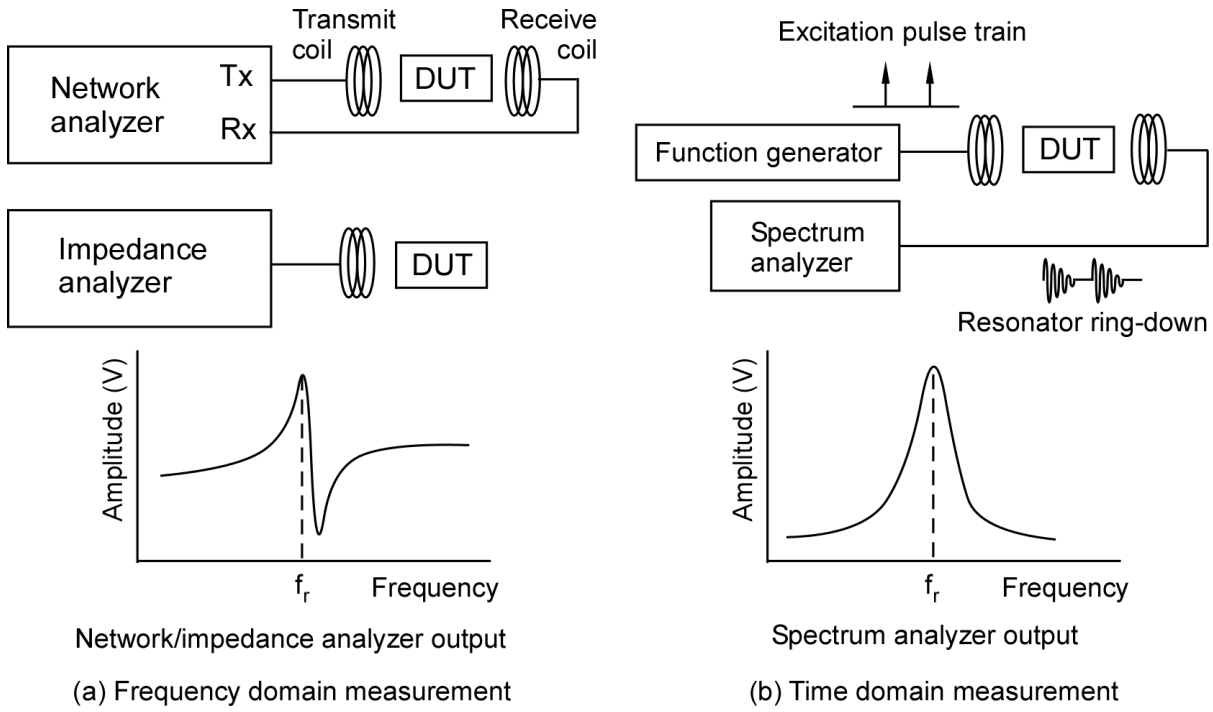


**Fig. 1.12:** Typical methods of measurement of resonant magnetoelastic devices. (a) Frequency domain and (b) time domain.

receive circuits. The ring-down is at the device resonant frequency and can be measured by using Fourier analysis or frequency counting techniques [She10, Zen02, Sau12].

If the time domain approach is performed using impulse excitation, the incident field is distributed over a broadband spectrum. Much of the excitation field is not in the vicinity of the resonant frequency of the device and does not contribute to the output signal. Conversely, with the approach based on a frequency sweep, the excitation magnetic field is at the device resonant frequency, leading to a stronger resonant response from device. As a result, an impulse response-based time domain approach has a weaker resonant response than a frequency sweep-based for identical excitation fields.

An advantage of the time domain approach is the isolation of the transmitted field from the receive circuit, which reduces the feedthrough. The receive circuit can be synchronized to measure the resonator response, while being deactivated during the transmit phase. Decoupling the

magnetoelastic resonant response from the excitation field is useful in a multitude of ways. It enables the use of stronger excitation magnetic fields without the risk of damaging the receive circuit by overloading it. The expected improvement in system performance is twofold: (i) the dimensional range of the excitation can be increased as the transmit coils can now be used to generate a stronger field over extended distances; and (ii) the resonators can now be driven to larger vibration amplitudes, enabling the generation of stronger signals at the receive coil. In addition, the decoupling isolates the comparatively weak resonant response of the resonators from the much stronger excitation magnetic field. Weak resonant responses no longer superimpose on noisy feedthrough of large magnitude, making the detection more robust. Finally, because the strength of the sensor resonant response correlates to its size, the decoupling of the excitation field from the sensor response allows miniaturization of the sensors.

Other methods of decoupling the transmit excitation field from the received resonant response are possible. The non-linearity in the properties of magnetoelastic materials can enable the generation of higher order resonances from a given sinusoidal excitation. In this case, filters can be used in the receive circuit to filter out the excitation energy from the resonant response. This enables the decoupling in the frequency domain. Another way of achieving the decoupling is through coil design. The transmit coil and the receive coil can be oriented in a manner that minimizes the coupling between the two. At the same time, the coupling between the resonant device and the coils must be substantial for a strong response.

## 1.4 Focus of this work

Magnetoelastic transduction has been used for decades for multifarious purposes across numerous application areas and, as such, is a mature technology in its own right. However, it has not been used for miniaturized sensors and actuators. The previous sections detailed the aspects

of magnetoelastic transducers that can have significant benefits and implications as implantable biomedical devices. The aim of this work is not only to propose and evaluate magnetoelastic devices that can compete with established technologies, but also explore new application areas where the unique abilities of magnetoelastic materials can be leveraged to provide significant benefits. Working towards these overarching goals, this dissertation encompass all facets of magnetoelastic transducer technology – sensing, actuation, and device measurement and characterization. Finally, based on the application areas described in Section 1.3, this dissertation focusses on the development of the following aspects of magnetoelastic transducers – strain sensors for biomechanical implants, actuators for GDDs, and improved methods of device characterization.

### 1.4.1 Wireless strain sensing

A new class of magnetoelastic strain sensors that utilize the $\Delta E$ effect of magnetoelastic materials is proposed for measurement of strains in biomechanical implants. Resonant detection renders the sensor output insensitive to the orientation of the interrogation coils. In addition, a novel architecture is used, allowing flexibility in setting the sensitivity and dynamic range specifications of the sensor.

### 1.4.2 Actuation of liquid flow on 3D surfaces

Passive, wireless, resonant magnetoelastic actuators intended for the generation of fluid flow on the surface of implantable Ahmed glaucoma drainage devices are investigated. The shear stresses generated directly by the actuator vibration and indirectly by the fluid agitation resulting from this vibration would potentially reduce the adhesion of fibroblasts and endothelial cells that are responsible for fibrosis. Particle flow and laser displacement measurements are used to characterize the device operation.

### 1.4.3 Measurement methods for resonant magnetoelastic devices

The overall goal is to improve the readout of magnetoelastic resonances by decoupling the excitation magnetic field from the resonant response. Three pathways for decoupling are explored – time domain, frequency domain, and interrogation coil design. Time domain decoupling is used in conjunction with a frequency-lock loop (FLL) to locate and track resonant frequencies of magnetoelastic devices. In addition, the time domain decoupling method is used to characterize the performance of wireless strain sensors. Frequency domain decoupling is achieved by utilizing the inherent non-linear mechanical and magnetic properties of magnetoelastic materials. The second harmonic mode of test resonators is excited and measured to effectively decouple the magnetic energy that is transmitted at the fundamental mode. Finally, interrogation coil designs are explored that can spatially isolate the excitation magnetic fields from the device response.

## 1.5 Organization of this report

Chapter 2 details the design, simulation and experimental results of magnetoelastic strain sensors for biomedical monitoring applications. Two sensor designs are described – single and differential. The differential sensor has the capability of compensating for changes in temperature.

Chapter 3 describes actuators for regulating fibrosis in glaucoma drainage implants. Six actuators are described in full detail – design, fabrication, and characterization.

Chapter 4 reports the development of improved methods of measurement of resonant magnetoelastic devices.

Finally, Chapter 5 concludes this report with the summary of inventions and possible directions of further research in this field.

# CHAPTER 2

## MICROMACHINED WIRELESS MAGNETOELASTIC STRAIN SENSORS

### 2.1 Introduction

Using magnetoelastic transduction, both resonant and non-resonant measurement approaches to strain sensor design are viable. Non-resonant sensing detects the change in magnetic coupling between the interrogation coils and the sensor due to applied strain. Strain applied to a magnetoelastic material results in magnetization and change in permeability through the Villari effect, which can then be detected using interrogation coils [Amo06, Ger00, Sav88, Tan12, Her01, Odu96, Shi99, Oes09]. A potential drawback of this technique is that the signal is susceptible to the geometry of the coil and its position relative to the magnetoelastic material.

Another phenomenon observed in magnetoelastic materials – magnetization-induced change in Young's modulus, i.e., the $\Delta E$ effect – can be exploited to provide a strain dependence to the resonant frequency. In [Hub12], two magnetoelastic strips held in close proximity were utilized together – one to provide a strain-dependent biasing field for the other, which served as the resonator. The dynamic range was limited by saturation magnetization of the biasing strip and was reported to be ±50 μstrain.

This chapter presents a passive, resonant, strain sensing approach based on the $\Delta E$ effect of magnetoelastic materials, where the strain is directly transferred to a doubly-anchored suspended resonating structure. Structural elements built into the resonator enable the extension of sensor dynamic range beyond the intrinsic capabilities of the magnetoelastic material. The

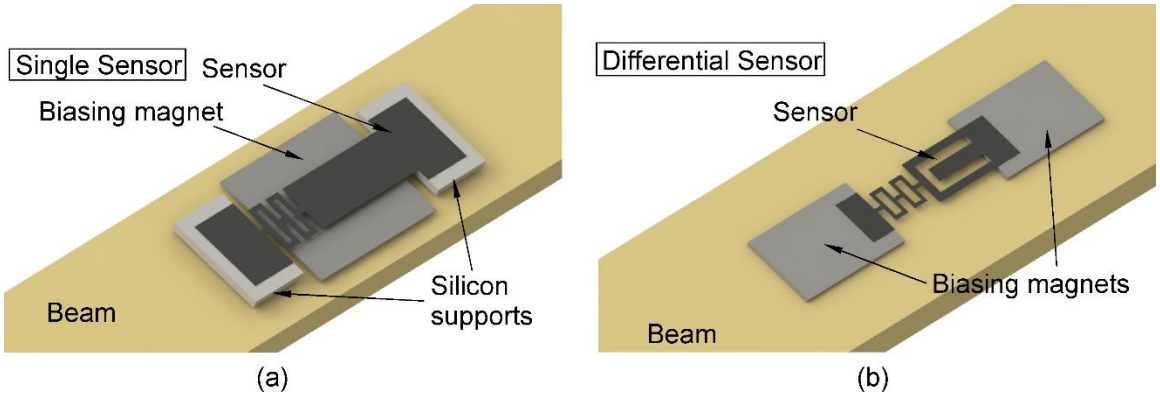


**Fig. 2.1:** (a) Assembly of the single sensor showing the silicon supports and bias magnet. (b) Differential sensor suspended on bias magnets with strain-independent cantilevered reference resonator. The sensors are fixed on a test beam.

resonant response of the structure is detected wirelessly through interrogation coils and is observed as a peak in the frequency spectrum of the coil voltage. Two sensor types are described – single and differential (Fig. 2.1). Both sensors include doubly-anchored resonant strips; the differential sensor has an additional cantilever exhibiting a strain-independent resonant response. The theory and modeling of the devices are outlined in section 2.2, followed by the design and fabrication in section 2.3. The experimental methods and results are described in section 2.4, and the discussion is presented in section 2.5.

## 2.2 Theory

### 2.2.1 The ΔE effect

In a magnetoelastic material under stress, strain is produced by two processes: the first is elastic strain (as produced in all materials); the second is from the Villari effect which represents magnetic moment rotation. In materials with strong spin-orbit coupling, rotation of magnetic moment results in rotation of electron clouds. If the electron charge cloud is anisotropically shaped, its rotation effectively results in strain [Cul09a]. The Young's modulus at a fixed DC magnetic bias field, $B_0$, can then be written as:

$$E|_{B_0} = \frac{\sigma}{\varepsilon_{el}+\varepsilon_{mag}} \tag{2.1}$$

where $\varepsilon_{el}$ is the elastic strain and $\varepsilon_{mag}$ is the strain due to material magnetization.

The $\varepsilon_{mag}$ component of strain reduces as the material is exposed to higher stress levels and consequently, the Young's modulus increases. Additionally, if the magnetic field or applied stress is such that the material is magnetically saturated, the only incremental contribution to strain is elastic, and the ΔE effect saturates. Figure 2.2 shows a typical stress-strain relationship and the slope of the stress-strain curve, i.e. Young's modulus, as a function of stress [Boz93]. Points A, B, C and D indicate different bias levels of the magnetic field that result in different responses. Tuning the biasing magnetic field or mechanically pre-stressing the sensor during attachment shifts the baseline operating point of the sensor. This property can be employed to allow measurement of both tensile and compressive strains.

### 2.2.3 Material considerations

In this work, the sensors are fabricated 29-μm-thick foils of Metglas 2826MB ($Fe_{40}Ni_{38}Mo_4B_{18}$). As an amorphous magnetoelastic alloy, Metglas 2826MB exhibits significant ΔE effect, with variations up to 20% of the nominal value [Tor78]. Other factors that contributed to the choice of thin-foil amorphous alloys are described in section 1.2.3.

The biasing magnetic field required for resonant operation of the sensor is provided by a permanent magnet made using 50 μm thick sheets of Arnokrome 5 (Arnold Magnetic Technologies Corp., Rochester, NY) – an iron-manganese alloy [Arn00]. It shows a remanence of 12-16 kG and a coercivity of 20-50 Oe. The high value of remanence would be beneficial for generating strong magnetic fields at small form factors.

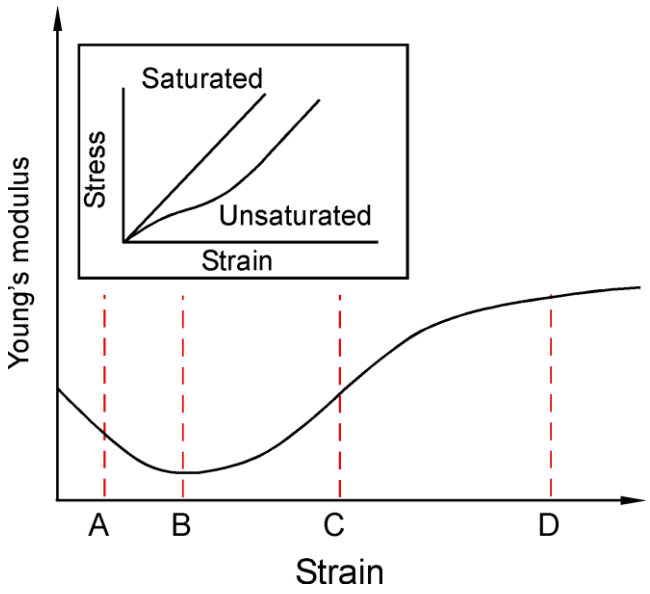


**Fig. 2.2:** Small-signal stiffness (slope of the stress-strain curve, shown in the inset) for a typical demagnetized specimen of a magnetoelastic material. Points A, B, C, and D are operating points under increasing magnitude of applied magnetic field.

## 2.3 Design and fabrication

### 2.3.1 Resonating elements

Two types of strain sensors are investigated in this effort – single and differential (Fig. 2.3). The sensing element for both types consists of a doubly-anchored suspended strip of Metglas 2826MB. It can be divided into two parts – a resonant strip and a spring. The spring serves to attenuate the strain in the resonant strip. This is necessary for sensor to provide a wide dynamic range, as the ΔE effect of magnetoelastic materials typically saturates at low levels of strains [Hub12]. Higher strains do not result in any appreciable change in stiffness and consequently no change in resonant frequency. While the geometry and boundary conditions of the sensors are such that both transverse (i.e. bending) and longitudinal modes exist, the first longitudinal mode of each sensor type is typically dominant in the wireless response of the sensor because it provides the largest unidirectional strain (i.e. mainly compressive or tensile at a given instant in time), which results in the strongest response magnetic field. The simultaneous presence of tensile and

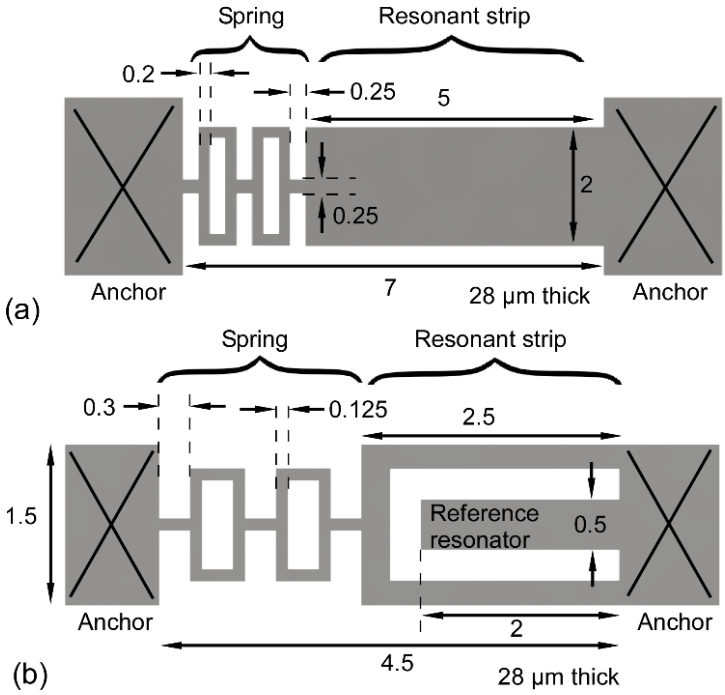


**Fig. 2.3:** Sensor designs: (a) Single sensor; (b) differential sensor. All dimensions in mm.

compressive strains in transverse modes of vibrations results in lower magnitudes of resultant magnetic fields.

In the single strain sensor, the resonating element is 5×2 $mm^2$ in area. This area determines the strength of the transmitted RF signal. The spring is 2×2 $mm^2$ in area, and is made with 200 μm wide elements. The entire structure is 28 μm thick. In the differential sensor, the sensing element is divided into two parallel sections. The sensing element in each section is 2.5×0.25 $mm^2$ whereas the shared spring element is 2×1 $mm^2$. The differential sensor also contains a reference resonator. This is a cantilever and is unaffected by any strain applied to the sensor. All elements are 28 μm thick. The reference resonator is helpful because the Young's modulus of the sensor material varies with temperature [Ber76, Hau78, Jai01]. This (common mode) variation in the absence of strain can be compensated by the response of the reference element. For small shifts in resonant frequency, $\Delta f$, to which a linear approximation can be applied:

$$\left.\frac{\Delta f}{f_0}\right|_{B_0}(\varepsilon, T) \approx S_T(\varepsilon)\Delta\varepsilon + S_\varepsilon(T)\Delta T \tag{2.2}$$

where $B_0$ is the biasing magnetic flux density through the resonating element, assumed to be invariant; $f_0$ is the baseline resonant frequency; $S_T(\varepsilon)$ is $\frac{\partial}{\partial\varepsilon}\left(\frac{\Delta f}{f_0}\right)_T$, the sensitivity to strain at constant temperature; and $S_\varepsilon(T)$ is $\frac{\partial}{\partial T}\left(\frac{\Delta f}{f_0}\right)_\varepsilon$, the sensitivity to temperature at constant strain. The term $S_\varepsilon(T)$ at zero strain is obtained from the response of the cantilever reference resonator in the differential device, whereas the sensing element of the differential sensor and the single sensor each provide the total sum. The $\Delta\varepsilon$, therefore, must be calculated from the sum. Of course, $\Delta\varepsilon$ itself has a temperature dependence based on the expansion mismatch between the sensor and the substrate to which it is attached. However, the calculated strain does not differentiate between thermal and mechanical sources of strain.

Initial experiments indicated that the ΔE effect of Metglas 2826MB saturates at about 50 μstrain. In this work, the springs were designed to limit the strain in the resonant strip to this value at the target strain of 2 mstrain on the entire sensor. Further, the sensors were sized to ensure that their resonant frequencies were within the excitation and detection range of the test setup. The compromise between sensor size and signal strength were also considered in selecting the final dimensions which are described in Fig. 2.3.

COMSOL Multiphysics 4.3 (COMSOL AB, Stockholm, Sweden) was used to simulate the resonant operation of the strain sensors. The coupled small signal equations 1.4 and 1.5 were implemented in a frequency domain simulation to determine the resonant frequencies and mode shapes of the sensors. Further details of the custom simulation model used are described in Appendix A. For the single sensor, the simulated resonant frequency was 230 kHz. For the differential sensor, the resonant frequency of the sensing element was 276 kHz, whereas the

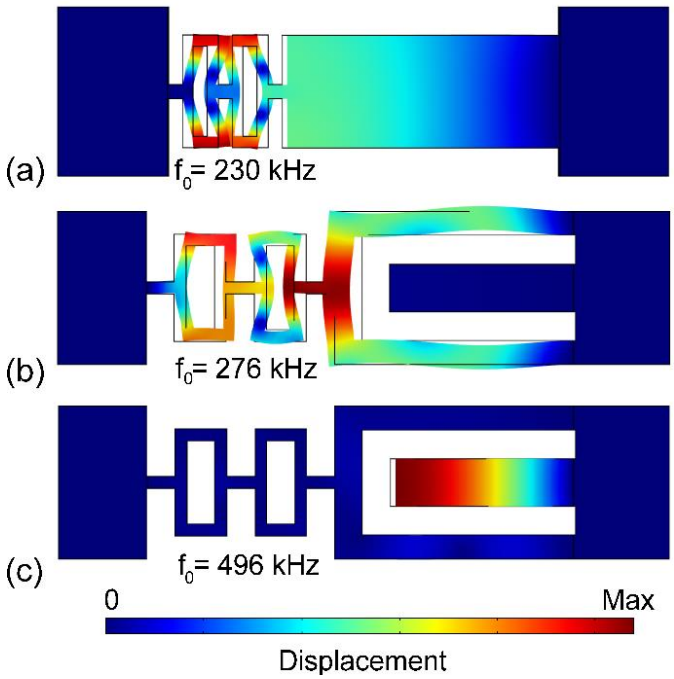


**Fig. 2.4:** Simulated mode shapes for single and differential sensor. (a) Single sensor, (b) differential sensor, sensing element, and (c) differential sensor, reference element. The Young's modulus was assumed to be 120 GPa in this simulation.

resonant frequency for the reference was 496 kHz. The simulated mode shapes for both the single and differential sensors are shown in Fig. 2.4.

The sensor shows a shift in resonant frequency shift not only due to ΔE effect but also because of a change in its equation of motion in presence of axial loads (i.e. strain stiffening). This is seen in all materials regardless of the magnetoelastic nature of the material. To analyze this effect of axial loading, a pre-stressed eigenfrequency simulation was performed for the sensors. In these simulations, the single sensor showed an estimated sensitivity of 2700 ppm/mstrain, while the differential sensor showed 1100 ppm/mstrain. These simulated sensitivities are due only to the strain stiffening effect.

Micro-electrodischarge machining (μEDM) is an attractive technique that can be used for serial or batch-mode micromachining any conductive material. This approach has been previously

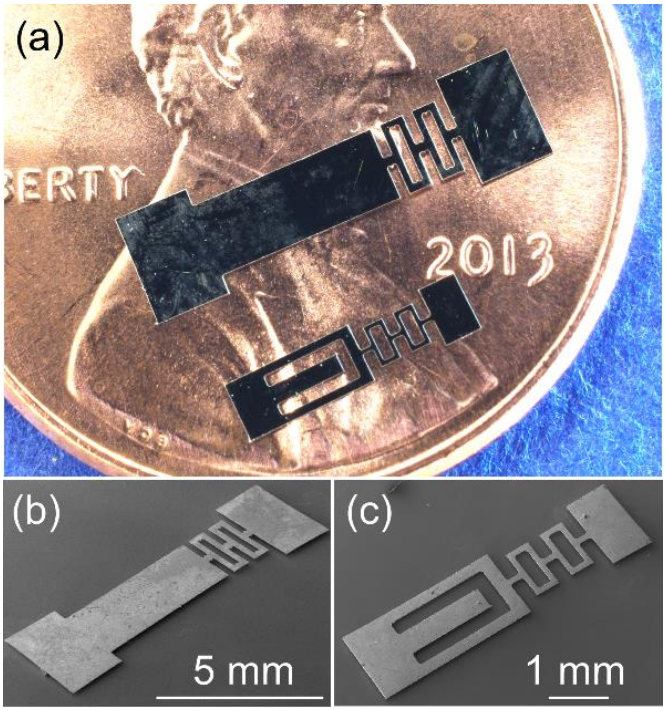


**Fig. 2.5:** (a) Microfabricated devices; (b) Single sensor; (c) Differential sensor

demonstrated for use in machining of Metglas 2826MB [Vis13]. In this effort, μEDM was used not only to fabricate the sensors, but also the biasing magnets that are described below. The fabricated sensors, single and differential, are shown in Fig. 2.5.

### 2.3.2 Biasing magnetic field and interrogation coils

To read out the sensor response, a system consisting of transmit and receive coils was employed (Fig. 2.6). The transmit coils were used to sweep a range of frequencies within which resonance was expected. The resonant frequency of the sensor was detected by an elevated response in the receive coil. In order to excite a longitudinal mode of vibration, the field lines generated by the transmit coil should loop through the sensor longitudinally. In order to minimize signal feedthrough, the receive coils must be positioned at a null point in the transmitted field. The transmit coils were 7 mm in diameter, 20 mm long, and had 10 turns each. The receive coils were 45 mm in diameter, 10 mm long and had 5 turns each. For this work, the sensor was held at a

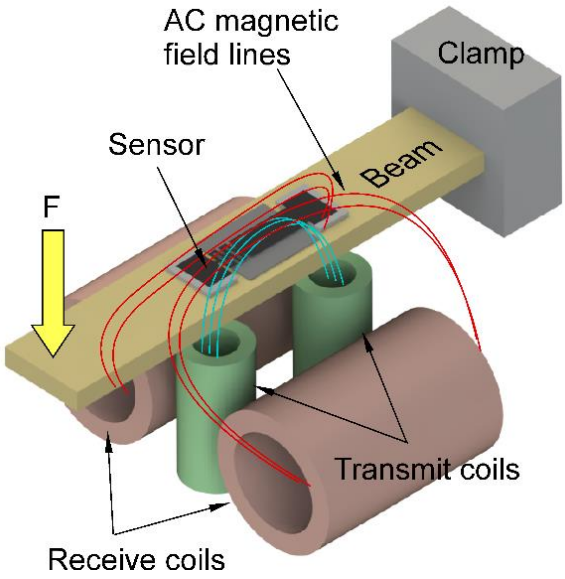


**Fig. 2.6:** Coil configuration and test setup used for sensor readout. Blue lines indicate field due to the transmit coil and red lines indicate the field as generated by the sensor and picked up by the receive coil.

distance of less than 5 mm from the transmit coil. An Agilent model 4395A network analyzer (Agilent Technologies, Santa Clara, CA) was used to read the voltage induced on the receive coil by the sensor response.

To determine the strength of biasing field necessary for device operation, the resonant frequency of the sensors was first experimentally determined using Helmholtz coils to provide the magnetic field. It was found that a biasing field of 5-10 Oe is sufficient for single sensor operation. The differential sensor, being smaller than the single sensor, required a stronger biasing field for operation [Che05]. For the differential sensor, a bias field of 15-20 Oe was necessary.

### 2.3.3 Sensor attachment

The single sensor was suspended across two supporting elements (300 μm thick silicon) that offset it from the beam. The longitudinally magnetized Arnokrome 5 bias magnet measuring 6×3 $mm^2$ was located underneath the suspended sensor. Cyanoacrylate adhesive was used for all

attachments. In the case of the differential sensor, to augment the strength of biasing magnetic field, a stack of three longitudinally magnetized Arnokrome 5 magnets was used as the support at each end of the sensor. The magnets each measured 4×2.5 $mm^2$. As the magnets were in direct contact with the sensor, a larger bias field was provided for sensor operation. Based on magnetometer readings (Model 5180, F. W. Bell, Milwaukie, OR), the magnets provided an estimated 5-10 Oe field required for single sensor and 15-20 Oe field required for the differential sensor. The sensor assemblies for the single and differential sensors are shown in Fig. 2.3.

## 2.4 Experimental methods and results

For testing, the sensors and the biasing magnets were attached to the upper surface of brass cantilevers. The free ends of the cantilevers were pushed down using a force gage (Fig. 2.6). To calibrate the force used with the strain generated on the beam surface, a commercial strain gage (SGD-5/350-LY13, one-axis general purpose strain gage, Omega Engineering, Inc., Stamford, CT) was first used on the cantilever setup. The reported data is the strain on the beam surface.

The temperature dependence tests were conducted by heating the sensor assembly on a hot plate. Temperature measurements were taken using a thermocouple (Type K, model 5SRTC, Omega Engineering, Inc., Stamford, CT) affixed to the brass beams near the sensors.

### 2.4.1 Single sensor

The typical single sensor showed an unstrained resonance at 230.8 kHz at 23˚C (Fig. 2.7(a)). Under applied tensile strain of 1.05 mstrain, the resonant frequency increased to 233.8 kHz. The typical resonance amplitude for the unstrained single sensor was 150 μV; under maximum strain the amplitude reduced to about 50 μV. The decrease in signal amplitude was

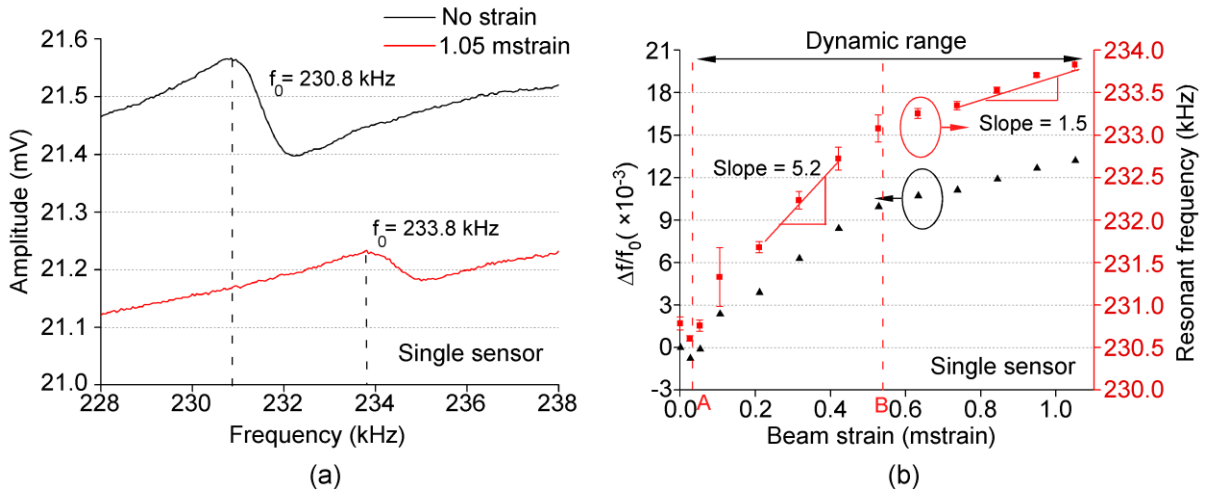


**Fig. 2.7:** (a) Resonance of the single sensor at 23˚C under no strain and 1.05 mstrain. (b) Resonant frequency and fractional change in resonant frequency as a function of beam strain for a single sensor at 23˚C.

consistent with expectations because the small signal magnetostrictivity, *d*, reduces at higher strain levels.

The typical change of resonant frequency as a function of strain is shown in Fig. 2.7(b). The average sensitivity over this range was typically about $13\times10^3$ ppm/mstrain. The slope at higher strain levels decreases from a maximum value of 5.2 kHz/mstrain to 1.5 kHz/mstrain. This indicates saturation of ΔE effect as shown in Fig. 2.7(b). The initial decrease in resonant frequency at small strains can be attributed to the ΔE effect: the localized slope of the stress-strain curve (i.e. the incremental stiffness) does not monotonically increase with applied strain at low levels of strain [Boz93]. This is corroborated by experiments done on similar amorphous alloys [Ber76]. Taking into account the decrease in resonant frequency at lower strains, the single sensors typically showed a dynamic range of 0.05-1.05 mstrain.

### 2.4.2 Differential sensor

For the differential sensor, a typical unstrained resonance for the sensing element was at about 266.4 kHz at 23˚C (Fig. 2.8(a)). Under applied tensile strain of 1.85 mstrain, the resonant frequency increased to 272.5 kHz resulting in a sensitivity of $12.5\times10^3$ ppm/mstrain. As expected, the amplitude of resonance for the sensing element reduced with increasing strain: the baseline resonance amplitude was 150 μV, while at maximum applied strain the amplitude was less than 10 μV. The reference resonance was at 492.75 kHz. It was experimentally verified that this frequency did not change with applied strains.

The dependence of resonant frequency on applied strain for the sensing element is shown in Fig. 2.8(b). Unlike the single sensor, the differential sensor did not show a reduction in resonant frequency at strains below 0.05 mstrain. This was because the sensor was biased by a stronger magnetic field at an operating point above the initial dip in stiffness. As was the case with the single sensor, the differential sensor showed a reduced sensitivity at higher strain levels: it fell

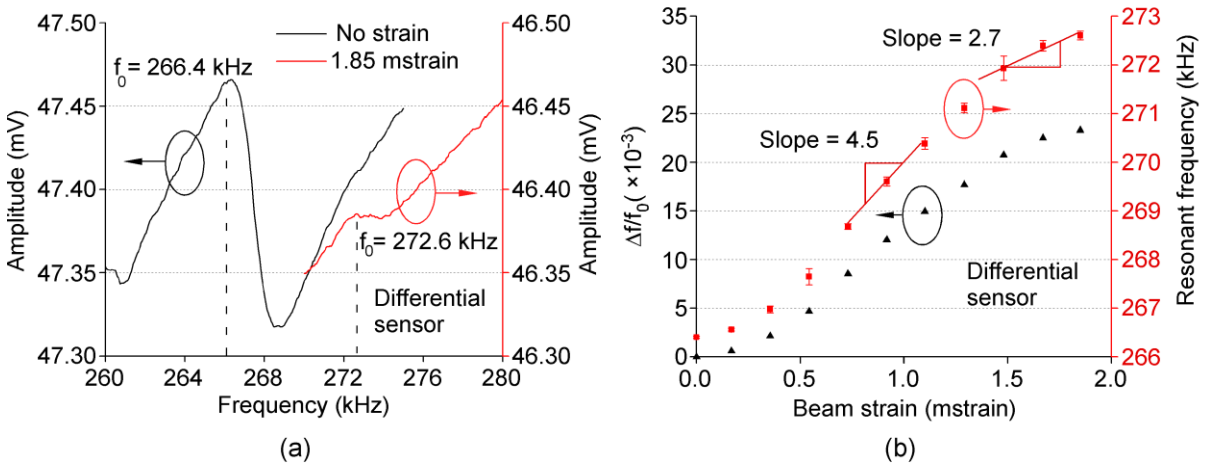


**Fig. 2.8:** (a) Resonance of the sensing element of the differential sensor at no strain and 1.85 mstrain at 23 ˚C. (b) Resonant frequency and fractional change in resonant frequency as a function of beam strain for the sensing element of the differential sensor at 23˚C.

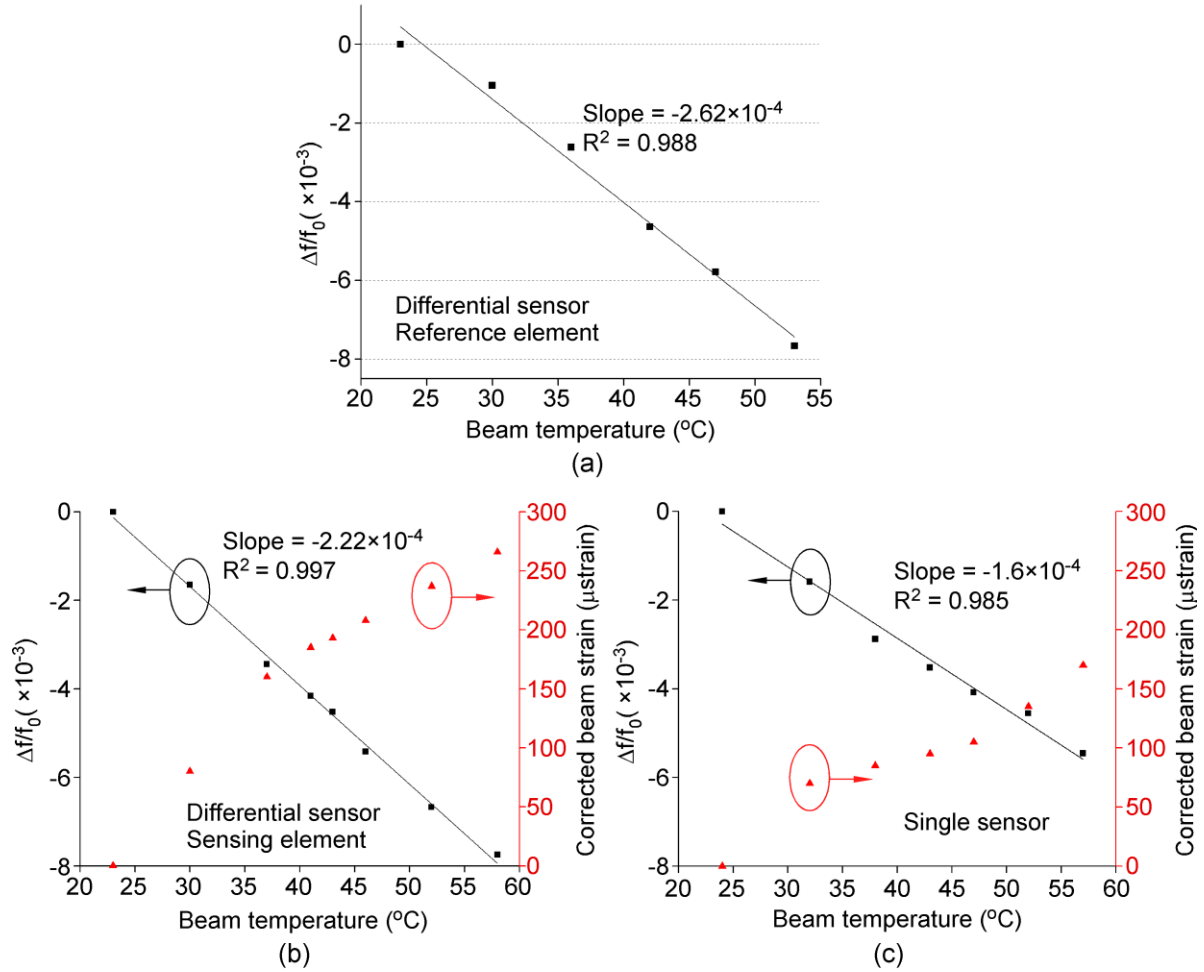


**Fig. 2.9:** Temperature compensation as used in differential and single sensor. (a) Fractional change in resonant frequency of the reference resonator as a function of the temperature of the brass beam. (b) Fractional change in resonant frequency of sensing element of the differential sensor and corrected beam strain as a function of temperature. (c) Fractional change in resonant frequency of the single sensor and corrected beam strain as a function of temperature.

from a maximum slope of 4.5 kHz/mstrain to 2.7 kHz/mstrain. These measurements were taken at 23˚C.

Over the range of temperatures approximately from 20˚C to 60˚C, the resonant frequency of the reference cantilever varied by -262 ppm/˚C (Fig. 2.9(a)), and that of the sensing element varied by -222 ppm/˚C uncorrected by the output of the reference element (Fig. 2.9(b)). Based on this and equation (2.4), the true strain observed in the sensor is plotted in the right axis of Fig.

2.9(b). If the temperature compensation provided by the cantilever is applied to the simple sensor, its temperature coefficient of resonant frequency changes from -160 ppm/˚C uncorrected to 102 ppm/˚C corrected (Fig. 2.9(c)).

## 2.5 Discussion

In case of the single sensor, there is an initial reduction in resonant frequency at strain values below 0.05 mstrain. The dynamic range can be extended to lower values by increasing the biasing magnetic field, shifting the baseline resonant frequency to a point in the response plot that is above this dip. It can be seen in Fig. 2.7(b) shows how initial magnetization or strain can affect the ΔE behavior of magnetoelastic materials and be applied to the strain sensor. A magnetic bias or applied pre-strain can move the baseline operating point to A, where the sensor will show continuous increase with applied strain. Using an even stronger field or higher pre-strain can move the baseline operating point to point B, where the sensor can detect both tensile and compressive strains. It can be seen in Fig. 2.8(b) how the experiments for the differential sensor demonstrate this – the magnetic field bias provides an operating point where there is no decrease in resonant frequency with increasing strains.

As described in section 2.3.1, a shift in resonant frequency of the device can occur due to strain stiffening. Finite element analysis shows that for the single and differential sensors described in this work, the non-magnetic contributions are 2700 ppm/mstrain and 1100 ppm/mstrain respectively. These are minor compared to the overall measured sensitivity of $13\times10^3$ ppm/mstrain for the single sensor and $12.5\times10^3$ ppm/mstrain for the differential sensor. Hence, it can be concluded that it is indeed the ΔE effect which primarily determines the sensitivity of these devices.

In general, a change in temperature affects the resonant frequency of a cantilever through change in Young's modulus or dimension change due to thermal expansion. For a cantilever resonating in the longitudinal mode, the resonant frequency is given by:

$$f_0 = \frac{1}{4L}\sqrt{\frac{E}{\rho(1-\nu^2)}} \tag{2.3}$$

where, $E$ is the Young's modulus, $\rho$ is the density, $\nu$ is the Poisson's ratio, $L$ is the length of the cantilever. The fractional change in resonant frequency resulting from a temperature change can be expressed as:

$$S_\varepsilon(T)\Delta T = \frac{\frac{1}{4L(1+\alpha_{TE}\Delta T)}\sqrt{\frac{E(1+\alpha_\gamma \Delta T)(1+\alpha_{TE}\Delta T)^3}{\rho(1-\nu^2)}} - \frac{1}{4L}\sqrt{\frac{E}{\rho(1-\nu^2)}}}{\frac{1}{4L}\sqrt{\frac{E}{\rho(1-\nu^2)}}} \tag{2.4}$$

$\Delta T$ is the temperature change, $\alpha_{TE}$ is the thermal expansion coefficient of Metglas 2826MB and $\alpha_\gamma$ is the fractional change, with temperature, in the Young's modulus of Metglas 2826MB. However, $\alpha_{TE}$ is 12 ppm/˚C – negligible compared to measured $\Delta f/f_0$ – and can thus be ignored for the temperature range under consideration. Equation (2.6) then simplifies to:

$$S_\varepsilon(T) \approx \frac{1}{\Delta T}\left(\sqrt{(1+\alpha_\gamma \Delta T)} - 1\right) \approx \frac{\alpha_\gamma}{2} \tag{2.5}$$

From experimental results, $S_\varepsilon(T)$ for the reference element in the differential sensor is -262 ppm/˚C which implies that $\alpha_\gamma$ is -524 ppm/˚C.

The Young's modulus of 2826MB reduces with increasing temperature, lowering the resonant frequency. In contrast, the expansion mismatch of brass and 2826MB, which have thermal expansion coefficients of 19 ppm/˚C and 12 ppm/˚C, respectively, results in tensile strain, assuming that the strain sensor and the brass beam are at similar temperatures. Hence, these factors influence the resonant frequency of the sensors in opposing manner. For the single sensor, there

is a decrease of 1.27 kHz in the resonant frequency for a 35˚C increase in temperature. The substantial decrease in resonant frequency with increasing temperature indicates that the decrease in Young's modulus of 2826MB is the dominant parameter influencing the resonant frequency. Considering that the full range of frequencies for the single sensor, observed over the range of applied strain, is about 3 kHz, it is necessary for the temperature variation to be factored into the measurement. For the differential sensor, the sensor resonant frequency falls by 1.85 kHz for a 35˚C increase in temperature. Temperature compensation using the response of the reference resonator enables the calculation of the tensile strain caused by the temperature change. In these experiments, the differential sensor and single sensor showed a strain dependence on temperature of 7.45 μstrain/˚C (ppm/˚C) and 4.52 μstrain/˚C (ppm/˚C), respectively. This corresponds well with the theoretical expansion mismatch between brass and 2826MB of 7 ppm/˚C.

The device operation relies on the magnetic circuit formed by the transmit and receive coil with the sensor. If the sensor rests on a ferromagnetic substrate, it can potentially influence this magnetic circuit. However, the permeability of Metglas 2826MB is much higher than most ferromagnetic materials and the effect of the substrate on sensor read-out will be accommodated by an appropriate calibration on a similar substrate.

The signal quality of the sensor output may be improved in the long term by employing strategies to exploit higher harmonics of the resonant response, thereby reducing feedthrough of the interrogating signal. Pulsed interrogation methods may also reduce signal feedthrough. In addition, the interrogation range can be increased by using larger coils and higher input power for the transmit coils.

A comparison of the performance of the wireless strain sensor reported in this work with previously reported devices is shown in Table 2.1. Resonant operation, a design that can be

adjusted to vary sensitivity and dynamic range, and a small footprint are some of the advantages of the sensors reported in this chapter over other passive strain sensors.

TABLE 2.1: COMPARISON OF PASSIVE STRAIN SENSORS

| | **Type** | **Sensitivity** | **Dynamic range** | **Footprint** |
|---|---|---|---|---|
| Jia *et al.* [Jia06] | Resonant LC | $0.981\times10^3$ ppm/mstrain | 18 mstrain | 8100 $mm^2$ |
| Oduncu *et al.* [Odu96] | Non-resonant magnetoelastic | $166\times10^3$ ppm/mstrain | 2.4 mstrain | 80 $mm^2$ |
| Huber *et al.* [Hub12] | Resonant magnetoelastic | $380\times10^3$ ppm/mstrain | 50 μstrain | 450 $mm^2$ |
| This work | Resonant magnetoelastic | $12.5\text{-}13.0\times10^3$ ppm/mstrain | Up to 1.85 mstrain | As small as 10 $mm^2$ |

## 2.6 Summary

This chapter presents the design, fabrication and experimental results of passive, wireless magnetoelastic strain sensors. Using the ΔE effect of magnetoelastic materials, the devices detect strain as a change in its resonant frequency. The single sensor incorporates only a sensing element, whereas the differential sensor incorporates both a sensing element and a reference resonator. Both sensors use spring structures to attenuate the strain in the sensing element. This architecture allows the sensitivity and dynamic range to be customized. The sensors can be used to measure both tensile and compressive strains by mechanical pre-stressing or by selecting an appropriate magnetic bias field. In the differential sensor, the output of the reference resonator can be used to compensate for resonant frequency change due to the temperature dependence of the Young's modulus of Metglas 2826MB.

# CHAPTER 3

# RESONANT MAGNETOELASTIC MICROSTRUCTURES FOR WIRELESS ACTUATION OF LIQUID FLOW AND APPLICATION TO GLAUCOMA DRAINAGE DEVICES

## 3.1 Introduction

The Ahmed glaucoma drainage device (AGDD) (New World Medical Inc., Rancho Cucamonga, CA) uses a drainage tube that permits the flow of fluid out of the eye when the IOP exceeds a certain threshold. The tube drains AH into the space created by the plate body, located in a subconjunctival space over the sclera (Fig. 3.1(a)). Over time, a fibrous capsule of tissue, or "bleb," is formed around the AGDD, serving as a reservoir for the extra AH that drains from the eye. In a subset of patients, the fibrous capsule significantly reduces the permeability to AH, which, in turn, increases the resistance to AH outflow (Fig. 3.1(b)). The increased resistance to AH outflow has a cascading effect that culminates in elevated IOP.

We envision that magnetoelastic actuators can be integrated with GDDs to limit cellular adhesion on the implant surface. The actuator could be either embedded within the GDD or affixed to it prior to surgical implantation. The shear stresses generated directly by the vibration of the actuator and indirectly by the fluid agitation resulting from this vibration would reduce the adhesion of fibroblasts and endothelial cells [Tit12, Ito11, Tru90]. As a result, the actuation would impede complete encapsulation by preventing cells from adhering to large portions of the implant. This is expected to increase the permeability of the surrounding tissue to the AH draining from the AGDD, enabling the AGDD to better control the IOP. Post-implantation, the actuator could be

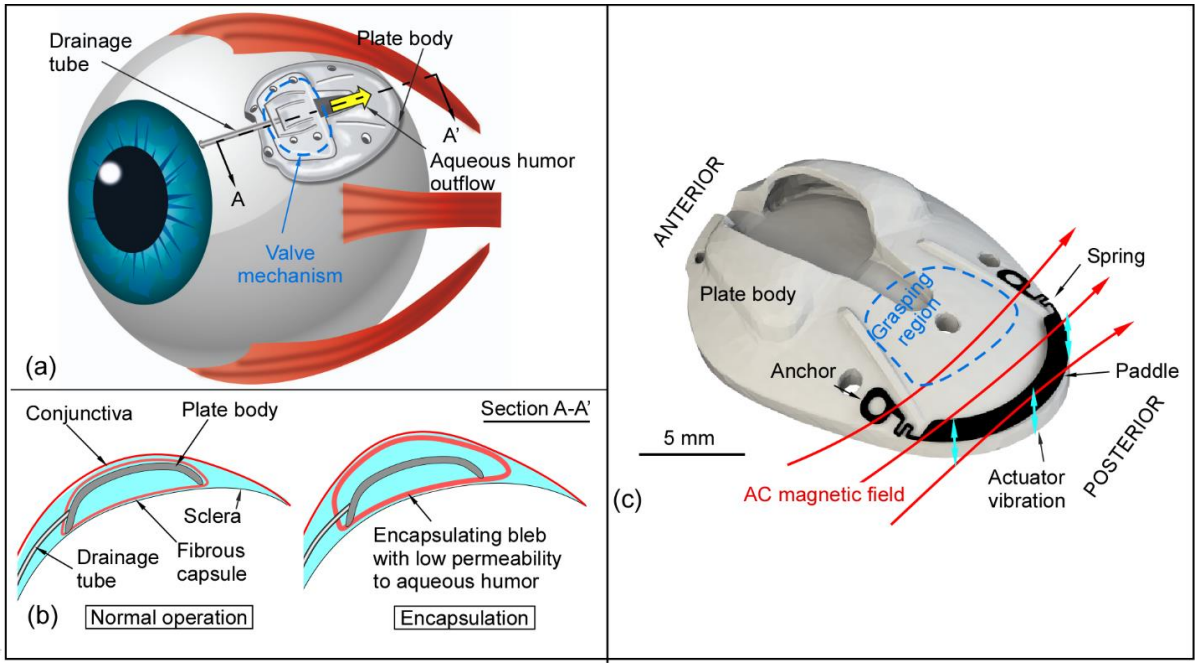


**Fig. 3.1:** (a) Implantation of the Ahmed glaucoma drainage device. The conjunctiva is not shown for clarity. (b) Cross section of the implant showing the formation of the bleb, which serves as a reservoir for aqueous humor exiting the eyeball. As pictured on the right, a thick, encapsulated bleb with low permeability to aqueous humor results in the inability of the device to drain aqueous humor as intended, leading to an elevated IOP. (c) A magnetoelastic actuator (Type *A*) attached to the plate body.

deployed periodically – perhaps for only a few minutes per day – using a small external coil to generate an oscillating magnetic field. The external coil, positioned a few centimeters from the implant, would need to generate only a weak magnetic field (< 20 G) and could even be embedded in a toothbrush or a wearable device. This procedure could be safely administered by the patient or a caregiver with minimal instruction.

The fabrication of complex 3D geometries and curved surfaces using planar magnetoelastic foils remains challenging. This is especially important for implantable applications where such shapes are necessary to conform to biological features and devices like the AGDD. Whereas the vast majority of reported magnetoelastic devices have been planar, a few curved structures have been described for use in sensing applications [Gre09a, Gre10, Kou00b]. These three-dimensional

(3D), out-of-plane geometries have been achieved by thermal annealing or by inducing elastic or plastic deformations. However, until now, these geometries have been limited to simple, single-axis curvatures. For instance, sensors reported for detecting occlusions in biliary stents had tubular curvatures to match stent geometry [Gre09a].

This chapter describes the design, fabrication, and *in vitro* experimental results of actuators using amorphous magnetoelastic materials. The actuators have customized 3D shapes and curvatures that conform to an AGDD, (Fig. 3.1(c)). Six actuator designs are evaluated, with varying implant coverage areas and resonant frequencies. The design and modeling are described in section 3.2 followed by fabrication in section 3.3. Experimental methods and results are presented in section 3.4, and the discussion and summary are presented in sections 3.5 and 3.6, respectively.

## 3.2 Design and modeling

### 3.2.1 Design

The complex geometry of the AGDD warrants special considerations for actuator development. The actuator should closely conform to the AGDD surface to avoid changes to the manner in which the device fits the eye and to prevent any damage to the surrounding ocular tissue. This is a design and fabrication issue because amorphous magnetoelastic materials, from which the actuators are patterned, are generally available only as flat foils. The design of the actuator must also accommodate various features on the AGDD (Fig. 3.1(c)). Three perforations in the posterior portion of the implant allow the growth of fibrous tissue that "rivets" the plate body of the implant to the scleral surface on which it rests, whereas two are located in the anterior portion for suturing the implant in place. In addition, there are two ridges located on the posterior of the implant. The actuator design must avoid both the perforations and ridges on the plate surface.

Additionally, there are considerations related to the handling of the AGDD during the implantation procedure. During the implantation procedure, the AGDD is grasped with forceps by the surgeon (on the portion of the device posterior to the valve mechanism) and placed under the conjunctiva before it is sutured to the sclera. The actuator should avoid the area of the plate body where the forceps are typically positioned during this procedure.

To enable the design, fabrication and simulation of the complex actuator geometry, a 3D model of the AGDD was necessary. An AGDD was scanned using a Scanco μCT 100 micro-computed tomography (μCT) system. A software package (Mimics 14, Materialise NV, Leuven, Belgium) was used to create a 3D mesh from the scan data, which could then be imported into CAD and FEA tools. Another software module (3-Matic 9, Materialise NV, Leuven, Belgium) was then used to repair the mesh and remove any imperfections and artifacts caused by the scanning process. The AGDD model that was created from the CT scan data is shown in Fig. 3.1(c).

Six actuator designs were evaluated, each covering different areas on the AGDD. The actuators were designed for fabrication from 29-μm-thick foils of an amorphous magnetoelastic alloy and, hence, are of this same thickness. Each of the actuators includes three types of elements – paddles, anchors, and springs. The Type *A* design consists of a paddle circumscribing the posterior (downstream) portion of the plate body (Fig. 3.2(a)). The resonant vibration of this paddle causes agitation and flow in the fluid in which it is immersed. The outer radius of the paddle is 5.1 mm, and the inner radius is 4.2 mm, making the width approximately 1 mm. Both ends of the paddle are attached to compliant segments to relieve the stress from the anchors. The compliant segments are folded structures measuring 125 μm wide, with the entire suspension on each side measuring $1.6 \times 0.75$ mm$^2$. Attached to the springs are anchors measuring $1.3 \times 1.3$

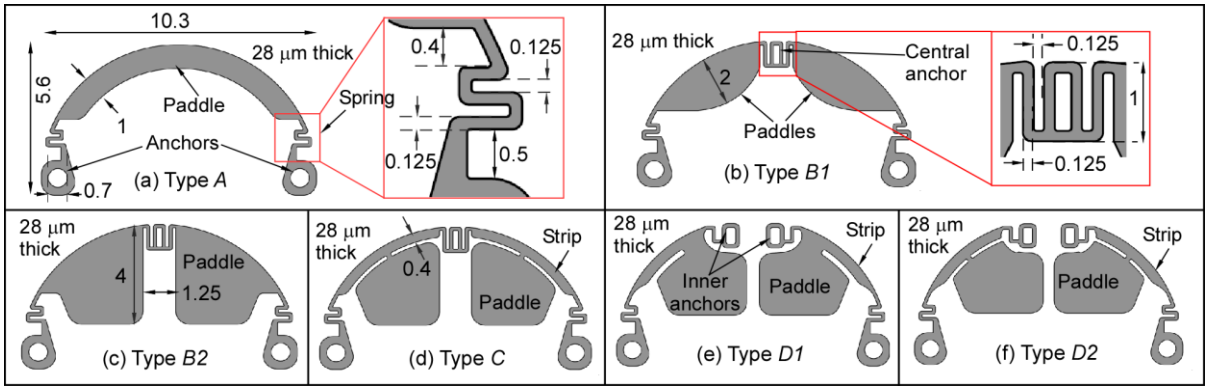


**Fig. 3.2:** Dimensions of the six actuator designs (in mm).

mm$^2$, each with a perforation measuring 0.7 mm in diameter. To anchor the actuator, an adhesive is used that, once hardened, will rivet the anchor to the plate body. The entire actuator footprint measures 10.3 × 5.6 mm$^2$ on a planar foil.

Type *B* includes two similar designs with increased coverage of the plate body (Fig. 2(b) and (c)). In addition, a central anchor is provided for added security during implantation when the AGDD is pushed underneath the conjunctiva with the forceps. The anchor measures 1.3 × 1 mm$^2$ and is made of beam elements that are 125 μm wide. For Type *B1*, the paddles measure approximately 2 mm wide at the widest point (Fig. 3.2(b)), whereas for Type *B2*, they measure 4 mm at the widest point (Fig. 3.2(c)). The outer springs and anchors are identical to those of the Type *A* actuator. Both designs measure approximately 10.3 × 5.6 mm$^2$.

Type *C* is a hybrid of Types *A* and *B*, with wide paddles attached to a thin strip circumscribing a portion of the posterior of the plate body, divided by the central anchor (Fig. 3.2(d)). The central anchor is identical to that in the Type *B* actuators. The outer radius of the strip is 5.1 mm, and the inner radius is 4.7 mm, making the strip approximately 0.4 mm wide. The paddles attached to the spring measure 3.25 mm at the widest point. The outer anchors and springs are identical to those of the previous actuators. The entire actuator measures 10.3 × 5.6 mm$^2$.

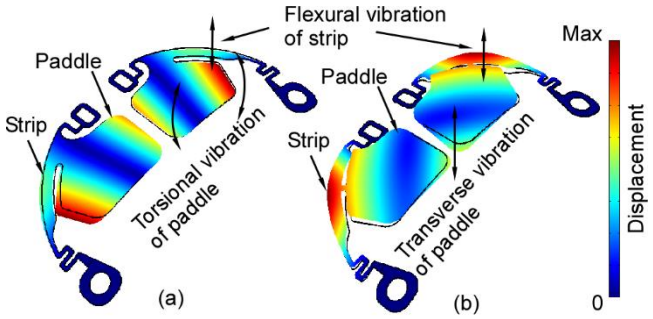


**Fig. 3.3:** Target resonant modes for Type *D* actuators: (a) Type *D1* and (b) Type *D2*. The different points of attachment of the paddles to the strip result in different paddle vibration modes.

Finally, Type *D* includes two designs with physically separate paddles on each half of the AGDD (Fig. 3.2(e) and (f)). Each paddle is attached to a strip that circumscribes a portion of the plate body, with one end of the strip attached to the outer springs and anchor and the other end attached to the inner spring and anchor. Types *D1* and *D2* differ on the point of attachment to the strip. In Type *D1*, the attachment is located toward the end of the strip: a flexural motion of the strip results in a torsional motion of the paddle (Fig. 3.3(a)). Type *D2* has a central attachment: a flexural motion of the strip results in a transverse motion of the paddles (Fig. 3.3(b)). For both designs, the outer radius of the strip is 5.1 mm and the inner radius is 4.7 mm, making the strip approximately 0.4 mm wide. The inner anchors measure $1 \times 0.7$ mm$^2$ for each of the paddles in both designs. The inner springs measure $0.7 \times 0.6$ mm$^2$ and are made from beam elements that are 125 μm wide. The outer anchors and springs for each of the paddles are identical to those of the previous actuators. The entire actuator measures $10.3 \times 5.6$ mm$^2$.

The overall dimensions of the actuators are designed to fit the Model FP7 AGDD. A meandering shape for the spring provides compliance within a small form factor. The width of the folded structures that make up the compliant spring elements (i.e., 125 μm) represents the lower limit of the photochemical machining fabrication process used, further details of which are

provided in section 3.3. The anchors are designed to be sufficiently large to allow easy manual attachment. The variations in the features of the different actuator types are designed to provide empirical information on the value of these various features. Type *B* designs have a larger area over the valve plate body than the Type *A* design to determine the impact of this area on the flow. Type *C* actuator paddles are attached to the strip to determine the impact on paddle compliance and the vibration displacement amplitude. Type *D* designs have physically separate paddles on each half of the AGDD to accommodate any deformation of the soft AGDD plate body.

The flexibility of the AGDD plate body is an important feature of the AGDD that enhances its performance [Mac07]. The compliant spring elements of the actuator, the overall thin structure, and the fact that there are only two or three anchor points ensure that the flexibility of the AGDD plate body is not compromised. Through finite element simulations in COMSOL Multiphysics 4.4, the out-of-plane compliance of the Type *A* actuator was estimated to be nearly six orders of magnitude higher than that of the plate body. Finally, by locating the actuator sufficiently far from the valve mechanism, potential interference with this mechanism is avoided.

### 3.2.2 Modeling

The resonant behavior of the actuators was simulated in COMSOL Multiphysics 4.4. Coupled solid mechanics and magnetic field physics (approximated by equations 1.4 and 1.5) were used to simulate the behavior of the magnetoelastic material in an oscillating magnetic field. The mechanical and magnetic properties used in this simulation were derived from manufacturer data sheets and previous reports [Met00, Gut13, Lia07]. The damping due to the liquid environment was obtained experimentally from laser displacement meter measurements performed on the final fabricated actuators. The details of this method are provided in section 3.5.

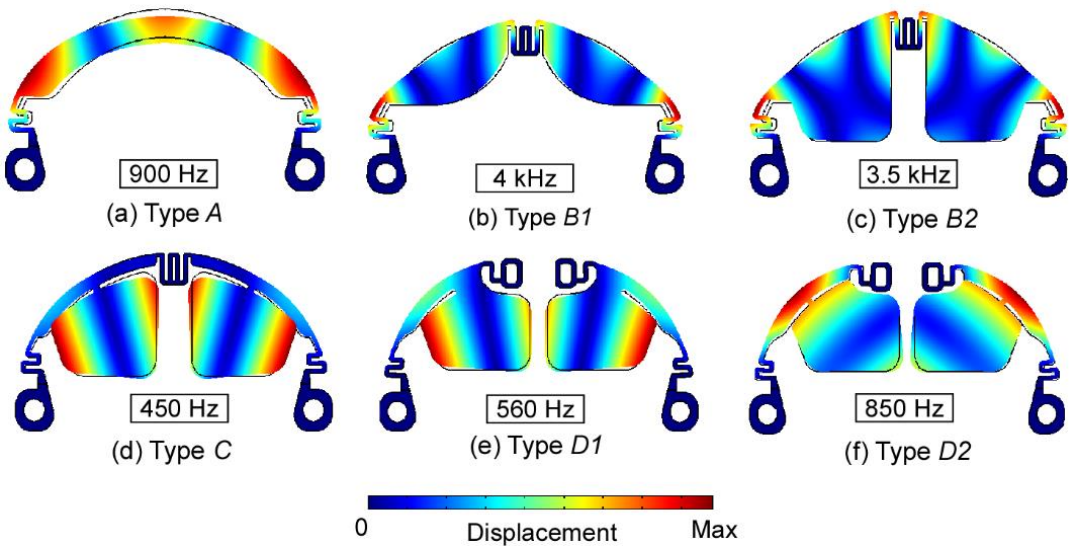


**Fig. 3.4:** Simulated resonant frequencies and corresponding mode shapes showing maximum vibration amplitudes.

The resonant frequencies and mode shapes exhibiting the maximum vibration amplitudes are shown in Fig. 3.4. The simulations predicted multiple flexural modes for Type *A* actuators, with the third mode (at 900 Hz) exhibiting the maximum resonant amplitudes. For Type *B*, the resonant frequencies with the largest displacements were 4 kHz and 3.5 kHz for Types *B1* and *B2*, respectively. The Type *C* actuator had a low resonant frequency of 450 Hz that resulted in large displacements. For Type *D* actuators, target resonant modes were identified at 560 Hz and 850 Hz for Types *D1* and *D2*, respectively.

## 3.3 Fabrication

For this work, the actuators were fabricated from 29-μm-thick foils of Metglas 2826MB ($Fe_{40}Ni_{38}Mo_4B_{18}$). The fabrication of the actuators is a two-step process: patterning of the thin-film magnetoelastic alloy, followed by thermal annealing to induce the desired curvature. The actuators are patterned from flat sheets of Metglas 2826MB using PCM (Kemac Technology, Inc., Azusa, CA). In this process, the foil is first coated with a photoresist, which is lithographically

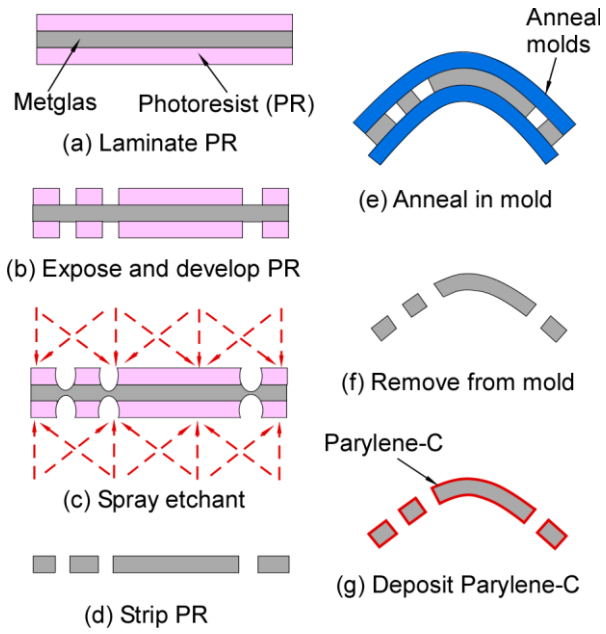


**Fig. 3.5:** Process flow for actuator fabrication. Steps (a)-(d) result in the patterning of the magnetoelastic foil. Steps (e)-(g) impart the required curvature and biocompatibility.

patterned by ultraviolet exposure. The exposed regions of the substrate (not covered by the mask) are then etched away using a spray of etchant. Advantages of this technique include burr-free fabrication and retention of the magnetic properties of the material. The process flow for PCM is shown in Fig. 3.5(a)-(d).

To obtain an actuator with the necessary curvature, a patterned sheet of Metglas 2826MB must be annealed in a mold at elevated temperature to remove the stress induced by the applied curvature. A longer annealing duration or higher temperature causes the initially flat structure to more closely conform to the curvature of the annealing mold. The disadvantage is that a higher temperature also results in embrittlement. Furthermore, a temperature that is too high can also lead to crystallization of the material or loss of ferromagnetism (if it exceeds the Curie point), resulting in a reduction in permeability [Liv81]. The Curie temperature for Metglas 2826MB is 353°C, and its temperature of crystallization is 440°C [Has78, Tor78]. Conversely, a shorter annealing duration or lower temperature prevents the shape of the mold from being completely


**Fig. 3.6:** Fabricated actuators after photochemical machining and annealing: (a) Type *A*, (b) Type *B1*, (c) Type *B2*, (d) Type *C*, (e) Type *D1*, and (f) Type *D2*.

transferred to the final actuator. Preliminary experiments focused on inducing curvature in the actuators indicated that the recoil is 25-40% of the target deformation upon removal from the mold. The shape of the mold must account for this partial recoil. For this study, it was found that annealing at 275°C for 12 hours in a mold with an exaggerated curvature yielded a desirable outcome. It is important that the curvature of the actuator conform to the AGDD. Inexact curvature can result in damage to the surrounding tissue, difficulty in surgical implantation of the device, and reduced actuation efficacy due to the larger separation from the implant surface.

The annealing mold consisted of two plates (with exaggerated curvatures) between which a PCM-patterned sheet of Metglas 2826MB was sandwiched during the annealing process (Fig. 3.5(e)). The annealed actuators were then coated with a 1-μm-thick layer of Parylene-C to prevent corrosion in the aqueous testing environment and to provide *in vivo* biocompatibility [Sch88] (Fig. 3.5(g)). The as-fabricated actuators (prior to annealing) and the annealed actuators are shown in Fig. 3.6.

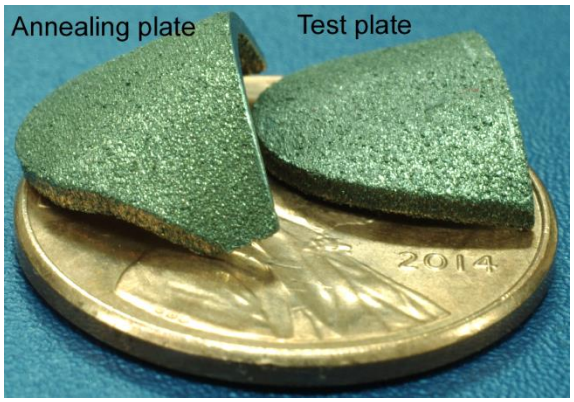


**Fig. 3.7:** Fabricated plates for annealing and actuator testing. Each patterned foil of Metglas 2826MB was sandwiched between two annealing plates during the annealing process. The test plate mimicked the curvature of the AGDD.

The plates used for annealing were designed based on the 3D scanned model of the AGDD and fabricated by direct metal laser sintering (DMLS) of a cobalt-chrome alloy (GPI Prototype and Manufacturing Services, Lake Bluff, IL). In the DMLS process, which is an additive manufacturing process, a laser is used to sinter powdered metal layer by layer to create the required solid structure [Aga95]. In addition to the plates used for annealing, DMLS was also used to fabricate test plates that mimicked the curvature of the AGDD. During the experimental measurements, the actuators were attached to these test plates to replicate the curvature of the AGDD. The fabricated plates used for annealing and testing are shown in Fig. 3.7.

## 3.4 Experimental methods and results

The annealed and coated actuators were experimentally evaluated using an optical approach to determine the resonant modes that generated the maximum liquid motion. Each actuator was placed in an aqueous suspension of 3.1-μm-diameter particles (Fluoro-Max dyed green aqueous fluorescent particles, Thermo Fisher Scientific Inc., Waltham, MA) at a concentration of 6 ng/ml. These particles have an excitation wavelength of 468 nm and an

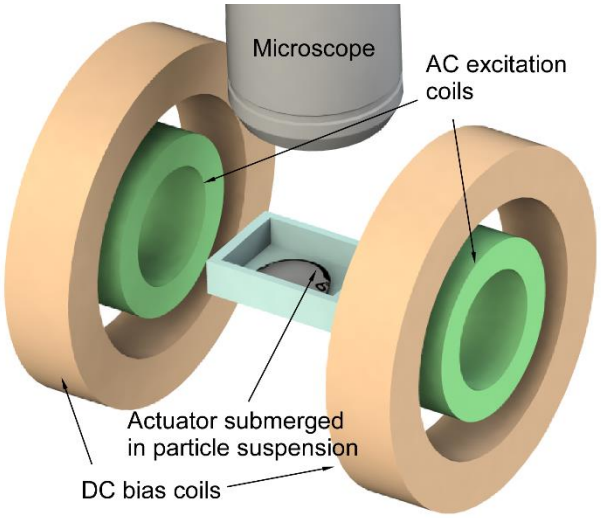


**Fig. 3.8:** Test setup for the particle flow measurements. DC bias coils generated the DC magnetic field for biasing the actuator in the high-magnetostrictivity region. AC excitation coils generated the AC magnetic field to induce actuator vibration.

emission wavelength of 508 nm. The motion of the particles was observed under a microscope (Olympus SZX12 stereo microscope, Olympus Corporation, Tokyo, Japan), and the images were recorded using a digital camera (Pentax K7, Ricoh Company, Ltd., Tokyo, Japan). The particle trajectories were captured in long-exposure (0.6 s) photographs acquired through the microscope. The particle velocities were estimated based on the distances traveled by the particles during the exposure time of the photographs. All measurements were collected at 23°C.

Magnetic biasing was provided by a set of Helmholtz coils that generated a DC magnetic field, and activation was achieved using a second set of coils, coaxial to the first, that transmitted an AC magnetic field (Fig. 3.8). The DC biasing field measured 20 G, whereas the AC excitation magnetic field measured 4 G rms. The frequency of the AC excitation magnetic field varied from 0.1 kHz to 5 kHz. Each annealed actuator was attached to the DMLS-fabricated test plate at its anchor points using cyanoacrylate adhesive. The coils generating the AC excitation magnetic field were located 25-30 mm away from the anchored actuator.

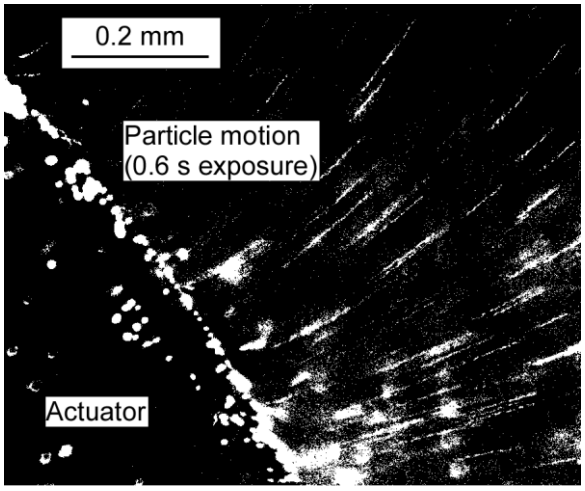


**Fig. 3.9:** Moving fluorescent microparticles observed as streaks in a photograph of a Type *A* actuator resonating at 890 Hz with 0.6 s of exposure. Image thresholding was applied to improve visibility.

Figure 3.9 shows streaks of particle motion generated by a Type *A* actuator, as observed in a long-exposure photograph. At this location, the particles traveled an average distance of 149 μm in 0.6 s. The velocity of the particles was thus estimated to be 248 μm/s. Figure 3.10 shows the particle velocities estimated for each of the actuators using this technique. The regions of the actuators exhibiting particle motion correspond to the antinodes of that particular resonant mode. The mode shapes indicated by the observed antinodes correspond to the simulated mode shapes shown in Fig. 3.3. The Type *A* actuator had six regions where particle flow was generated, with an average flow velocity of 230 μm/s at a resonant frequency of 890 Hz. The flow pattern indicated the third flexural mode of the paddle, confirming the simulated mode shape. Both Type *B* actuators had five regions where particle flow was generated on each paddle. For Type *B1*, an average flow velocity of 200 μm/s was recorded, whereas for Type *B2*, an average flow velocity of 135 μm/s was found. The resonant frequency was 3.8 kHz for Type *B1* and 4.7 kHz for Type *B2*. Type *C* actuator had five regions on each paddle where particle flow was generated, with an average flow velocity of 118 μm/s at a resonant frequency of 520 Hz. The Type *D1* actuator had two regions

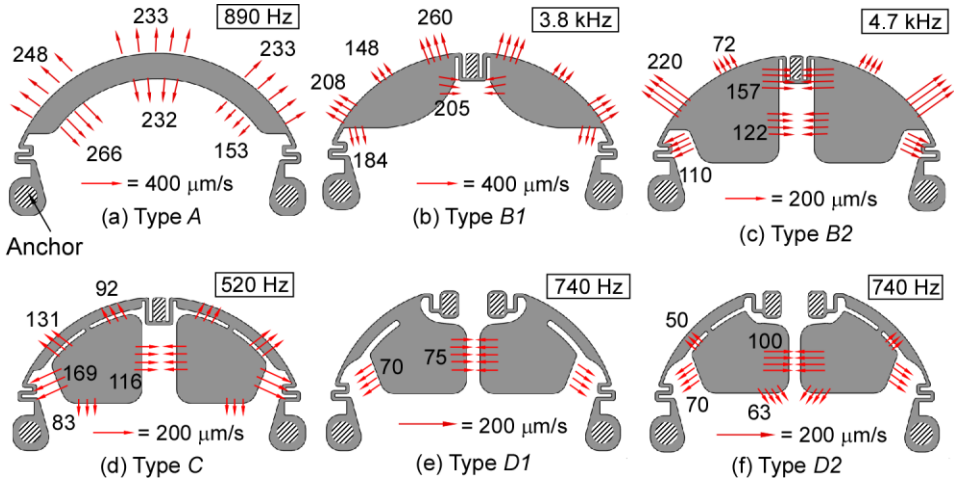


**Fig. 3.10:** Measured resonant frequencies and particle velocities (in μm/s) for the actuators in water.

on each paddle where particle flow was generated, with an average flow velocity of 73 μm/s at a resonant frequency of 740 Hz. Finally, the Type *D2* actuator had four regions on each paddle where particle flow was generated, with an average flow velocity of 70 μm/s at a resonant frequency of 740 Hz.

To estimate the influence of the viscous damping caused by the aqueous environment surrounding the plate body of the AGDD on the vibration amplitudes and the quality factor of the

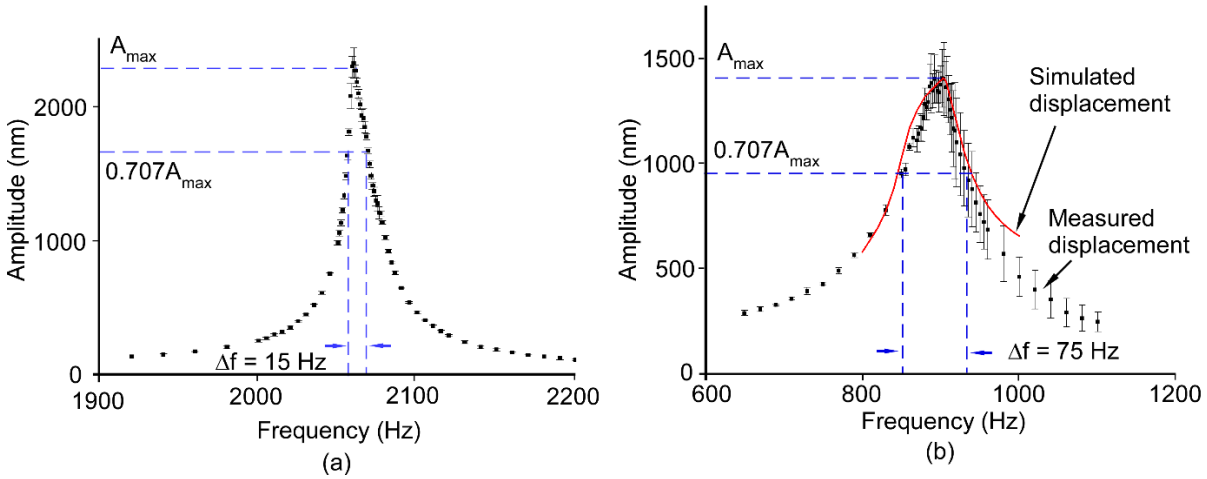


**Fig. 3.11:** Frequency responses measured using a laser displacement meter for the Type *A* actuator in (a) air and (b) water. The plotted amplitudes were measured at the center of the actuator paddle.

resonance, the mechanical frequency response was measured for the Type *A* actuator. A laser displacement sensor (Model LK-G32, Keyence Corporation, Osaka, Japan) was used to measure the vibration amplitudes. The displacement of the center of the Type *A* actuator (in air) as a function of frequency for an AC excitation magnetic field of amplitude 0.2 G is shown in Fig. 3.11(a). The experiment was repeated with the actuator submerged in water (at a depth of less than 1 mm) (Fig. 3.11(b)). The excitation field was increased to 2 G amplitude to generate a measureable response in this high-damping environment. Peak amplitudes of 2.4 μm were observed in air, whereas in water (with a 10-fold increase in the applied magnetic field), the peak amplitude was approximately 1.5 μm.

## 3.5 Discussion

The flexural modes of vibration of the actuators are difficult to detect using magnetic means because the vibrations cause simultaneous tensile and compressive strains. These strains have opposing effects on the generated magnetic field, making detection of resonant peaks using inductive coupling methods difficult. The expected functionality of the actuator is that of prevention of cell adhesion and removal of adhered cells through vibration. The direct observation of these effects of vibration, through particle flow measurements, offers a superior assessment of this functionality. This approach also enables the localization of regions of high vibration amplitudes, which would not be possible using an inductive coupling method.

The particle velocities, on average, were inversely proportional to the area of the actuator. This was anticipated, as a wider paddle transfers more energy to the surrounding liquid. However, a wider paddle also covers a greater portion of the AGDD and is subject to more damping. In future designs, the paddles may be perforated.

A possible concern associated with the use of amorphous magnetic alloys such as Metglas 2826MB for implantable devices is compatibility with magnetic resonance imaging (MRI). The small form factor of the actuators and the low eddy current and hysteresis losses [DeC98] of amorphous magnetic alloys diminish tissue heating. Preliminary calculations show that for a 64-MHz system with a 10-μT oscillating field magnitude (i.e., a B1 field), the tissue heating due to eddy current and hysteresis losses is within the specifications of the IEC 60601-2-33 standard, which establishes the safety limits in an MRI environment [IEC03, Sch15]. Further details of the simulation study to establish the safety of magnetoelastic materials in an MRI environment are described in Appndix D. The small form factor of the actuators also ensures that any artifacts in the MRI image (due to the high permeability of the material) are localized to the immediate vicinity of the actuators.

Despite the fact that the target application of the actuators described in this work is to minimize cell adhesion through vibration, it is quite possible that some accumulation of cells on the actuator surfaces may occur nonetheless. Any change in the resonant frequency due to such tissue loading can be accommodated by using a wideband AC excitation magnetic field rather than a single tone. In addition, previous studies have reported appreciable resonant amplitudes for significant mass loading (in excess of five times the resonator mass) [Gre09a]. Finally, Parylene-C, with which the actuators are coated, exhibits excellent long-term stability and efficacy as a biocompatible material [Sch88]. It does not exhibit any swelling in aqueous environments [Koy14]. As a result, Parylene-C coated magnetoelastic actuators are expected to remain stable *in vivo*.

The simulation model, in conjunction with frequency response measurements, enabled the determination of the energy transfer efficiency between the applied magnetic energy and the induced kinetic energy of the liquid. The quality factors of the Type *A* actuator in air and water

were determined from the frequency response plots shown in Fig. 10. The quality factor $Q$ is approximately equal to $f_0/\Delta f$, where $f_0$ is the resonant frequency and $\Delta f$ is the 3-dB bandwidth. From Fig. 10(a), the quality factor in air is given by:

$$Q_{air} \approx \frac{f_0}{\Delta f} = \frac{2060}{15} = 137 \tag{3.1}$$

Similarly, from Fig. 10(b), the quality factor in water is given by:

$$Q_{water} \approx \frac{f_0}{\Delta f} = \frac{900}{75} = 12 \tag{3.2}$$

The quality factor in water, $Q_{water}$, can be expressed as the following equation of its constituent parts:

$$\frac{1}{Q_{water}} = \frac{1}{Q_{int}} + \frac{1}{Q_{visc}} \tag{3.3}$$

where $Q_{int}$ is the intrinsic loss, including material losses and anchor loss, and $Q_{visc}$ is the loss due to viscous damping in water. Ignoring viscous losses in air (under the assumption that intrinsic losses dominate in air), $Q_{air}$ is approximately equal to $Q_{int}$. Hence, from eqn. (5), $Q_{visc}$ is approximately equal to 13.

The experimentally determined quality factors and frequency response plots were used to model the damping in the custom coupled magnetomechanical simulation implemented in COMSOL Multiphysics 4.4. The frequency response as simulated by COMSOL is shown in Fig. 3.10(b), superimposed on the measured response. The simulated average magnetic energy, $E_{mag}$, delivered to the resonator by the excitation coils is $2.9 \times 10^{-10}$ J. The simulated mechanical energy, $E_{mech}$, of the resonator is $3 \times 10^{-12}$ J. The energy transferred per cycle (through viscous damping) to the liquid, $E_{liquid}$, is $E_{mech}/Q_{visc}$ and is equal to $2.3 \times 10^{-13}$ J. Finally, the conversion efficiency for the energy transferred from the input magnetic field to the liquid is estimated to be $E_{liquid}/E_{mag}$, i.e., 0.08%.

Equation 1.7 indicates that the magnetomechanical coupling coefficient, $k$, which determines the energy conversion efficiency between the mechanical and magnetic domains, is an expression that depends solely on the material parameters. As stated in section 1.2.3, in an amorphous alloy, this property can be tuned by annealing in a magnetic field. This provides an avenue for improving the efficiency of the energy transfer into the liquid.

The results for the Type *A* actuator in water indicate vibration amplitudes exceeding 1 μm. Extrapolating these results to the other designs using the particle velocity measurements, it is safe to assume vibration amplitudes on the order of hundreds of nanometers for all fabricated actuators. Vibration amplitudes and frequencies on the order reported here have previously been shown to reduce cellular adhesion [Ito11, Vla11]. Hence, it can be concluded that the actuators fabricated in this study show vibration amplitudes that are sufficient to impact cell adhesion and proliferation, and can ultimately result in improving the effectiveness of the AGDD in lowering the IOP and preventing vision loss from glaucoma.

Whereas the experimental results reported here for the wireless actuators demonstrate the ability to generate liquid flow, further studies are needed to establish the appropriate usage modality for fibrosis mitigation. Parameters such as amplitude, duration, and periodicity could influence the efficacy of the technique and can only be determined through *in vivo* studies in animal models.

## 3.6 Summary

This chapter describes the design and fabrication of passive, wireless magnetoelastic resonant actuators for microfluidic actuation targeted at mitigating fibrosis in a glaucoma drainage device, as well as the results of *in vitro* experiments with these actuators. By means of three-dimensional scanning, printing, and molding techniques, complex geometries were fabricated

from commercially available amorphous magnetoelastic foils. Particle flow and laser displacement meter measurements were performed to characterize the operation of the actuators in an aqueous environment. Type *A* and *B* actuators exhibited the highest particle flow velocities among the set that was evaluated. Type *B* actuators, with a central anchor for improved surgical compatibility, showed promise as a viable and practical enhancement for the AGDD. Future efforts should be directed at establishing the most suitable usage modality for effective mitigation of fibrosis. This concept can also be extended to other biomedical implants in which microfluidic actuation is required.

# CHAPTER 4

## IMPROVED TECHNIQUES FOR INTERROGATION OF MAGNETOELASTIC RESONATORS

### 4.1 Introduction

The measurement of the resonant behavior of magnetoelastic structures is essential for sensing and tagging applications [Gri11, Tan14, And85]. Magnetoelastic resonant sensors, such as the wireless strain sensors described in Chapter 2, exhibit changes in resonant frequencies in response to changes in the measurand. Resonant frequency and quality factor measurements are also used for material characterization: for instance, to determine the stiffness, magnetomechanical coupling coefficient, or damping [And82, O'De82, Tor78]. Hence, accurate measurement of resonant frequencies is important for technologies based on magnetoelastic materials.

A typical approach for measurement of resonant frequencies uses two inductive coils. The transmit coil is used to excite the magnetoelastic resonant device with an oscillating magnetic field over a range of frequencies. The receive coil is used to detect the magnetic field scattered from the resonant device at the excitation frequency. The resonant response appears as a peak in the

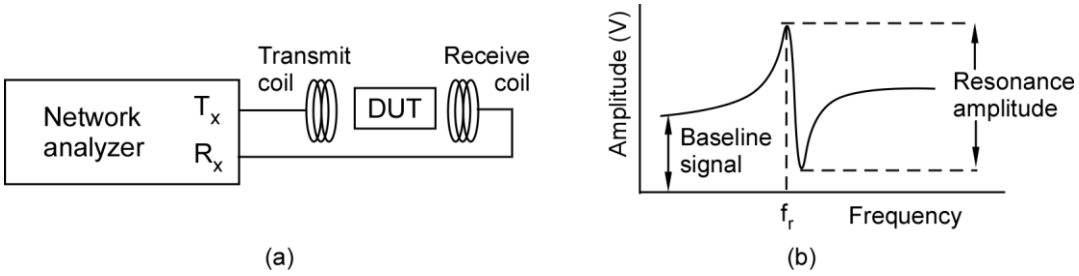


**Fig. 4.1:** (a) Frequency sweep method of detection of magnetoelastic resonances using a network analyzer. (b) Voltage of the receive coil as a function of the frequency.

plot of received voltage vs. frequency at the receive coil (Fig. 4.1). A network analyzer is well-suited for this approach. This was used for characterizing the operation of wireless strain sensors in Chapter 2.

A single inductive coil can also be used for resonant frequency detection [Bar00]. The coil is magnetically coupled to the resonant device. The mechanical vibration of the device results in an increase in the generated magnetic field at the device resonant frequency. This increase in the magnetic field manifests in the form of a peak in the coil inductance at the device resonant frequency.

Improving the detection range of magnetoelastic resonators is a challenging problem. Increased separation between the interrogation coils and the magnetoelastic resonator results in a weaker magnetoelastic response for a given excitation magnetic field. The issue escalates when the resonator is used in a damped environment which inhibits large vibration amplitudes – for instance, as an implant that is in contact with fluids. Boosting the amplitude of the excitation magnetic field will strengthen the resonant response at extended ranges in such conditions. This will also pave the way for resonator miniaturization.

Unfortunately, in any interrogation system, a portion of the excitation magnetic field feeds through directly from the transmit coil to the receive coil. This can possibly overload the receive circuit when high excitation magnetic fields are used. In this context, decoupling of magnetoelastic resonant response from the excitation magnetic field is important for a number of reasons. As was described in Section 1.3.4, expected improvement can be in the form of stronger responses, improved interrogation range, improved noise immunity, and sensor miniaturization.

Decoupling of the excitation magnetic field can be implemented in the time domain, the frequency domain, or through coil design.

**(a) Time domain decoupling:** A sinusoidal magnetic pulse at the resonant frequency is used to excite the resonator, following which the resonator is allowed to ring down freely. The receive coil is deactivated during the pulse transmission, but measured during the ring-down period. In this manner, the excitation magnetic field and the magnetic field of the resonator response are separated in time.

**(b) Frequency domain decoupling:** This method relies on nonlinear response of the resonator to generate a strong harmonic signal. The receive coil is tuned to a frequency band that is a harmonic of the excitation frequency. It rejects the excitation frequency signal. In this manner, the excitation magnetic field and the magnetic field of the resonator response are separated in frequency.

**(c) Decoupling through physical layout of coils:** In methods where transmit and receive coils operate simultaneously in overlapping frequency bands (as shown in Fig. 4.1), decoupling can be achieved through appropriate design of the physical layouts of these coils. In particular, the relative orientations are designed to bring the mutual coupling to zero.

## 4.2 Time domain decoupling

Typically, in time domain detection, an incident magnetic pulse excites the resonant device, following which the ring-down oscillations are measured. Excitation and detection can be performed using separate coils or a single coil switching between transmit and receive circuitry.

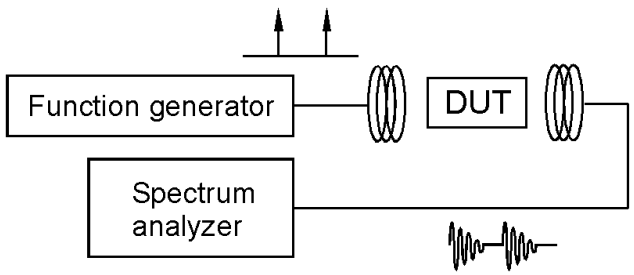


**Fig. 4.2:** Time domain decoupling of resonant response using impulse excitation.

The frequency of the ring-down is the device resonant frequency and can be measured by using Fourier analysis or frequency counting techniques [She10, Zen02] (Fig. 4.2). However, in this approach, the incident magnetic field is distributed over a range of frequencies. Much of the excitation energy is outside the vicinity of device resonant frequency and has a lower contribution towards building the vibration amplitudes prior to initiation of the ring-down. This does not maximize the response for the available stimulation power.

A time domain ring-down approach where the excitation magnetic field is a sinusoid of limited duration, at a frequency equal to the resonant frequency of the device, can generate a higher amplitude ring-down response. The temporal separation avoids interference of excitation magnetic field with the resonator response. However, for sensing devices where the device resonant frequency is subject to change, the excitation frequency would very likely be different from the device resonant frequency. In addition, small fluctuations in biasing DC magnetic fields and batch-to-batch variations between devices lead to a non-uniformity in resonant frequencies across seemingly identical devices. In this scenario, the excitation frequency must be adjusted to track the device resonant frequency for strongest response.

A method of using the ring-down response of an LC resonant sensor to track the resonator frequency using a phase-locked loop (PLL) has been reported previously [Joy07]. In applications where phase synchronization is not necessary, a frequency-locked loop (FLL) can be used to track a frequency of interest, which in the case of a magnetoelastic sensor is its resonant frequency. Analog and digital FLLs find wide use in wireless communication systems for carrier synchronization and frequency synthesis [Cur12, Hua11, Kha11]. FLLs have also been demonstrated for frequency measurement applications [Dea13, Luo11]. By ignoring the relative phases between the target signal and the generated response signal, an FLL typically allows a

larger lock-in range than a PLL [Cur12]. This is a desired feature because the effective elastic stiffness (and correspondingly, resonant frequencies) of magnetoelastic materials are highly dependent on the magnitude of biasing magnetic field, with variations of up to 90% of the nominal values in some situations [Tor78, Ber76, Boz93]. However, for the resonators described in this thesis, the variations in resonant frequency are only in the range of 3-5%.

The remainder of this section (§4.1) describes the use of an FLL is used to characterize the operation of magnetoelastic strain sensors of the type described in Chapter 2. Real-time tracking of strain, as made possible by the FLL, is useful in applications that present fast changing loading conditions. For instance, real-time strain measurements in a biomechanical implant can be used to monitor its operation under stresses resulting from bodily motion. Such strain sensors can be integrated with artificial joints or orthopedic implants [Bur00].

### 4.2.1 Theory and Modeling

*A. The frequency-locked loop*

The system level diagram for the approach used in this section is shown in Fig. 4.3. An excitation pulse of predetermined duration and frequency builds up the vibration of the magnetoelastic sensor, following which the excitation is turned off. The sensor is then allowed to

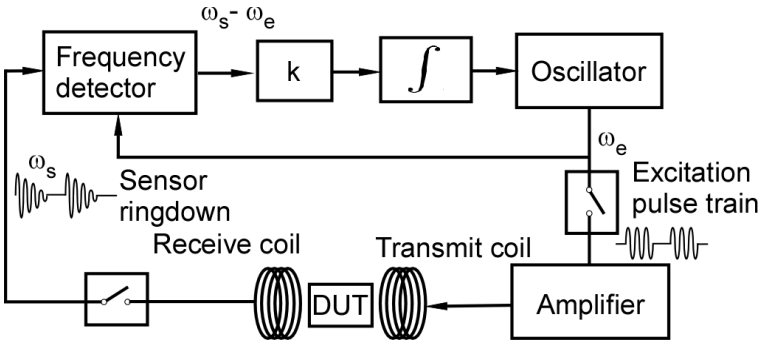


**Fig. 4.3:** Detection of resonant frequency of magnetoelastic resonator using a frequency locked-loop.

ring-down at its resonant frequency. A single iteration of the FLL detects the sensor ring-down response, compares it with the excitation frequency, and updates the excitation frequency for the next pulse, bringing it closer to the sensor resonant frequency. Sufficient number of loop iterations result in the excitation frequency locking on to the sensor resonant frequency. After lock-in, the FLL tracks the sensor resonant frequency, following any variations in it. At this point, the sensor read-out is simply the frequency of the excitation pulse. An amplifier is used to generate the currents needed to drive the transmit coil. In addition, switches are used to gate the transmit pulses to the driving amplifier and the received signal from the sensor to the frequency detector.

Figure 4.4 shows an illustration of the excitation pulses to the transmit coil and the sensor response at the receive coil. The sensor response is gated by a switch to isolate the ring-down response (Fig. 4.4(c)). The FLL analyzes this ring-down response.

The frequency detector compares the excitation frequency with the resonant ring-down frequency and presents the difference between the two (Fig. 4.5). To perform this operation, the

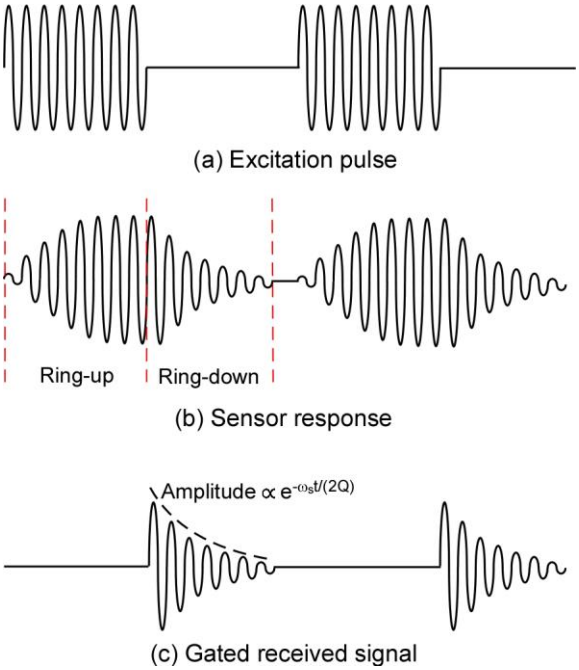


**Fig. 4.4:** (a) Sinusoidal excitation pulse applied to the sensor by the transmit coil. (b) Sensor response. (c) Received resonator signal after gating.

measured ring-down signal from the receive coils is multiplied with two sinusoids at the excitation frequency that are in a quadrature phase relation with one another. If $V_{sig}$ is the resonant ring-down response of the magnetoelastic sensor at frequency $\omega_s$ (as detected at the receive coil), and $V_{ex}$ is the excitation signal at frequency $\omega_e$ (from the oscillator output):

$$V_{sig} = V_s(t)\sin(\omega_s t) \tag{4.1}$$

$$V_{ex} = V_e \sin(\omega_e t); \tag{4.2}$$

Then the mixer outputs, after low pass filtering are:

$$X = 0.5\, V_s(t)\, V_e \cos\{(\omega_s - \omega_e)\, t\} \tag{4.3}$$

$$Y = 0.5\, V_s(t)\, V_e \sin\{(\omega_s - \omega_e)\, t\} \tag{4.4}$$

The phase difference, $\Delta\theta(t)$, between the excitation signal and the sensor resonant response is $\tan^{-1}(Y/X)$. Figure 4.6 illustrates the phase difference signal for $\omega_s > \omega_e$ and $\omega_s < \omega_e$. The frequency separation, $\omega_s - \omega_e$, between the excitation and the ring-down frequency is the slope of the phase difference. If the phase difference is calculated at intervals of $\Delta t$, then frequency separation is given as:

$$\omega_s - \omega_e = \Delta\omega = \frac{\Delta\theta}{\Delta t} = \frac{\theta(t+\Delta t) - \theta(t)}{\Delta t} \tag{4.5}$$

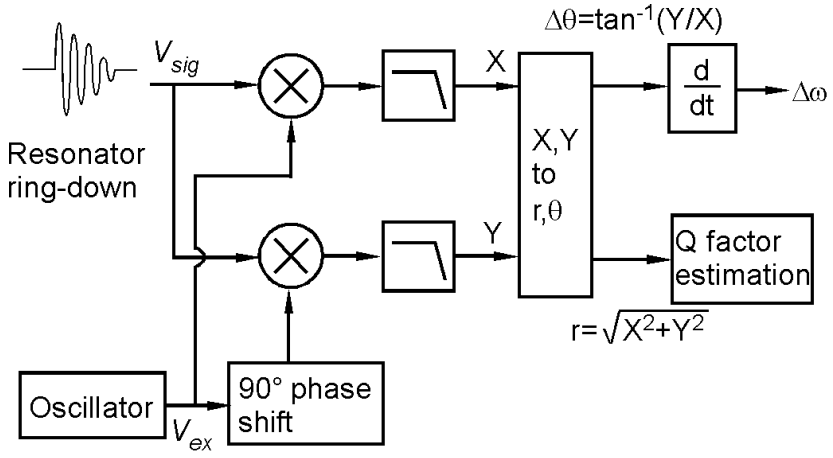


**Fig. 4.5:** Architecture of the frequency detector. The resonator ring-down signal amplitude can also be detected in this step which can be used to estimate the resonance quality factor.

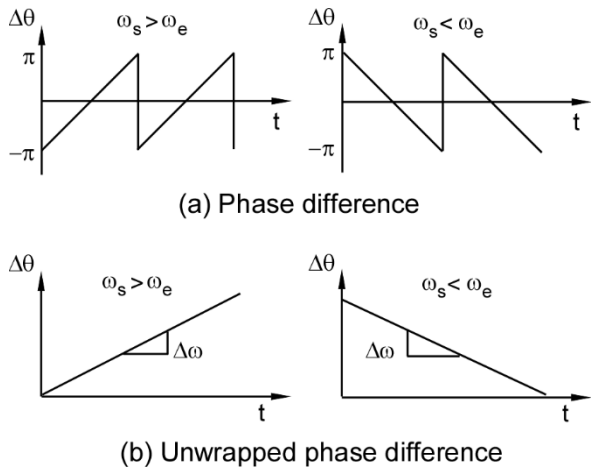


**Fig. 4.6:** (a) Phase difference (Δθ) for the two cases where the sensor resonant frequency is greater than and less than the excitation frequency. (b) The frequency difference between the sensor resonant frequency and the excitation frequency is the slope of the unwrapped phase difference.

An average of $\omega_s - \omega_e$ is measured for the duration of the ring-down and is the output of the frequency detector.

The error signal (i.e., $\omega_s - \omega_e$) multiplied by a predetermined constant, $k$, is used to adjust the frequency of the oscillator for the next excitation pulse, bringing it closer to the sensor resonant frequency. The process is continuously repeated, ensuring the frequency separation between the excitation and the resonant frequency tends to zero.

The duration of excitation pulse required for maximum ring-down response depends on the damping of the sensor. A sensor that is subject to higher damping will take longer to reach its peak vibration amplitude. For instance, Fig. 4.7 shows the MATLAB-simulated ring-up transient response amplitude of a resonator subject to an excitation magnetic field at a frequency equal to its resonant frequency. The sensor resonant frequency is assumed to be 50 kHz with a resonance quality factor of 200. Hence, for this resonator, it is expected that an excitation pulse of a duration

of 10 ms would ensure that the resonator attains peak vibration amplitudes before the ring-down is initiated. This would result in the maximum amplitude for the ring-down signal.

The ring-down response can also be used to determine the mechanical quality factor of the resonant response. Assuming that a simple spring-mass-damper model can be applied, the amplitude of the ring-down, $V_s(t)$ (or $0.5\,V_s(t)\,V_e$ after downconversion) is proportional to $e^{-\frac{\omega_s}{2Q}t}$. The amplitude after the downconversion step can be evaluated from $X$ and $Y$ and is equal to $\sqrt{X^2+Y^2}$ (Fig. 4.5). The quality factor of the resonance is determined by an exponential curve-fit to this amplitude, once the FLL is locked into the resonant frequency.

*B. Loop dynamics*

Each ring-down of the resonator (corresponding to one loop iteration) will provide a single data point, or "sample", of the difference between the excitation and the ring-down resonant frequency. This difference is used to correct the excitation frequency for the next loop iteration. The sampling rate of the FLL is the loop iteration rate which can be measured in samples/s. Assuming that a proportional controller is used, the corrected excitation frequency is the sum of

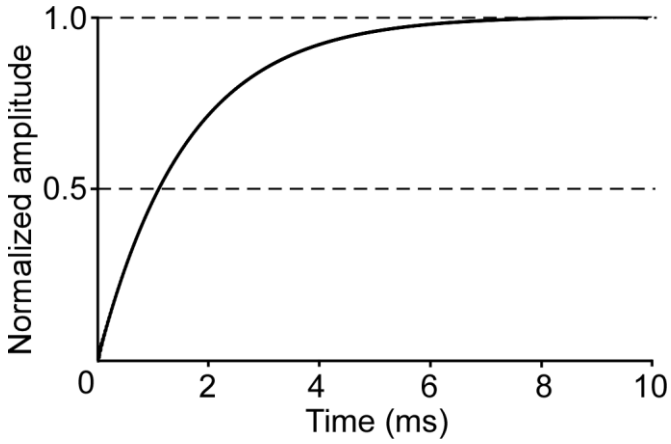


**Fig. 4.7:** MATLAB-simulated amplitude of ring-up response for a 50 kHz resonator with a quality factor of 200.

the previous excitation frequency and the error signal (multiplied by gain $k$). Hence, the excitation frequency at the $n^{th}$ iteration of the loop, $\omega_e(n)$, can be described by the difference equation:

$$\omega_e(n) = \omega_e(n-1) + k[\omega_s(n-1) - \omega_e(n-1)]$$

$$\therefore\ \omega_e(n) - (1-k)\omega_e(n-1) = k\omega_s(n-1) \tag{4.6}$$

where $\omega_s(n)$ is the sensor resonant frequency. The system transfer function is then given by:

$$S(z) = \frac{\Omega_e(z)}{\Omega_s(z)} = \frac{kz^{-1}}{1-z^{-1}+kz^{-1}} \tag{4.7}$$

where $\Omega_e(z)$ and $\Omega_s(z)$ are the $z$-transforms of $\omega_e(n)$ and $\omega_s(n)$, respectively. However, the excitation frequency generator will take a finite amount of time to respond to the error signal and change its frequency. The signal flow path must account for this. If the frequency generator can be represented by a transfer function $H(z)$, the system transfer function is given by:

$$R(z) = \frac{kH(z)z^{-1}}{1-z^{-1}+kH(z)z^{-1}} \tag{4.8}$$

The signal flow block diagram in the $z$ domain is shown in Fig. 4.8. From equation (8), and a given transfer function $H(z)$, the values of $k$ that result in a stable feedback loop can be determined. For instance, assuming a single-pole transfer function for the oscillator:

$$H(z) = \frac{z^{-1}(1-a)}{(1-az^{-1})} \tag{4.9}$$

where $a$ is defined by the unit step response which is given to be $1-a^n, |a|<1, n \geq 0$, we get:

$$R(z) = \frac{k(1-a)z^{-2}}{1-(a+1)z^{-1}+[a+k(1-a)]z^{-2}} \tag{4.10}$$

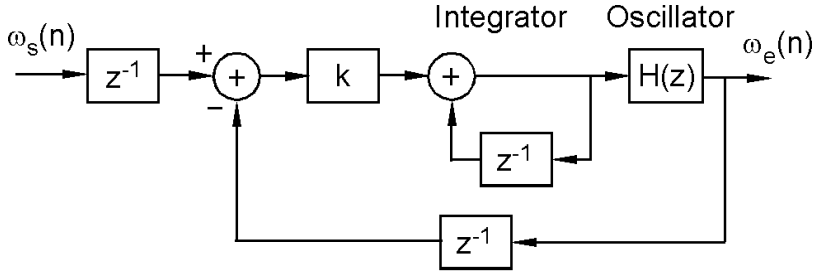


**Fig. 4.8:** The $z$-domain model of the frequency-locked loop.

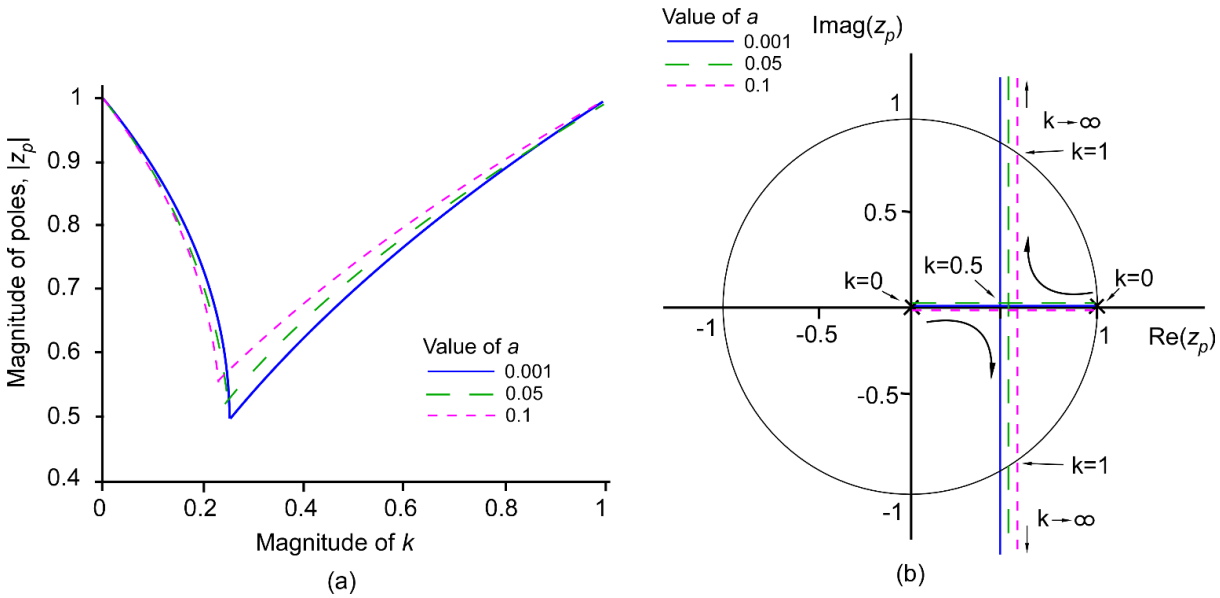


**Fig. 4.9:** (a) Magnitude of poles of transfer function $R(z)$ for different values of $k$ and $a$. (b) Root locus plot showing the poles of the transfer function $R(z)$ as $k$ varies. The system is stable if the poles lie within the unit circle.

The parameter $a$ defines the transient response of the oscillator: a smaller value of $a$ indicates a faster response.

The value of $k$ for a desirable system response can also be established from the system transfer function. By the condition for stability, the magnitude of the poles should be less than 1. Figure 4.9 shows the MATLAB-calculated poles of $R(z)$, defined by equation 4.10, as a function of $k$ and three values of $a$. Figure 4.9(a) shows the magnitude of the poles, whereas Fig. 4.9(b) shows the root locus of the transfer function. It is clear that for a stable system (with magnitude of poles being less than 1), $k$ should be less than 1. Exceeding this value for $k$ results in the magnitude of poles being greater than 1, causing instability of the feedback loop. Note that the magnitude of the poles is relatively insensitive to the value of $a$.

Figure 4.10 (a) shows the system response for a unit step input and the frequency response for four different values of $k$ with $a$ = 0.001. The frequency is normalized by division with the

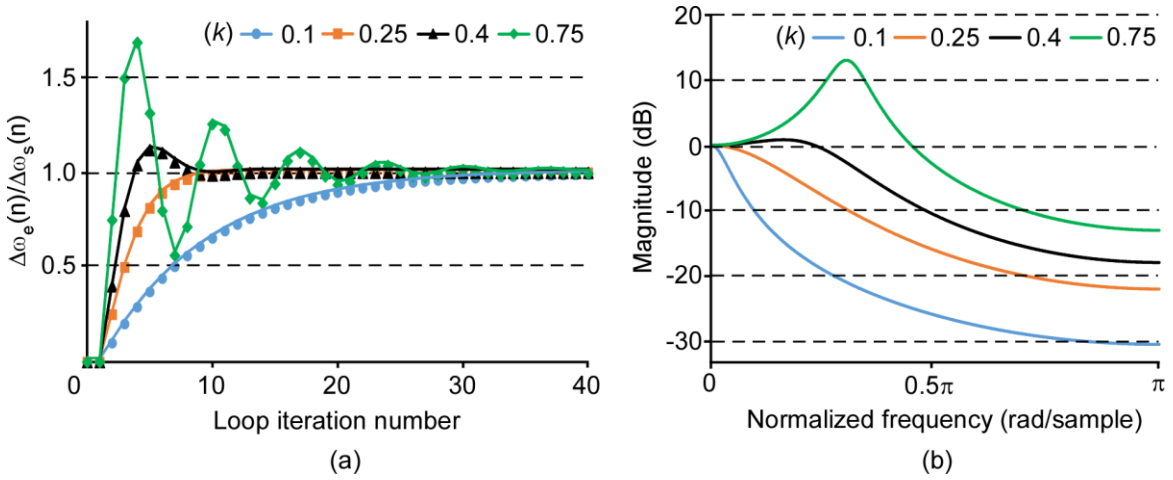


**Fig. 4.10:** (a) FLL response to a step change in frequency for different values of *k*. (b) Frequency response of the FLL for different values of *k*.

sampling rate of the FLL. A low value of *k* leads to the response being excessively damped resulting in a sluggish FLL response. In contrast, a high *k* leads to an underdamped response with a large overshoot. A *k* of 0.25 generates critically damped transient response without overshoot. However, a slightly underdamped system is desirable for higher measurement bandwidth (Fig. 4.10(b)). A *k* of 0.4 corresponds to a wider measurement bandwidth than a *k* of 0.25. A wider measurement bandwidth enables the measurement of oscillating resonator signals at higher frequencies. For a strain sensor, this means the FLL can track loads oscillating at higher frequencies. The 3 dB-bandwidth for a *k* of 0.25 is 0.15$\pi$ rad/sample while for a *k* of 0.4 it increases to 0.32$\pi$ rad/sample.

### 4.2.2 Design and Fabrication

*A. Prototype strain sensors*

The magnetoelastic resonant strain sensors used for testing the FLL follow the architecture of the sensors described in Chapter 2. The sensors are suspended by attachment at the anchor points. Applied strain causes a change in the stiffness of the resonant strip through the $\Delta E$ effect,

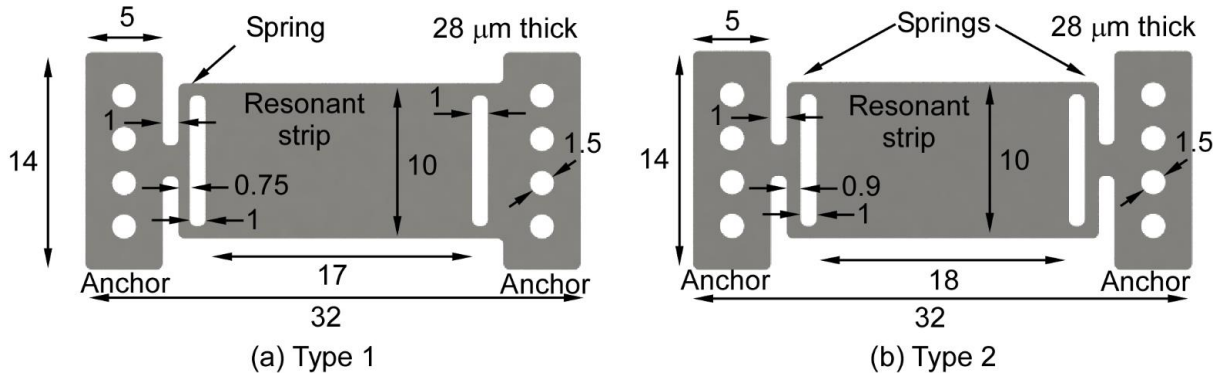


**Fig. 4.11:** Dimensions of the two prototype sensor designs (in mm).

resulting in a change in the sensor resonant frequency. Springs limit the strain in the resonant strip, effectively increasing the dynamic range of the sensor. The sensors are fabricated from the Metglas 2826MB alloy.

The two sensor designs used for this test are shown in Fig. 4.11. Both the sensors measure $32 \times 14$ mm$^2$, and are 28 μm thick. Also, both the sensors are designed for a dynamic range of 2 mstrain. The Type 1 sensor has the strain limiting spring attached to one anchor. Narrow attachments to the second anchor limit the energy losses to the anchor by inducing an acoustic mismatch [Gra75]. The Type 2 sensor has springs attached to both the anchors to generate a symmetric mode shape, in addition to inducing an acoustic mismatch at both anchor locations.

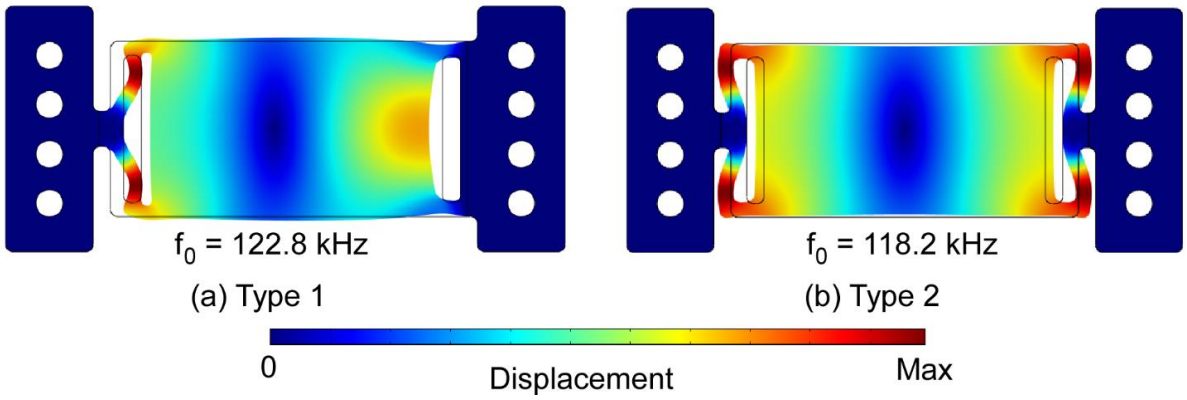


**Fig. 4.12:** COMSOL-simulated resonant frequencies and mode shapes for (a) Design 1, and (b) Design 2 strain sensors.

As with the previously described strain sensor designs, the longitudinal modes provides the strongest signal response. The COMSOL-simulated resonant frequency for the Type 1 sensor is 122.8 kHz, while that for the Type 2 sensor is 118.2 kHz. The target resonant mode shapes as simulated in COMSOL are shown in Fig. 4.12.

The magnetic biasing field for sensor operation is generated by Arnokrome 3 permanent magnets (Arnold Magnetic Technologies Corp., Rochester, NY). The appropriate sizing and spacing between the permanent magnets and the strain sensor for desired operation is estimated through magnetic field simulations in COMSOL Multiphysics. Further details of these simulations are described in Appendix B. Based on these simulation studies, a 100-μm-thick magnet measuring 21 × 4 $mm^2$, placed at a distance of 2 mm from the sensors, is estimated to be capable of providing sufficient bias field for both sensor designs.

The sensors are fabricated using photochemical machining (PCM) at an external facility (Kemac Technology, Inc., Azusa, CA). The fabricated sensors are shown in Fig. 4.13. The permanent magnets are fabricated using micro-electrodischarge machining (μEDM).

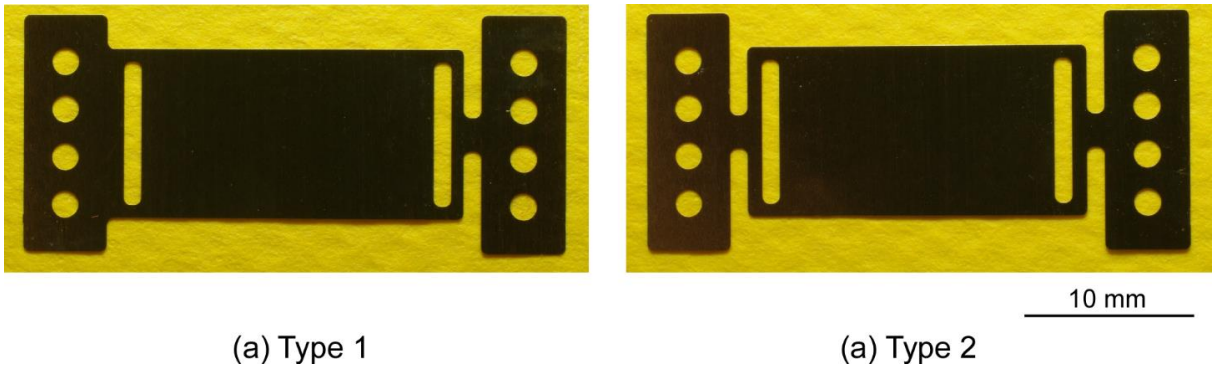


**Fig. 4.13:** Strain sensors fabricated using PCM.

*B. Test setup*

The test setup consists of a polypropylene cantilever, on the surface of which the strain sensors are affixed. A prescribed displacement of the cantilever tip would result in a determinable

magnitude of strain on the cantilever surface. This strain-displacement relationship is established using a commercial strain gage (SGD-5/350-LY13, Omega Engineering, Inc., Stamford, CT). The sensors are suspended on two supports (600-μm-thick silicon blocks). The Arnokrome 3 permanent magnets are affixed underneath the cantilever. Cyanoacrylate adhesive is used for all attachments.

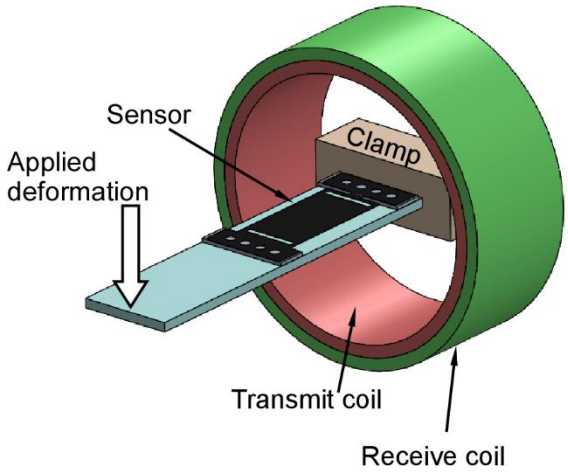


**Fig. 4.14:** Test setup for sensor interrogation. The biasing magnet is affixed underneath the cantilever and is not visible in this image.

The transmit coil that generates the excitation magnetic field is 30 mm in diameter, 10 mm in length, and has 10 turns. The receive coil that detects the sensor response is wound coaxial to the transmit coil, is 10 mm in length, and has 10 turns. The complete test setup is shown in Fig. 4.14.

*C. FLL system implementation*

The FLL is software-defined, and is implemented in a custom program written in the National Instruments LabVIEW software with signal generation and acquisition through the NI USB-6341 device (National Instruments Inc., Austin, TX). The USB-6341 generates the sinusoidal excitation signal which is then amplified (amplifier Model 7500, Krohn-Hite Corp.,

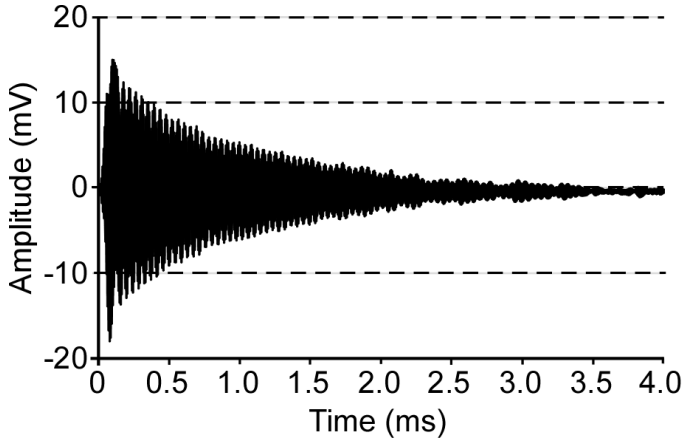


**Fig. 4.15:** Ring-down response for the unstrained Type 1 strain sensor, measured as the voltage at the receive coil.

Brockton, MA). An analog switch (TS5A22364, Texas Instruments Inc., Dallas, TX) gates the excitation energy to the transmit coil and the received ring-down sensor response detected by the receive coil. The switch is controlled by signals that are also generated by the USB-6341 device.

### 4.2.3 Results

The sensors are excited by the excitation magnetic field for a duration of 10 ms, following which the ring-down is measured. The exemplary ring-down response of the Type 1 strain sensor,

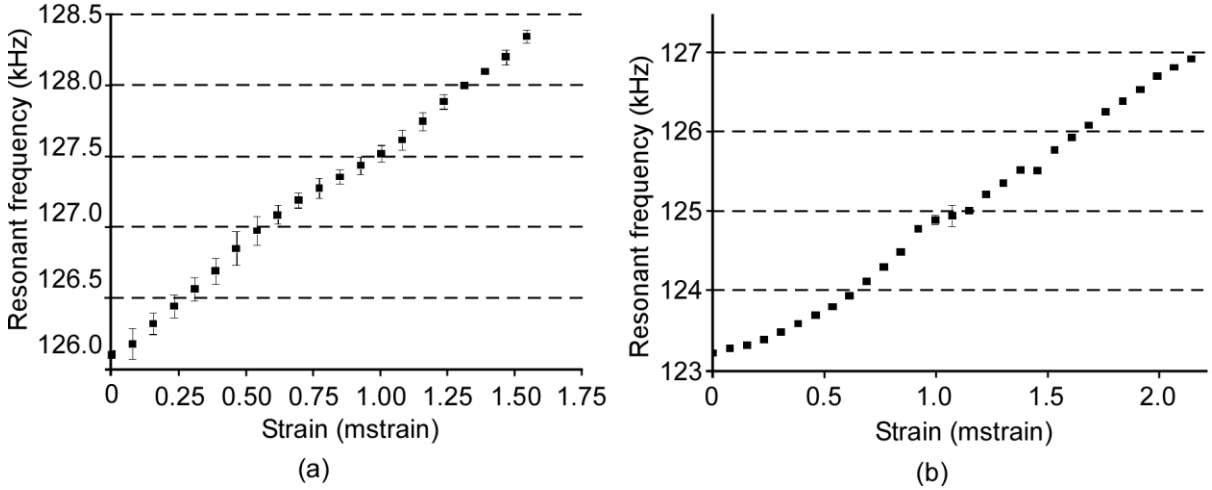


**Fig. 4.16:** Resonant frequency as a function of applied tensile strain for the (a) Type 1 strain sensor, and the (b) Type 2 strain sensor.

as picked up by the receive coils, is shown in Fig. 4.15. The ring-down is apparent for a duration of approximately 4 ms. Similar response was observed, albeit at a different frequency, for the Type 2 sensors. Each loop iteration of the FLL takes an estimated 50 ms to complete. The excitation signal generation and the measurement of the ring-down takes approximately 25 ms, while the rest of the time is taken by the LabVIEW program to analyze the data.

The strain dependencies of resonant frequencies for the two sensor types are shown in Fig. 4.16. The Type 1 sensor has an unstrained resonant frequency of 126.1 kHz. Under applied tensile strain of 1.5 mstrain, the resonant frequency increases to 128.3 kHz. Correspondingly, the sensitivity of the Type 1 sensor is 11600 ppm/mstrain. The Type 2 sensor has an unstrained resonant frequency of 123.2 kHz. Under applied tensile strain of 2.1 mstrain, the resonant frequency increases to 126.9 kHz. Correspondingly, the sensitivity of the Type 2 sensor is 14300 ppm/mstrain.

The quality factor estimates for the two sensors, based on curve-fitting an exponential decay to the ring-down response amplitude, are shown in Fig. 4.17. The quality factor for the Type 1 sensor is 380, while for the Type 2 sensor, it is 300. These measurements are under no-strain

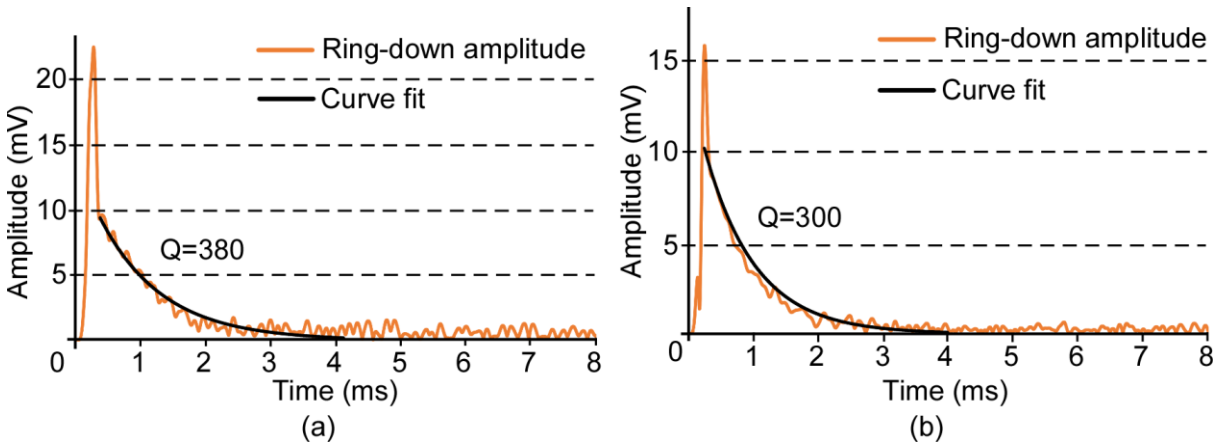


**Fig. 4.17:** Quality factor estimation by curve-fit for the (a) Type 1 sensor, and (b) Type 2 sensor. The measurements are under no-strain conditions. The initial peak observed in the ring-down is because of the switching transients.

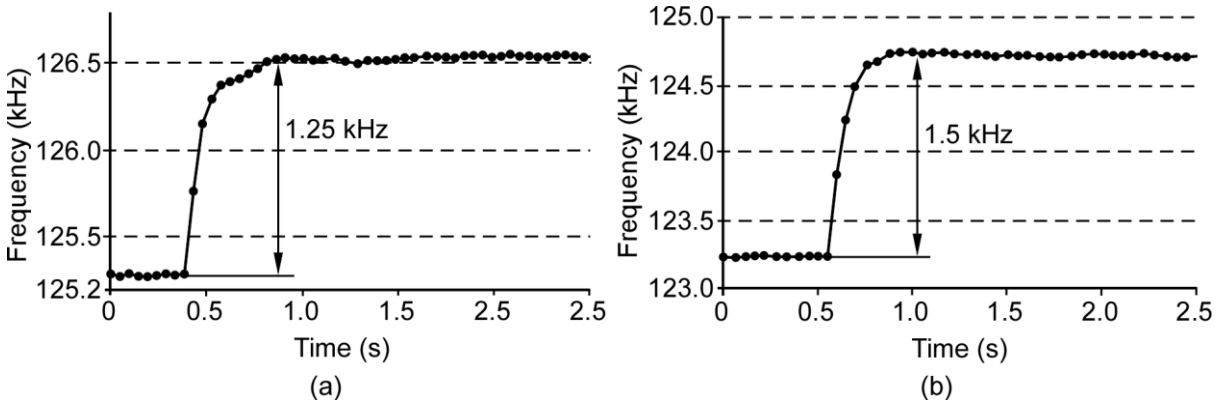


**Fig. 4.18:** Response of the FLL to an applied step of 0.8 mstrain for the (a) Type 1 sensor, and (b) Type 2 sensor.

conditions. The observed resonant frequencies and quality factors indicate that the duration of the excitation signal need only be 4 ms to achieve maximum vibration amplitude before ring-down.

The step response of the measurement system is also determined (Fig. 4.18). An electromechanical solenoid actuator (SMT1632S, Jameco Electronics, Belmont, CA) is used to apply a step displacement to the cantilever surface. The response time for the actuator is approximately 10 ms. An applied step of 0.8 mstrain results in a frequency shift of 1.25 kHz for the Type 1 sensor, and 1.5 kHz for the Type 2 sensor. The FLL achieves a lock to the new frequency within 10 loop iterations, as is expected based on the response plotted in Fig 4.10(a).

### 4.2.4 Discussion

Variations in the frequency of the FLL, as represented by the error bars in Fig. 4.15, indicate the presence of noise in the system. A major source of noise in the FLL response is the mode splitting in the resonant response of the sensor due to the out-of-plane deformation of the sensor under applied strain. The sensor is fabricated from Metglas 2826MB foils that are available in the form of rolls. As a result, the fabricated sensors have some initial out-of-plane curvatures. Under applied strains, this causes significant out-of-plane deformations. Figure 4.19 shows the

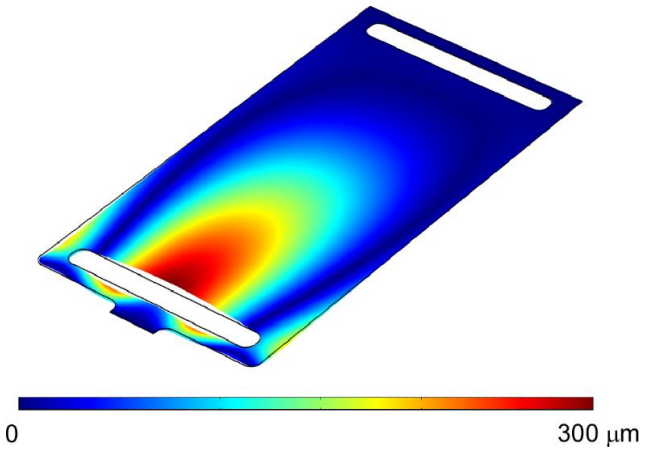


**Fig. 4.19:** Simulated out-of-plane deformation of the Type 1 sensor under an applied tensile strain of 2 mstrain. Anchors are not defined to reduce simulation complexity.

COMSOL-simulated out-of-plane deformation for an applied tensile strain of 2 mstrain. An initial curvature is assumed such that the sensor mid-point is displaced 100 μm out-of-plane with respect to the anchors. Such strain-induced deformations generate spurious modes that are spaced close to the frequency of the target sensor resonant modes. In such cases, the ring-down response is not an ideal exponentially decaying sinusoid. The resultant error term $(\omega_s - \omega_e)$ has significant variation from iteration to iteration, resulting in the noise in the frequency lock. In addition, this can also limit the sensor dynamic range if increasing strain-induced deformation results in the

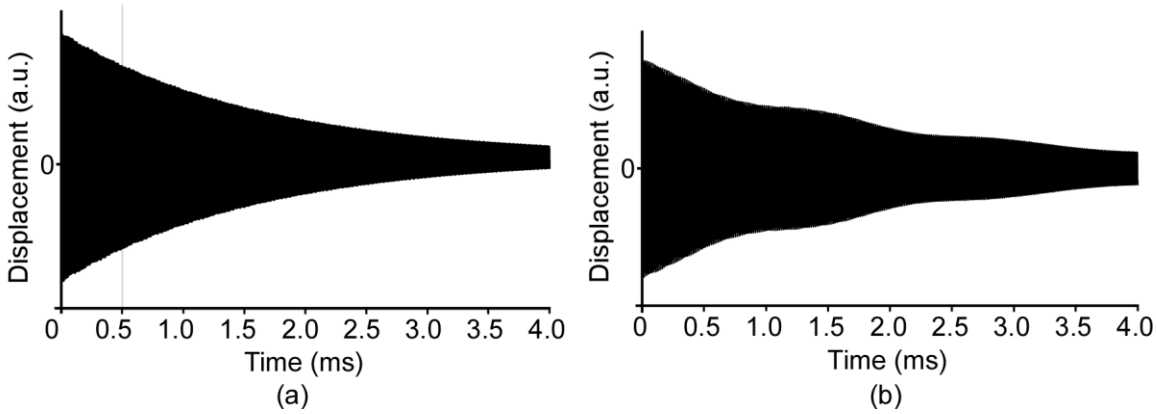


**Fig. 4.20:** COMSOL-simulated ring-down displacement amplitudes (in arbitrary units) of a point at the end of the resonant strip of a Type 1 actuator in (a) non-deformed state, and (b) deformed state as characterized by Fig. 4.18.

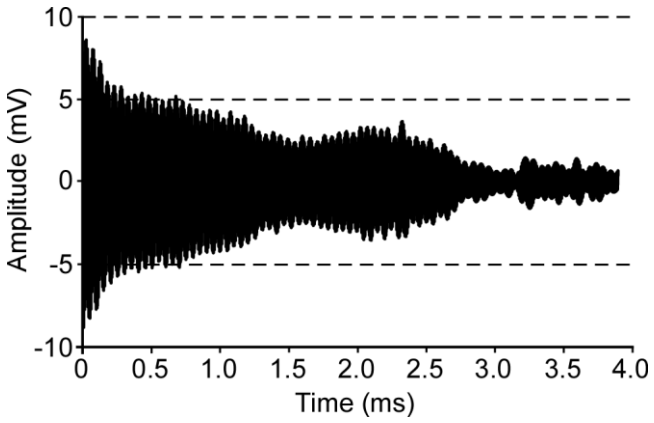


**Fig. 4.21:** Ring-down response for the Type 1 strain sensor, under applied tensile strain of 0.8 mstrain, measured as the voltage at the receive coil.

amplitude of the spurious modes becoming comparable to the target resonant modes. In such a case, the FLL can lose its lock of the target mode, and instead lock onto the spurious mode.

COMSOL can be used to simulate the ring-down response of the sensors, both in non-deformed and deformed states. Figure 4.20 compares the simulated ring-down response for the non-deformed Type 1 sensor under no applied strain to the ring-down response for the deformed sensor (as shown in Fig. 4.19). Arbitrary units are used because the amplitude is highly dependent on the initial conditions as well as the experimental settings. Experimental ring-down receive coil voltage readings, shown in Fig. 4.21 for a strained Type 1 sensor, shows response similar to that predicted by simulation. Such a response is in contrast to a more ideal ring-down response shown in Fig. 4.15. Optimization of the anchoring mechanisms can reduce the sensor out-of-plane sensor deformation, improving the system performance.

## 4.3 Frequency domain decoupling

### 4.3.1 Introduction

Non-linearities in magnetostrictive and mechanical properties of amorphous magnetoelastic materials (like Metglas 2826MB) result in magnetization and mechanical vibrations at harmonics of the excitation magnetic field. This harmonic response can be exploited

to decouple the excitation magnetic energies from the sensor response. The received signal from the material is measured only at harmonics of the excitation frequency, effectively isolating the excitation energies from the receive circuits. This can lead to improved system performance in the form of increased detection range and larger signal-to-noise ratios.

Previous work on the use of harmonic measurement technique involved the measurement of generated field magnitudes at harmonics of the excitation frequency [Tan12, Ong02]. The excitation in the previous work is non-resonant in nature and the generated field magnitudes correlate to the magnitude of the measurand. However, the generated field magnitudes are also dependent on interrogation distance which requires careful calibration to get usable data.

Magnetoelastic resonant sensors, like the strain sensors described in Chapter 2, work by transducing the measurand into a change in its resonant frequency. In this section, a harmonic resonant excitation approach is proposed for frequency domain decoupling of excitation energy and resonant response.

*A. Non-linear behavior of magnetoelastic materials*

Non-linearity in magnetoelastic materials is the cumulative result of its magnetostrictive, elastic and magnetization properties. Magnetostriction is a non-linear phenomenon. For materials showing a two-fold in-plane anisotropy (i.e. uniaxial anisotropy), which as-quenched amorphous metals are known to possess [Fuj83], magnetostriction $\Delta l/l$ can be related to applied magnetic field, $H$, as:

$$\frac{\Delta l}{l} = \frac{3}{2}\lambda_s \left(\frac{H^2}{H_A^2} - \frac{1}{3}\right) \tag{4.11}$$

where $H_A$ is the anisotropy field and $\lambda_s$ is the spontaneous magnetostrictive strain in a domain in the direction of applied field [Liv82]. In addition, magnetostrictive behavior exhibits saturation and hysteresis, which also contribute to non-linearity [Kim99].

Secondly, the mechanical stress-strain characteristic of magnetoelastic materials is non-linear. Under applied stress, the resultant strain in these materials is the sum of strain due to material elasticity and strain due to the rotation of magnetic domains [Cul09a]. This is due to strong spin-orbital coupling, wherein rotation of electron spins results in rotation of electron clouds, and vice-versa. This behavior manifests as a non-linear stress-strain characteristic.

Finally, the magnetization behavior of amorphous magnetoelastic materials is non-linear. As with all ferromagnetic materials, they exhibit hysteretic magnetization curves and saturation of magnetization at elevated magnetic fields [Met00]. The cumulative effect of these non-linear effects results in an oscillatory response at harmonics of excitation frequencies.

*B. Zero bias operation*

In a typical magnetoelastic resonant device, a DC magnetic field is applied to bias the resonator at a point in the magnetostriction curve where the small-signal magnetostrictivity (i.e., the slope of the curve) is high. A small amplitude sinusoidal excitation field, superimposed on this DC biasing field, results in a sinusoidal mechanical and magnetization response proportional to the small-signal magnetostrictivity. If the magnetostriction characteristic is linear, the response is solely at the frequency of the excitation field. In absence of the DC biasing field, the resonator would be biased at essentially zero small-signal magnetostrictivity, resulting in no response at the excitation frequency.

The non-linearity of magnetostriction is a contributing factor in generation of a response at harmonics of the excitation frequency. This non-linearity is present even in absence of a DC biasing field. Figure 4.22 shows the magnetostriction curve of Metglas 2826MB, with polynomial approximations at different regions. The strain at zero bias field is proportional to 0.033 times the square of the applied field, while at about 9 G bias field, it is 0.032 times the square of the applied

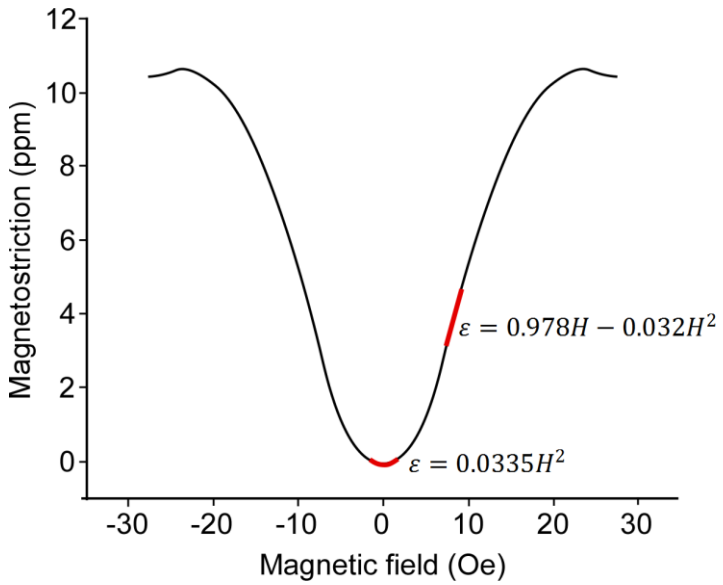


**Fig. 4.22:** Polynomial approximations at different regions of the magnetostriction curve. The magnetostrictivity characteristic is derived from [Gut13].

field. The square term is responsible for the generation of the harmonic response to an applied sinusoidal excitation. Based on this, the harmonic response at zero bias field should be comparable to the response in presence of a bias field.

The methods outlined in this section measure the response of a given excitation frequency at the harmonic of the excitation frequency. This can be exploited in two ways – exciting at half the resonant frequency and observing the response at the resonance frequency ($0.5f_0$ excitation), and exciting the resonant frequency and observing the response at twice the resonant frequency ($f_0$ excitation).

### 4.3.2 Design

Two techniques for excitation and detection of harmonic frequencies are implemented – modified gain-phase analyzer method, and PC-controlled data acquisition and analysis.

*A. Modified gain-phase analyzer*

In this technique, a network analyzer (Agilent 4395A, Agilent Technologies, Santa Clara, CA) is operated in the gain-phase analyzer mode. A frequency divider is used to divide the frequency of the signal, *f*, from the transmit terminal of the network analyzer (labeled $T_x$ in Fig. 4.23(a)) by two. Therefore, the excitation magnetic energy is at half the frequency (0.5*f*) of the signal from the $T_x$ terminal. The receive terminal (labeled $R_x$ in Fig. 4.20) scans at frequency *f*. In this manner, the system measures the response at twice the excitation frequency.

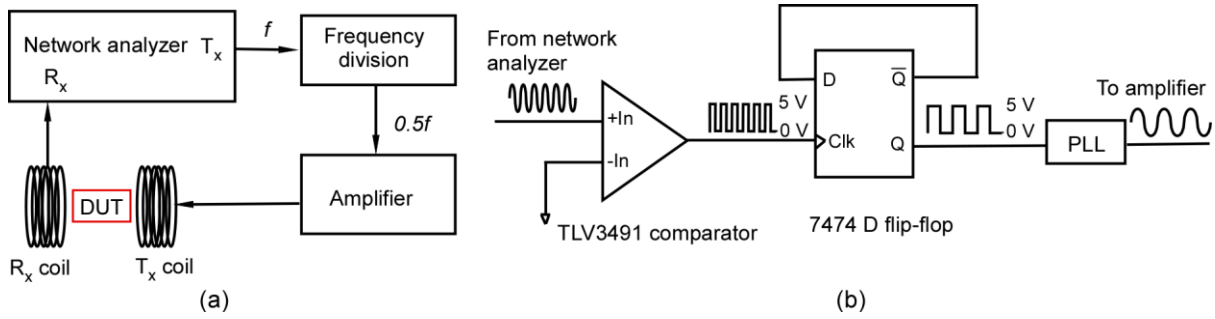


**Fig. 4.23:** (a) Harmonic detection at twice the excitation frequency using a network analyzer and a frequency divider. (b) Frequency division by two, using a comparator and a D flip flop.

The frequency division is implemented using the technique shown in Fig. 4.23(b). A comparator (TLV3491, Texas Instruments Inc., Dallas, TX) converts the sine wave signal from the network analyzer to a square wave. A D flip-flop (DM7474, Fairchild Semiconductor Corp., San Jose, CA) connected in feedback divides the frequency by two. Finally, a phase-locked loop (component of SR830 lock-in amplifier, Stanford Research Systems, Sunnyvale, CA) converts the square wave output from the D flip-flop to a sine wave signal, which is then fed to the amplifier.

*B. PC-controlled data acquisition*

In this technique, an NI LabVIEW program and associated data acquisition hardware is used to generate the excitation frequencies and acquire the receive signal. The PC controls a data acquisition device (NI USB-6341) using LabVIEW software. A lock-in amplifier (SR830,

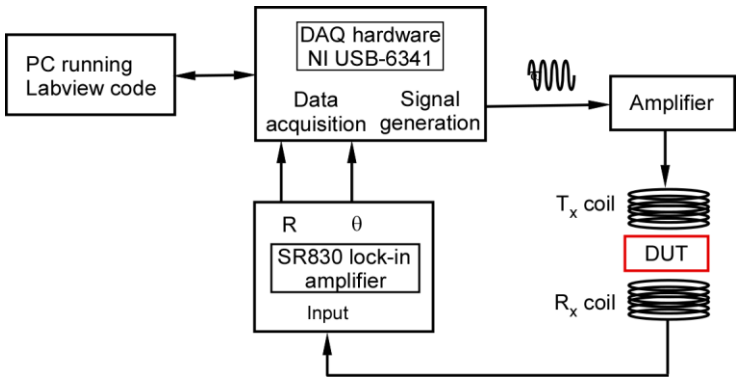


**Fig. 4.24:** Harmonic detection using PC interfaced with data acquisition hardware and lock-in amplifier.

Stanford Research Systems, Sunnyvale, CA) is used in conjunction with this setup to analyze the resonator response. The lock-in amplifier downconverts the received signal before acquisition by the USB-6341 device. The downconversion is performed by quadrature mixing with a sinusoid at twice the excitation frequency. In this manner, the receive section scans the response at twice the excitation frequency. Figure 4.24 shows the system implementation.

*C. Test resonator and coil arrangement*

The test resonator is fabricated from 29 μm thick sheets of Metglas 2826MB, and measures 50×10 $mm^2$. Simulation in COMSOL Multiphysics predict the first longitudinal resonant mode of vibration at 43 kHz. The resonator is clamped at its center to suppress the second longitudinal mode of vibration. The excitation and receive coils are 10 turns each and wound coaxially on a tube with a diameter of 2.5 cm. The excitation magnetic field measures approximately 200 mG, rms.

### 4.3.3 Experimental results

*A. $f_0$ excitation*

The excitation frequency was swept from 40 to 45 kHz, targeting the fundamental mode at about 44 kHz, while the receive coil scanned at twice the excitation frequency. No DC bias field

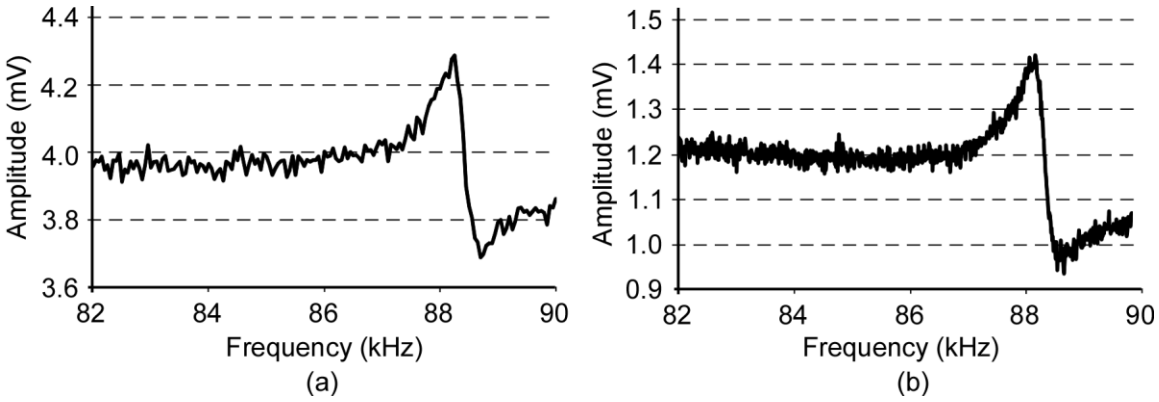


**Fig. 4.25:** Receive coil voltage as a function of the frequency for (a) modified gain-phase analyzer method, and (b) PC-controlled data acquisition and analysis method. As expected, a peak is observed at 88.3 kHz which is twice the fundamental mode.

was applied. Figure 4.25(a) shows the spectrum for the modified gain-phase analyzer method, while Fig. 4.25(b) shows the spectrum for the PC-controlled data acquisition and control method. The frequency spectrum shows a peak at 88.3 kHz, which is, as expected, twice the resonant frequency of the device. The absolute voltage amplitudes differ between the two methods due to some voltage scaling at the receive terminal of the network analyzer.

*B. $0.5f_0$ excitation*

The excitation frequency was swept from 20 to 25 kHz, while the receive coils scanned the 40 to 50 kHz range. No DC bias field was applied. The voltage at the receive coil as a function of the frequency shows a peak at the resonant frequency i.e. 44.15 kHz (Fig. 4.26).

### 4.3.4 Discussion

Both $0.5f_0$ and $f_0$ excitation methods result in approximately similar received signal strength at no applied DC bias field. However, the difference between the two is apparent when the bias field is applied and varied. Figure 4.27 shows the variation in the amplitude of the harmonic measured as voltage at the receive coil as a function of applied DC bias field for both the methods.

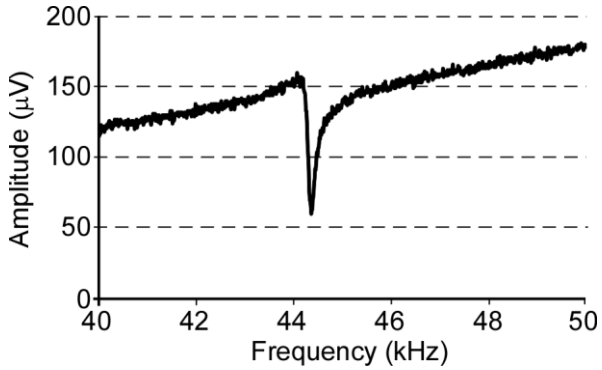


**Fig. 4.26:** Receive coil voltage as a function of frequency using the PC-controlled data acquisition technique. The readings are expected to be same for the modified gain-phase analyzer technique.

The amplitude is normalized to applied interrogation magnetic field. The two peaks in the curve possibly correspond to regions of higher non-linearity in the material properties which, in turn, results in higher harmonic response. Although the dependence of magnetostriction on the square of magnetic field is similar both at zero bias field and applied bias field, the non-linearities in other material properties (such as in magnetization and stress-strain characteristic) result in strong signal amplitudes in presence of applied bias fields.

The $f_0$ excitation method generates a much stronger response than the $0.5f_0$ excitation. This is because, in contrast to the $0.5f_0$ excitation method, direct excitation of a resonance mode (as done with the $f_0$ excitation method) results in a much stronger vibratory response, and consequently a stronger harmonic response.

The use of harmonic of the sensor response decouples the excitation signal from the harmonic sensor response in the frequency domain. However, in the present implementation, it does not reject the excitation energy from the receive circuit. Complete decoupling of excitation energy from the harmonic sensor response can be achieved by the use of a high-pass filter or a band-pass filter after the receive coil. This would allow the use of stronger excitation magnetic fields without overloading or saturating the receive circuit.

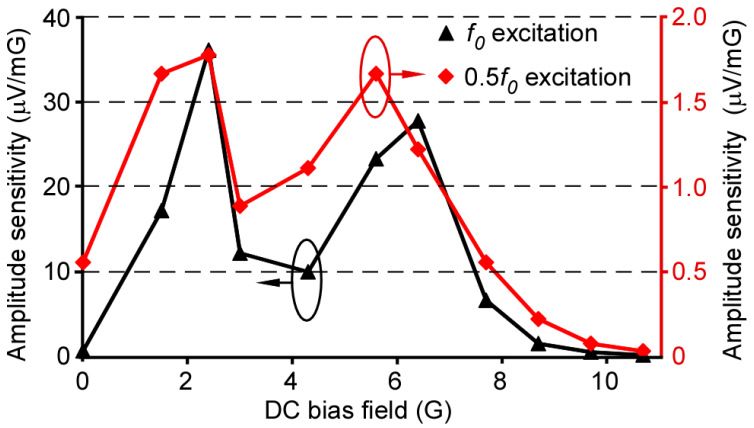


**Fig. 4.27:** Amplitude of resonant peak observed in the received coil voltage at the harmonic of the excitation frequency for $f_0$ excitation (resonant peak at approximately 88 kHz) and 0.5$f_0$ excitation (resonant peak at approximately 44 kHz).

### 4.4 Decoupling through physical layout of coils

In the frequency sweep approach to determine resonant frequencies (as used in Chapter 2), both the transmit and the receive coil operate simultaneously at identical frequency bands. The coupling between the transmit and the receive coils is dependent on coil geometry and relative orientation. The baseline receive coil voltage (i.e. voltage in absence of a resonant peak) is the measure of the coupling between the transmit and the receive coils (Fig. 4.1). Positioning the receive coil at a null-point in the transmit field reduces the coupling between the two and reduces the baseline. This is the approach that was followed for interrogation coil design in Chapter 2.

Finite element analysis (FEA) provides a tool to determine self-inductances and mutual inductances between transmit and receive coils. These values determine the baseline receive coil voltage. The simulation can be used to develop coil designs and geometries that minimize the baseline receive coil voltage.

### 4.4.1 Design

*A. Case study: three coil system*

A coil configuration of particular interest is shown in Figure 22. This coil was previously employed as a part of a magnetoelastic biliary stent sensor interrogation system [Gre13]. In addition to the transmit and the receive coil, it also has an electromagnet to generate the DC bias field necessary for resonant operation of the magnetoelastic sensor. The circuit equivalent for the above coil geometry is shown in Fig. 4.28. Subscripts 1, 2, and 3 represent elements of the bias circuit, transmit circuit, and receive circuit respectively.

The coil inductances and mutual inductances are derived from COMSOL simulation and are now described. The bias coil has a rectangular cross section of 8 × 18 $cm^2$ and has 90 turns. The simulated inductance ($L_1$) is 957 μH. The transmit coil has 10 turns each on two windings which are 13 cm in diameter and 1 cm in length. The two windings are series connected. The simulated inductance ($L_2$) is 46 μH. The receive coil has a rectangular cross section of 8 × 18 $cm^2$ and has 32 turns. The simulated inductance is 148 μH.

The mutual inductance between the bias electromagnet coil and the transmit coil ($M_{12}$) is simulated to be 19 μH. Similarly, the mutual inductance between the transmit coil and the receive

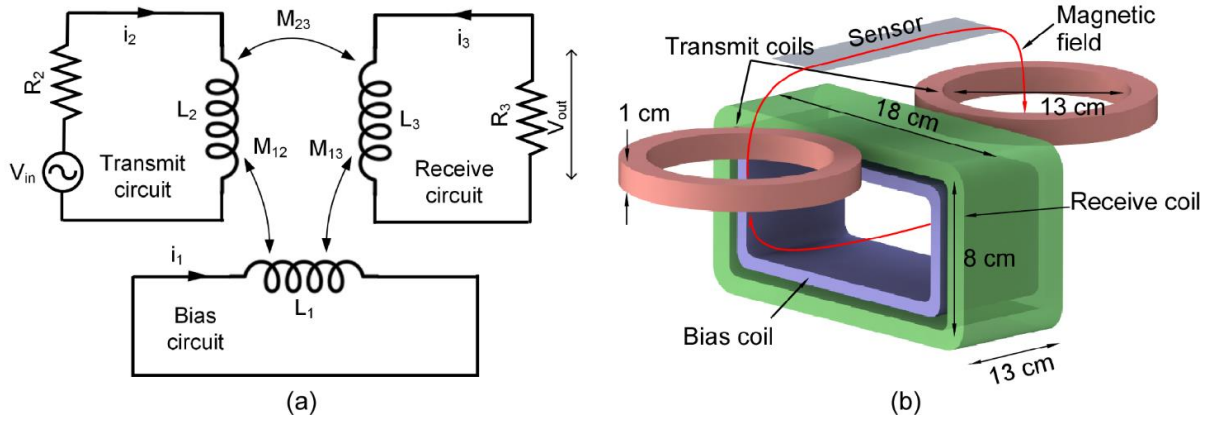


**Fig. 4.28:** (a) AC circuit equivalent showing the mutual coupling between the different coils. (b) Interrogation coil setup.

coil ($M_{23}$) is simulated to be 8 μH, while the mutual inductance between the receive coil and the bias coil ($M_{13}$) is 384 μH.

The coupling equations for the above coil geometry can be written as:

$$\begin{bmatrix} j\omega L_1 & j\omega M_{12} & j\omega M_{13} \\ j\omega M_{12} & j\omega L_2 + R_2 & j\omega M_{23} \\ j\omega M_{31} & j\omega M_{23} & j\omega L_3 + R_3 \end{bmatrix} \begin{bmatrix} i_1 \\ i_2 \\ i_3 \end{bmatrix} = \begin{bmatrix} 0 \\ v_{in} \\ 0 \end{bmatrix} \tag{4.12}$$

where $R_2$ is the output resistance of the power supply to the excitation coil (in this case, output resistance of the amplifier is specified to be 5 Ω), and $R_3$ is the input resistance of resistance of the network analyzer input terminal (i.e., 50 Ω ). Solving the above set of equations at 100 kHz for an input voltage, $v_{in}$, of 100 mV, using the COMSOL simulated values for inductances and mutual inductances, the output voltage is calculated to be 920 μV. If the bias coil is inactive, $M_{12} = M_{31} = i_3 = 0$. In this case, the output voltage is determined to be 12 mV. Experimentally, these values were found to be 1.2 mV and 18.8 mV, respectively. Hence, the simulation model is capable of estimating the operation of the interrogation coil and the effects of mutual coupling between the coils.

The presence of the bias coil reduces the baseline voltage at the receive coil. The effect of the number of turns of the bias coil on the baseline receive voltage ($V_{out}$) can also be estimated

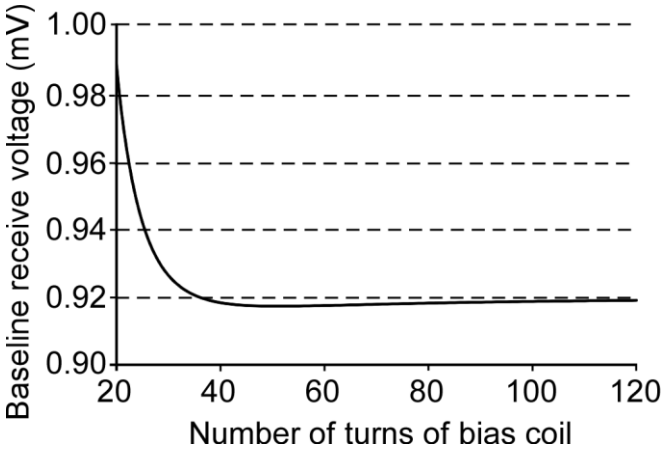


**Fig. 4.29:** Receive coil voltage as a function of the number of turns of the bias coil.

analytically. More importantly, it can be determined if there is an optimal number of turns of the bias coil that can completely cancel the baseline receive coil voltage for a given frequency. Mutual inductances $M_{12}$ and $M_{13}$ are proportional to the number of turns of the bias coil, while the inductance $L_1$ is proportional to the square of the number of turns of the bias coil. The receive coil voltage as a function of the number of turns of the bias coil is shown in Fig. 4.29. While there is a sharp drop in the baseline receive voltage values initially with increase in number of turns of the bias coil, further increasing the number of turns beyond 40 does not significantly affect the baseline levels. With this coil arrangement, it is not possible to completely cancel the baseline received signal.

*B. Differential coil design*

A differential arrangement has been previously reported that cancels the baseline voltage at the receive coil [She10]. A similar approach can be followed for improving the previously described coil setup, taking into consideration the influence of the bias coil. The receive circuit consists of two coil segments with opposing polarity of coupling with the transmit magnetic field (Fig. 4.30(a)). One of the segments should be coupled strongly to the transmit coil while very weakly coupled to the resonator. This segment is called the baseline canceling coil. The second segment is the receive coil, and is coupled to both the transmit coil and the resonator. Figure 4.30(b) shows the geometry of the interrogation coil studied in this report.

The coil inductances and mutual inductances are derived from COMSOL simulation. The bias coil has a rectangular cross section of $16 \times 3$ cm$^2$ and has 90 turns. The simulated inductance ($L_2$) is 514 μH. The transmit coil, as before, has 10 turns each on two windings which are 13 cm in diameter and 1 cm length for each winding. The two windings are series connected. The simulated inductance ($L_2$) is 46 μH. The receive coil has has a rectangular cross section of $18 \times 8$

cm$^2$ and 32 turns. The baseline canceling coil has cross section of 16 × 3 cm$^2$ and $Y$ turns. The simulated inductance in the receive circuit is given as:

$$L_3 = (148 + 0.075Y^2 - 1.87Y)\ \mu H \tag{4.13}$$

The first term is the self-inductance of the receive coil and the second term is the self-inductance of the baseline canceling coil. The negative term is due to the mutual coupling between the two coil segments in the receive circuit.

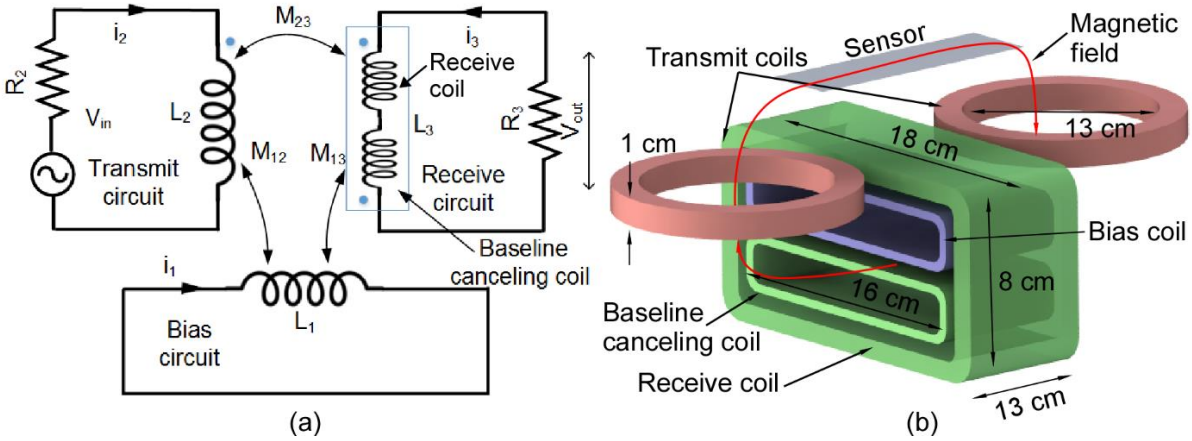


**Fig. 4.30:** (a) AC circuit equivalent of the interrogation coil setup. Baseline canceling coil is connected in series with the receive coil. (b) Interrogation coil setup for baseline cancelation.

The mutual inductance between the bias and the transmit coil ($M_{12}$) is 11.4 μH. Similarly, the mutual inductance between the transmit coil and the receive coil ($M_{23,1}$) is simulated to be 8 μH, while the mutual inductance between the bias coil and the receive coil ($M_{13,1}$) is 144 μH. The mutual inductance between the transmit coil and the baseline canceling coil ($M_{23,2}$) is 0.1$M$ μH, while the mutual inductance between the bias coil and the baseline canceling coil ($M_{13,2}$) is 0.9$M$ μH.

The coupling equations for the interrogating coil geometry can be written as:

$$\begin{bmatrix} j\omega L_1 & j\omega M_{12} & j\omega(M_{13,1} - M_{13,2}) \\ j\omega M_{12} & j\omega L_2 + R_2 & j\omega(M_{23,1} - M_{23,2}) \\ j\omega(M_{13,1} - M_{13,2}) & j\omega(M_{23,1} - M_{23,2}) & j\omega L_3 + R_3 \end{bmatrix} \begin{bmatrix} i_1 \\ i_2 \\ i_3 \end{bmatrix} = \begin{bmatrix} 0 \\ v_{in} \\ 0 \end{bmatrix} \tag{4.14}$$

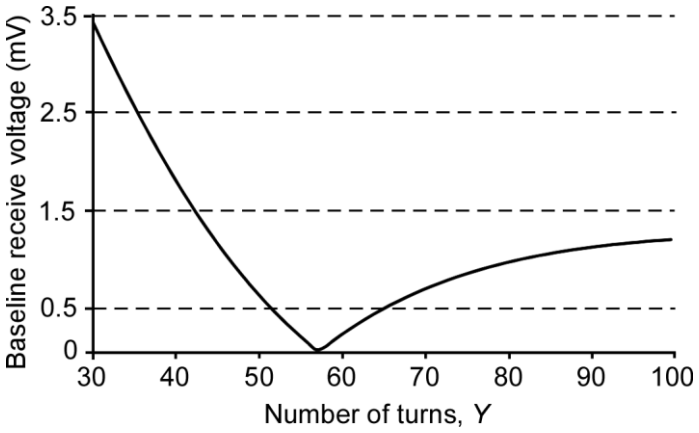


**Fig. 4.31:** Simulated baseline voltage as a function of the number of turns of the baseline canceling coil.

For baseline voltage at $v_{out}$ to be zero, $i_3$ should be zero. Based on the simulated inductances, the number of turns on the baseline canceling coil for zero baseline voltage can be estimated by solving Equation (4.14). Figure 4.31 shows the simulated baseline receive coil voltage as a function of number of turns of the baseline canceling coil. It is clear that 57 turns in the baseline canceling coil results in a zero baseline receive voltage according to the model.

The baseline canceling coil will couple to the magnetoelastic sensor as well. This will result in cancelation of part of the received resonator signal. However, the baseline canceling coil is farther away from the resonator than the receive coil, and thus is less strongly coupled to the sensor. As a result, the resonator signal is not completely canceled out by the baseline canceling coil.

## 4.5 Summary

This chapter describes three techniques for decoupling of the excitation energy from the magnetoelastic sensor response. Temporal decoupling is implemented, and measurements acquired by means of an FLL. The system is experimentally characterized with two designs of wireless magnetoelastic strain sensors. Frequency domain decoupling is implemented by

excitation of harmonics of a resonant device, utilizing the intrinsic non-linear properties of magnetoelastic materials. Finally, coil geometries that can potentially result in reduced coupling between the transmit and the receive coils are studied. One or more of these methods of decoupling can be used to potentially improve the performance of magnetoelastic resonator interrogation systems.

# CHAPTER 5

# CONCLUSIONS AND FUTURE WORK

The results described in Chapters 2-4 demonstrate some of the transduction capabilities of magnetoelastic materials that can be leveraged for use in biomedical devices. The work has broadly encompassed the complete feature set of magnetoelastic materials – sensing, mechanical actuation and wireless operation. The results shed new light on the potential of magnetoelastic materials for biomedical applications.

Section 5.1 provides a summary of the capabilities of the devices and methods described in this report. Section 5.2 recommends the direction of future efforts that can further advance the technology, and also outlines possible new applications based on the principles established in this work. Finally, section 5.3 summarizes the major contributions to the field that were a result of this endeavor.

## 5.1 Performance Summary

### 5.1.1 Wireless Strain Sensors

A new class of magnetoelastic strain sensors were designed and fabricated. In particular, ΔE effect, i.e., the change in stiffness of magnetoelastic materials with applied strain or magnetic field, was used to directly transduce strain into a change in the resonant frequency. This was measured as a shift in the resonant frequency and detected wirelessly using an inductive frequency swept gain-phase method. Other novel features included the use of strain absorbing spring elements for improved dynamic range and the ability to customize the sensor specifications, and

the integration of a reference resonator to compensate for temperature changes. Two sensor types were described – single and differential. The single sensor had an active area of 7×2 $mm^2$ excluding the anchors. At 23°C, it operated at a resonant frequency of 230.8 kHz and had a sensitivity of $13\times10^3$ ppm/mstrain; the dynamic range was 0.05-1.05 mstrain. The differential sensor included a strain-independent reference resonator of 2×0.5 $mm^2$ in addition to the sensing element which had an area of 2.5×0.5 $mm^2$ divided into two segments. The sensor resonance was at 266.4 kHz and reference resonance was at 492.75 kHz. The differential sensor provided a dynamic range of 0-1.85 mstrain with a sensitivity of $12.5\times10^3$ ppm/mstrain at 23°C. The reference resonator of the differential sensor was used to compensate for the temperature dependence of the Young's modulus of Metglas 2826MB, which was experimentally estimated to be -524 ppm/˚C. For an increment of 35˚C, uncompensated sensors exhibited a resonant frequency shift of up to 42% of the dynamic range for the single sensor and 30% of the dynamic range of the differential sensor, underscoring the necessity of temperature compensation. The geometry of both types of sensors can be modified to accommodate a variety of sensitivity and dynamic range requirements. Potential applications include monitoring of biomechanical implants and structural health monitoring.

### 5.1.2 Actuators for mitigation of fibrosis in glaucoma drainage devices

Multiple magnetoelastic actuators were designed and fabricated for use in Ahmed glaucoma drainage devices (AGDDs) for prevention of scar tissue formation and fibrosis. The hypothesis behind this approach was that fibrosis and scar tissue formation can be prevented by mechanically inhibiting cell growth on the implant surface. The actuators were integrated on the implant surface and remotely excited to resonance with a magnetic field generated by external coils. The fluid flow was intended to limit cellular adhesion to the implant surface that ultimately

lead to implant encapsulation and failure. Measuring $10.3 \times 5.6$ mm$^2$, the planar structures were annealed in 3D molds prior to integration to conform to the surface of the drainage devices, which had aspherical curvature. Six actuator designs were described, with varying shapes and resonance mode shapes. Resonant frequencies varied from 520 Hz to 4.7 kHz for the different designs. Flow velocities up to 266 μm/s were recorded at a wireless activation range of 25-30 mm, with peak actuator vibration amplitudes of 1.5 μm. Integrated actuators such as the ones described here have the potential to greatly enhance the effectiveness of glaucoma drainage devices at lowering eye pressure and may be useful in other areas of medicine.

### 5.1.3 Improved methods for characterizing resonant magnetoelastic devices

The performance of magnetoelastic resonator measurement systems can be improved by decoupling the excitation energy from the resonator response. Three methods of decoupling were explored – time domain decoupling, frequency domain decoupling, and decoupling by interrogation coil design. The time domain decoupling was implemented by analyzing the sensor ring-down, and a frequency-locked loop was used to track the sensor resonant frequencies. The method was demonstrated on two designs of wireless strain sensors with unstrained resonant frequencies of 123.2 kHz and 126.1 kHz. The FLL maintained lock for strain step inputs as large as 0.8 mstrain, with response time of less than 0.5 s. The method was also capable of estimating the quality factor, which is an important measurand in viscosity sensors.

Frequency domain decoupling was achieved for the first time in a magnetoelastic resonator by exploiting the non-linearities in the properties of magnetoelastic materials. Non-linear behavior results in generation of harmonics of the excitation frequencies. Coupling this with resonant excitation, wherein the sensor resonant modes are targeted, results in large amplitude signal. The

system was experimentally demonstrated for a magnetoelastic resonant device with a target resonant mode of 44.15 kHz.

Finally, some techniques for predicting the performance of interrogation coils using COMSOL simulations and analytical equations were presented. These techniques can lead to improved decoupling in swept frequency measurement systems, and to improved signal transmission efficiency in all inductive interrogation systems.

## 5.2 Future work

Several avenues can be explored for extending the device designs and the concepts described in this work. The potential is not only for improved performance through design modifications but also for widening the application space for these devices.

### 5.2.1 Anchor loss optimization in strain sensors

Anchor loss in one of the predominant loss mechanisms in any resonant device. Reduction of anchor losses in the strain sensor could potentially lead to higher vibration amplitude that would improve the detection range. An impedance mismatch between the resonant strip and the anchor would reduce the energy transferred to the substrate. Wave propagation in a resonator can be treated in a manner analogous to a transmission line (provided that the wavelength is, of course, of the same order as the beam dimension). The characteristic impedance of a bar with cross section $A$, density $\rho$, and Young's modulus $E$ is $A\sqrt{E\rho}$ [Gra75]. For a wave travelling from a bar with characteristic impedance $Z_1$ to an attached bar with characteristic impedance $Z_2$, the reflection coefficient, $R$, is given by:

$$R = \frac{Z_2 - Z_1}{Z_2 + Z_1} \tag{5.1}$$

The ideal situation is represented by a reflection coefficient of 1. A potential approach for realizing a reflection coefficient near 1 could be to use materials with different Young's moduli for the resonant strip and the anchors to minimize the energy coupled between them. The difference in Young's modulus would result in an impedance mismatch between the resonant strip and the anchor.

Another potential approach is to use quarter-wavelength attachments to acoustically isolate the resonator from the substrate [Tas10]. Such an attachment geometry would result in increased reflection from the anchors to the resonant strip. This could also potentially improve the purity of the resonant mode by effectively only allowing energies from the target mode to be isolated from the substrate, but transmitting energies from other modes out.

### 5.2.2 Strain sensor packaging

Packaging plays a key role in determining the long-term *in vivo* operation of any implantable device. Hence, packaging of the wireless strain sensors presented in this work presents a key challenge for its continued development. In addition to biocompatibility, there are other key aspects that must be kept in mind while designing the package. The package should be able to effectively transfer the strain from the substrate to the strain sensor. To enable strain transfer, the package should be flexible. The package should also be made of materials that are non-magnetic. Magnetic materials interact with magnetic fields and can negatively affect the sensor performance, especially in relation to interrogation range and signal quality. For instance, such materials can divert interrogation field away from the sensor, resulting in a reduced strength of resonant response. Maintaining a low sensor profile to reduce its impact on surrounding tissue is another aspect that should be considered for package design.

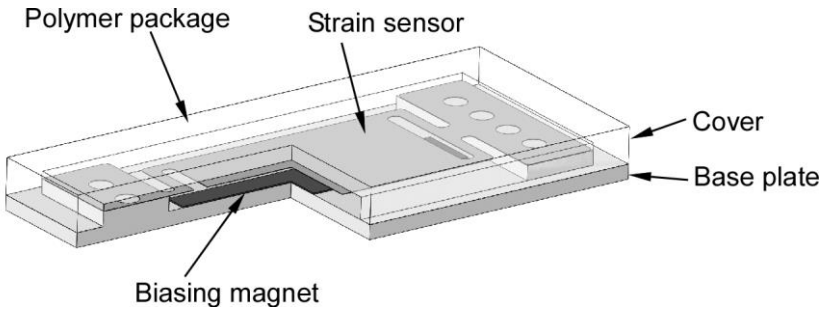


**Fig. 5.1:** Magnetoelastic strain sensor packaging.

A possible architecture that may be explored for the strain sensor packaging is shown in Fig. 5.1. The entire package can be fabricated from a biocompatible polymer like polycarbonate or polydimethylsiloxane (PDMS). The sensor is doubly-suspended across the length of the package, with the biasing magnet affixed underneath. The polymer packages can be fabricated using molding techniques. The cover and the base plate can be fabricated separately. Following attachment of the strain sensor and the biasing magnet to the base plate, the package can be sealed with the cover.

### 5.2.3 Characterizing the cross-axis sensitivity of the strain sensors

While the strain sensors are designed to measure longitudinal strain, some dependence on the transverse strain is also expected. Characterizing this cross-axis sensitivity of the strain sensors is an important aspect for determining the sensor performance. Furthermore, this can lead to the development of dual axis strain sensors that are capable of measuring the longitudinal as well as transverse strain in an integrated form factor.

### 5.2.4 Beat frequency measurement for strain sensors

The strain independent reference resonator can be used to improve the sensitivity of the strain sensor, in addition to providing the temperature compensation. For instance, if the reference

resonator is tuned to operate close to the frequency of the strain sensing element, the difference between the reference frequency and the sensor frequency would provide a more sensitive measure of strain. In addition, if the temperature induced change in frequency is, by design, identical for both the sensor and the reference resonator, the frequency difference is temperature independent.

### 5.2.5 Resonant fluidic actuation studies

The streaming motion of the microparticles in response to the oscillatory vibration of the GDD actuator points toward a possible role of acoustic streaming in generating the liquid flow [Lig78]. Further studies can be directed towards exploring the mechanism of induced liquid motion as well as methods to optimize it.

Acoustic matching of the actuator with the aqueous humor will ensure maximum energy transfer to the liquid. Acoustic impedance is the product of the density and the speed of sound in the material. Matching the impedance of the actuator with the AH involves bringing the acoustic impedances of the two closer, thereby minimizing the reflection at the actuator-AH interface.

Finally, some frequencies are more efficiently transmitted into the liquids than others. Research can be aimed at optimizing the actuator functionality by determining the frequencies that are most efficient and designing actuators to function at these frequencies.

### 5.2.6 *In vitro* and *in vivo* characterization of cell adhesion and fibrosis

The next step towards the characterization of the AGDD magnetoelastic actuators is the study of the effect on live tissue. To this end, experiments can be devised to study the actuator performance both *in vitro* and *in vivo*.

The *in vitro* study of scar tissue formation and fibrosis is typically performed using fibroblasts and endothelial cells – cells that mediate the process of fibrosis. The general protocols for such a study can be similar to the ones used for previous experiments [Vla11, Ito11]. The goal

is to study the effect of vibration on cell adhesion as a function of actuation amplitude, duration, and repetition frequency. Efficacy can be quantified through the use of fluorescence microscopy to visually observe cell proliferation and viability. A reduction of cell adhesion post-actuation would prove that the actuation is sufficient to prevent the proliferation of these cell types.

Alternatively, or in conjunction with *in vitro* studies, *in vivo* studies performed in live animal models enable direct observation of actuator influence on scar tissue formation. *In vivo g*laucoma studies can be performed using different animal models [Pra95, Ess04, Min87]. The size of the animal eyeball will determine the dimensions of the glaucoma implant to be used. This should be considered while designing and fabricating the actuator for a specific implant.

### 5.2.7 Fibrosis mitigation in trabeculectomy and other procedures

The concept of actuation for fibrosis mitigation can be extended to related glaucoma surgeries like trabeculectomy. In this procedure, a flap is created in the sclera which is then sutured down to create an outlet for aqueous humor. However, the 3 to 5 year rate of failure of this surgery can be as high as 40-50% [Law09]. The most common reason for surgical failure, as with the AGDD implant surgery, is subconjunctival fibrosis and scarring that impedes the outflow of aqueous. Magnetoelastic actuators similar to the type studied in this work can be envisaged for use in this surgical procedure.

The magnetoelastic actuator can be sutured underneath the conjunctiva, surrounding the scleral flap, as illustrated in Fig. 5.1(a). It will need to conform to the curved surface of the eyeball to prevent any damage to the surrounding tissue. The actuator will be comprised of three parts – paddle, anchors, and springs (Fig. 5.1(b)). The resonant vibration of the paddle will cause agitation of the surrounding fluid and limit cell adhesion. This would prevent fibrosis in its proximity. The anchors consist of perforations which are used to suture the implant to the eyeball. Compliant

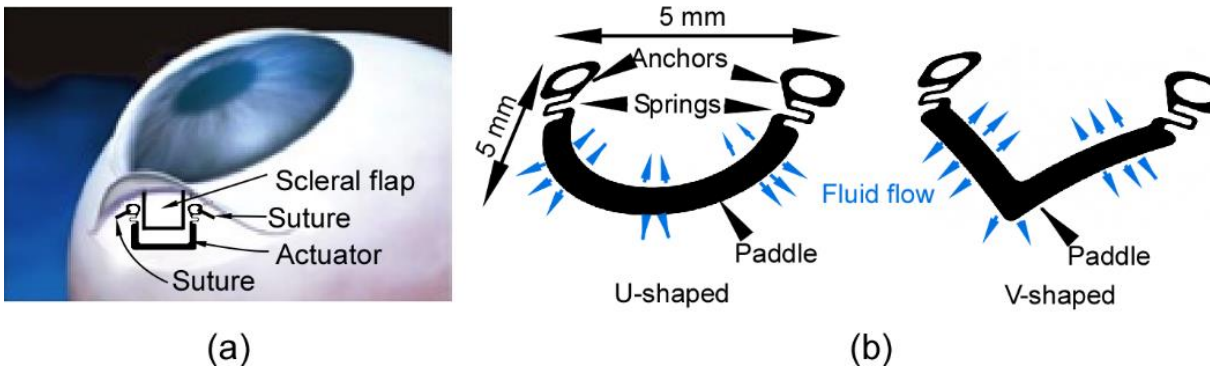


**Fig. 5.2:** (a) Actuator attachment at the location of trabeculectomy. (Image adapted from www.aeonastron.com). (b) Two actuator designs for different shapes of scleral flaps commonly made in trabeculectomy surgery.

springs, composed of folded beam structures, relieve the post-suturing stress from the anchors, ensuring that the vibrations are not damped out. Two proposed designs of the actuator are shown – U-shaped and V-shaped. The choice of the actuator will depend on the shape of the trabeculectomy flap made by the surgeon.

Cell adhesion is also an issue for bone-anchored prosthetics and other medical devices like catheters. Biofilm growth due to this adhesion and subsequent proliferation is a precursor to infection and reduced implant lifetime [Ros10, Raa98, Haz06]. Conformal magnetoelastic actuators can be devised for these implants on the same lines as the actuators presented in this report.

## 5.3 Major contributions to the field

While the strain-induced $\Delta E$ effect is a well-known and characterized phenomenon of a magnetoelastic material, its potential for use in strain sensing devices has been realized in this work for the first time. Novel magnetoelastic sensor architectures have been proposed that go beyond conventional ribbon sensors via monolithically integrated features like springs that serve to tune the dynamic range of the sensors and can also improve the resonant response. A new

integrated temperature compensation method has been established for magnetoelastic resonant devices.

The magnetoelastic transduction principles have been extended to areas that have previously not been explored. Conformal magnetoelastic actuators for fibrosis mitigation are proposed. Actuating devices are presented that, for the first time, target cell adhesion in implantable devices like the AGDD and can operate in fluidic environments. This has been made possible by the use of novel fabrication techniques including thermal annealing to produce resonators with aspherical curvature. Particle streaking measurements have been used for the first time for magnetoelastic actuator characterization. For flexural mode vibrations, this measurement approach provides significant advantages over conventional inductive coupling approaches.

Finally, new methodologies of measurement of magnetoelastic devices are explored. The techniques emphasized the separation of the device response from the interrogation signal. This paves the path towards long range detection and improved signal-to-noise ratios.

Taken together, the advancements made in this work contribute to extension of the applicability of magnetoelastic materials in relation to their use as implantable biomedical devices. In addition, the measurement and characterization methods developed expand the toolset available to engineer a new generation of magnetoelastic resonant devices.

# Appendix A

## Finite Element Analysis of Amorphous Magnetoelastic Materials

Finite element analysis (FEA) provides a useful tool for design optimization and performance estimation of magnetoelastic structures. This section describes the implementation of a finite element model to simulate operation of amorphous magnetoelastic materials using COMSOL Multiphysics (versions 4 and 5). Coupled mechanical-magnetic field physics is used to model the oscillatory response. In addition, acoustic physics can be integrated into the simulation to model liquid flow caused by mechanical motion of a magnetoelastic device.

### A.1 Constitutive equations

The small-signal operation about a bias field and stress state of a magnetoelastic material can be modeled by the coupled magnetomechanical equations [IEE91]:

$$[\varepsilon] = [s^H][\sigma] + [d][H] \tag{A.1}$$

$$[B] = [d]^T[\sigma] + [\mu^\sigma][H] \tag{A.2}$$

where $[\sigma]$ is stress tensor, $[\varepsilon]$ is strain tensor, $[B]$ is magnetic flux density and $[H]$ is magnetic field intensity (all small signal). $[s^H]$ is the compliance matrix at constant magnetic field intensity, $[\mu^\sigma]$ is the permeability matrix at constant stress, and $[d]$ is the magnetostrictivity matrix.

For amorphous materials, which behave isotropically, the coupled equations can be expressed in their full form as:

$$\begin{bmatrix}\varepsilon_{xx}\\ \varepsilon_{yy}\\ \varepsilon_{zz}\\ \varepsilon_{xy}\\ \varepsilon_{yz}\\ \varepsilon_{zx}\end{bmatrix} = \frac{1}{E^H}\begin{bmatrix}1 & -\nu & -\nu & 0 & 0 & 0\\ -\nu & 1 & -\nu & 0 & 0 & 0\\ -\nu & -\nu & 1 & 0 & 0 & 0\\ 0 & 0 & 0 & (1+\nu) & 0 & 0\\ 0 & 0 & 0 & 0 & (1+\nu) & 0\\ 0 & 0 & 0 & 0 & 0 & (1+\nu)\end{bmatrix}\begin{bmatrix}\sigma_{xx}\\ \sigma_{yy}\\ \sigma_{zz}\\ \sigma_{xy}\\ \sigma_{yz}\\ \sigma_{zx}\end{bmatrix} + \begin{bmatrix}d_{xx} & d_{xy} & d_{xy}\\ d_{xy} & d_{xx} & d_{xy}\\ d_{xy} & d_{xy} & d_{xx}\\ 0 & 0 & 0\\ 0 & 0 & 0\\ 0 & 0 & 0\end{bmatrix}\begin{bmatrix}H_x\\ H_y\\ H_z\end{bmatrix} \tag{A.3}$$

$$\begin{bmatrix}B_x\\ B_y\\ B_z\end{bmatrix} = \begin{bmatrix}d_{xx} & d_{xy} & d_{xy} & 0 & 0 & 0\\ d_{xy} & d_{xx} & d_{xy} & 0 & 0 & 0\\ d_{xy} & d_{xy} & d_{xx} & 0 & 0 & 0\end{bmatrix}\begin{bmatrix}\sigma_{xx}\\ \sigma_{yy}\\ \sigma_{zz}\\ \sigma_{xy}\\ \sigma_{yz}\\ \sigma_{zx}\end{bmatrix} + \begin{bmatrix}\mu^\sigma & 0 & 0\\ 0 & \mu^\sigma & 0\\ 0 & 0 & \mu^\sigma\end{bmatrix}\begin{bmatrix}H_x\\ H_y\\ H_z\end{bmatrix} \tag{A.4}$$

The subscripts *x*, *y* and *z* denote direction; $d_{xx}$ is the small signal magnetostrictivity along the direction of AC magnetic field, and $d_{xy}$ is the small signal magnetostrictivity orthogonal to applied AC magnetic field; $E^H$ is the Young's modulus at constant magnetic field intensity; $\nu$ is the Poisson's ration. The coupling between torsional stress/strain and magnetization has been assumed to be zero.

The direction of the DC biasing magnetic field plays an important role in determining the oscillatory response of a magnetoelastic device to an AC excitation magnetic field. Although the magnetization of amorphous magnetoelastic materials is isotropic, the application of the biasing magnetic field renders it anisotropic with the easy axis along the direction of biasing field. In addition, the AC excitation magnetic field is much lower in magnitude than the DC biasing field. As a result, the coupling between the stress and magnetization in the directions orthogonal to the bias field can be assumed to be negligible. This affects the magnetostrictivity matrix. If the bias field is along the *x* axis, the constitutive equations reduce to the form [Eng00]:

$$\begin{bmatrix}\varepsilon_{xx}\\ \varepsilon_{yy}\\ \varepsilon_{zz}\\ \varepsilon_{xy}\\ \varepsilon_{yz}\\ \varepsilon_{zx}\end{bmatrix} = \frac{1}{E^H}\begin{bmatrix}1 & -\nu & -\nu & 0 & 0 & 0\\ -\nu & 1 & -\nu & 0 & 0 & 0\\ -\nu & -\nu & 1 & 0 & 0 & 0\\ 0 & 0 & 0 & (1+\nu) & 0 & 0\\ 0 & 0 & 0 & 0 & (1+\nu) & 0\\ 0 & 0 & 0 & 0 & 0 & (1+\nu)\end{bmatrix}\begin{bmatrix}\sigma_{xx}\\ \sigma_{yy}\\ \sigma_{zz}\\ \sigma_{xy}\\ \sigma_{yz}\\ \sigma_{zx}\end{bmatrix} + \begin{bmatrix}d_{xx} & 0 & 0\\ d_{xy} & 0 & 0\\ d_{xy} & 0 & 0\\ 0 & 0 & 0\\ 0 & 0 & 0\\ 0 & 0 & 0\end{bmatrix}\begin{bmatrix}H_x\\ H_y\\ H_z\end{bmatrix} \tag{A.5}$$

$$\begin{bmatrix} B_x \\ B_y \\ B_z \end{bmatrix} = \begin{bmatrix} d_{xx} & d_{xy} & d_{xy} & 0 & 0 & 0 \\ 0 & 0 & 0 & 0 & 0 & 0 \\ 0 & 0 & 0 & 0 & 0 & 0 \end{bmatrix} \begin{bmatrix} \sigma_{xx} \\ \sigma_{yy} \\ \sigma_{zz} \\ \sigma_{xy} \\ \sigma_{yz} \\ \sigma_{zx} \end{bmatrix} + \begin{bmatrix} \mu^{\sigma} & 0 & 0 \\ 0 & \mu^{\sigma} & 0 \\ 0 & 0 & \mu^{\sigma} \end{bmatrix} \begin{bmatrix} H_x \\ H_y \\ H_z \end{bmatrix} \tag{A.6}$$

## A.2 Equation implementation in COMSOL Multiphysics

The coupled terms i.e. magnetostriction in the elasticity equation (A.5) and stress-induced magnetization in the magnetization equation (A.6) are conveniently incorporated into the solvers as magnetic field-dependent stress and stress-dependent flux density. Since COMSOL implements the magnetic field solver by first determining the flux density, *B*, equation (A.5) should be rearranged to have *B* as the independent variable. In the short form notation:

$$[\sigma] = [c^B][\varepsilon] - [c^B][d][\mu^{\sigma}]^{-1}[B] \tag{A.7}$$

where $[c^B]$ is the stiffness matrix at constant flux density and is equal to $([I] - [s^H]^{-1}[d][\mu^{-\sigma}]^{-1}[d]^T)^{-1}[s^H]^{-1}$. The stiffness matrix $[c^B]$ can also be written in terms of Young's modulus at constant flux density, $E^B$:

$$[\,c^B] = \frac{E^B}{(1+\nu)(1-2\nu)} \begin{bmatrix} 1-\nu & \nu & \nu & 0 & 0 & 0 \\ \nu & 1-\nu & \nu & 0 & 0 & 0 \\ \nu & \nu & 1-\nu & 0 & 0 & 0 \\ 0 & 0 & 0 & (1-2\nu) & 0 & 0 \\ 0 & 0 & 0 & 0 & (1-2\nu) & 0 \\ 0 & 0 & 0 & 0 & 0 & (1-2\nu) \end{bmatrix} \tag{A.8}$$

Therefore,

$$[c^B][d][\mu^{\sigma}]^{-1} = \frac{E^B}{\mu^{\sigma}(1+\nu)(1-2\nu)} \begin{bmatrix} (1-\nu)d_{xx} + 2\nu d_{xy} & 0 & 0 \\ \nu d_{xx} + d_{xy} & 0 & 0 \\ \nu d_{xx} + d_{xy} & 0 & 0 \\ 0 & 0 & 0 \\ 0 & 0 & 0 \\ 0 & 0 & 0 \end{bmatrix} \tag{A-9}$$

The term $-[c^B][d][\mu^{\sigma}]^{-1}[B]$ is incorporated into the into the "Solid Mechanics" physics (which defines the elasticity equation) in COMSOL, using the "Initial Stress" condition in the

"Linear Elastic Material" node for the magnetoelastic material. The term $[d]^T[\sigma]$ is incorporated in the "Magnetic Field" (which defines the magnetization equation) using a "Remanent Flux Density" condition in the "Ampere's Law" node for the magnetoelastic material. The non-coupled terms in both the equations, (i.e. $[c^B][\varepsilon]$ in the elasticity equation and $[\mu^\sigma][H]$ in the magnetization equation) are automatically included by COMSOL's built-in functionality for the respective physics. The expressions to be used in COMSOL to define the equation are defined in Table A.1.

TABLE A.1: EQUIVALENT COMSOL EXPRESSIONS FOR TERMS IN MAGNETOELASTIC COUPLED EQUATIONS

| **Expression** | **COMSOL expression** | **Description** |
|---|---|---|
| $\sigma_{xx,}\sigma_{yy,}\sigma_{zz,}\sigma_{xy,}\sigma_{yz,}\sigma_{xy}$ | solid.sx, solid.sy, solid.sz solid.sxy, solid.syz, solid.szx | Stress tensor |
| $B_x, B_y, B_z$ | mf.Bx, mf.By, mf.Bz | Magnetic flux density |

### A.3 The small signal magnetostrictivity

The DC strain in the direction of applied DC magnetic field for a magnetoelastic material is accompanied by a strain of opposing sign in orthogonal directions. The magnetostrictive strain in amorphous magnetoelastic material is given by:

$$\frac{\Delta l}{l} = \frac{3}{2}\lambda_s\left(\cos^2\theta - \frac{1}{3}\right) \tag{A.10}$$

where $\Delta l/l$ is the change in length in the direction of measurement, $\lambda_s$ is the saturation magnetostriction, $\theta$ is the angle between the direction of saturation magnetization and direction of measurement. The change in length measured along the direction of applied field is (i.e. for $\theta = 0°$), unsurprisingly, $\lambda_s$. Corresponding change in length transverse to the direction of magnetization (i.e., for $\theta = 90°$) is $-\lambda_s/2$. This implies that if the material expands by a certain amount in the direction of applied field, it would contract by half that value in transverse directions.

The small signal magnetostrictivity is given by the slope of the DC magnetostriction. Therefore, small signal magnetostrictivity, $d_{xy}$, transverse to the applied AC field can be related to the small signal magnetostrictivity, $d_{xx}$, in the direction of applied AC field by the simple relation:

$$d_{xy} = -\frac{1}{2} d_{xx} \tag{A.11}$$

Data reported in the literature is usually in the form of DC magnetostriction curves in the direction of applied field. The small signal magnetostrictivity in the direction of applied AC field, $d_{xx}$, is the slope of such a curve evaluated at the DC biasing field. The value of $d_{xy}$ can be obtained from

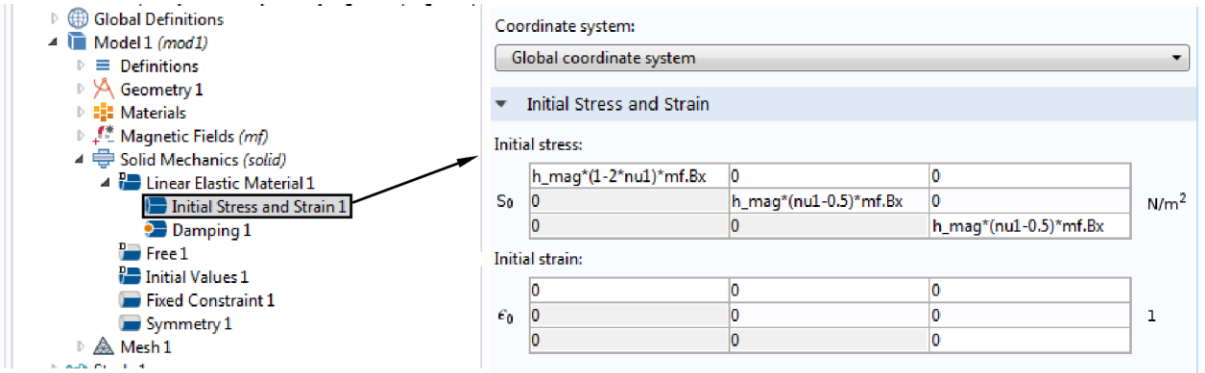


(a) Coupled elasticity equation

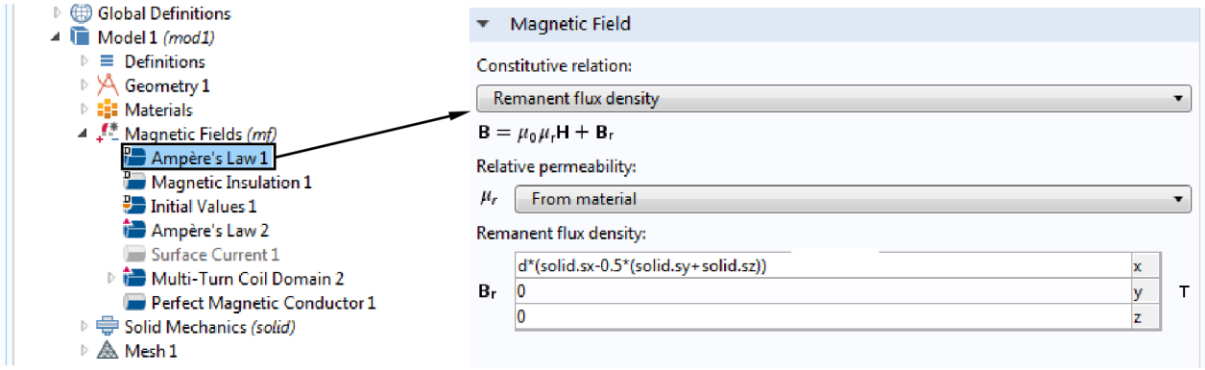


(b) Coupled magnetic fields equation

**Fig. A.1:** Defining the coupled terms in the (a) elasticity equation in "Linear Elastic Material" node under "Solid Mechanics" physics and the (b) magnetic fields equation in "Ampere's Law" node under "Magnetic Fields" physics. The parameter $h\_mag$ is defined to be equal to $\frac{E^B}{\mu^\sigma(1+\nu)(1-2\nu)}$.

equation (A.11). Based on this, the factor $[c^B][d][\mu^\sigma]$ from the coupled elasticity equation (A-7) reduces to:

$$[c^B][d][\mu^\sigma] = \frac{E^B}{\mu^\sigma(1+\nu)(1-2\nu)}\begin{bmatrix}(1-2\nu)d_{xx} & 0 & 0\\ (\nu-0.5)d_{xx} & 0 & 0\\ (\nu-0.5)d_{xx} & 0 & 0\\ 0 & 0 & 0\\ 0 & 0 & 0\\ 0 & 0 & 0\end{bmatrix} \tag{A.12}$$

Figure A.1 shows the equation view of the "Solid Mechanics" and "Magnetic Fields" physics where the coupled elasticity and magnetic field equations are defined. For this example, the DC bias field is assumed along the global *x* axis.

### A.4 Accommodating arbitrary DC bias direction

In the above treatment, the DC bias field is assumed to be aligned along the global *x* axis. If the DC bias field is along a direction other than the global coordinate system in the COMSOL simulation environment, the above equations would need to be modified. A new coordinate system can be created in a way that one of the coordinate axis is now aligned to the DC bias magnetization field. A new coordinate system can be defined in the "Definitions" section, under the heading "Coordinate Systems". A rotated coordinate system, where the new system is defined as a rotation transform (by Euler angles) of the global coordinate system, is the easiest way to accomplish this. The coupling terms $[d]^T[\sigma]$ in equation (A-6) and $-[c^B][d][\mu^\sigma]^{-1}[B]$ in equation (A.7) can now be defined in this new coordinate system. This can be implemented by selecting the newly defined coordinate system in the "Coordinate System Selection" feature under the "Ampere's Law" and "Linear Elastic Material" node.

The stress, $[\sigma]$ and magnetic flux density, $[B]$-dependent coupled terms in equations (A.6) and (A-7) are the values as defined by the new coordinate axis. In equation (A.6), the coupled $[\sigma]$ term must now, for instance, be referred by "solid.sl11" instead of "solid.sx". While COMSOL

has the built-in terms to access stress and strain in this new coordinate system in this fashion, it does not have the same feature for magnetic fields. Therefore, magnetic flux density, $[B]$, must be manually rotated from its values in the global system (mf.Bx, mf.By, mf.Bz) to align to new coordinate axis.

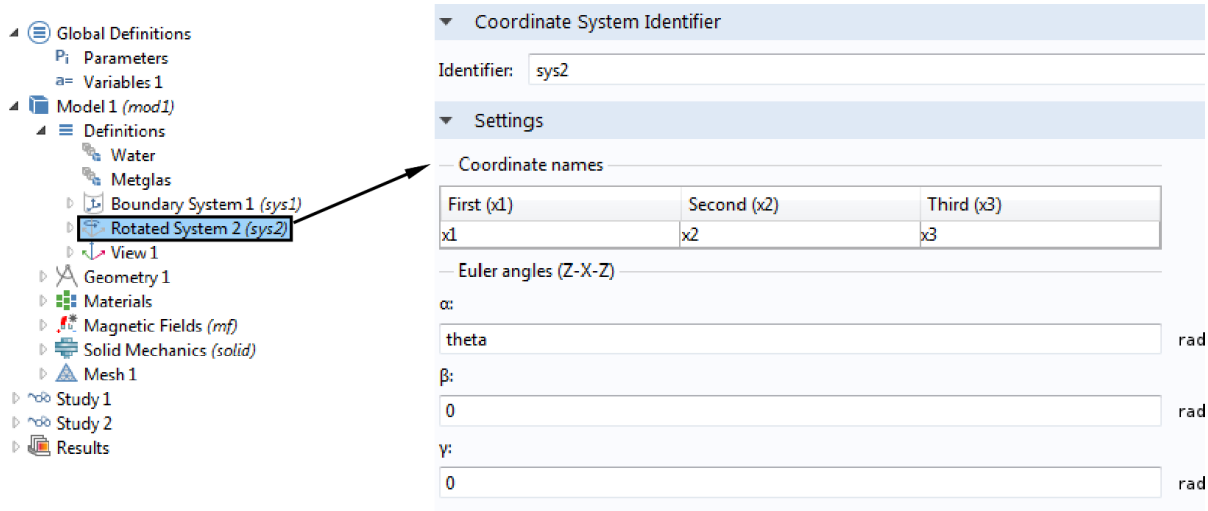


**Fig. A.2:** Defining a rotated coordinate system as Euler angle rotations of the global coordinate system.

For example, if the DC bias is along a vector in the XY plane that makes an angle $\theta$ with the global coordinate axes, a new coordinate system is defined by rotating the *x* axis to align with this bias direction. This is continuing with our convention of keeping the bias direction along the *x* axis. The rotated coordinate system is defined as shown in Fig. A.2.

The magnetic flux density, $[B]_{new}$, in this new coordinate system is defined as shown in Equation (A.13). This term, $[B]_{new}$, must be used in the coupled elasticity equation (A.7).

$$[B]_{new} = \begin{bmatrix} \text{mf. Bx}\cos(\theta) + \text{mf. By}\sin(\theta) \\ -\text{mf. Bx}\sin(\theta) + \text{mf. By}\cos(\theta) \\ \text{mf. Bz} \end{bmatrix} \tag{A.13}$$

Finally, the coupled magnetoelastic equations are now defined in COMSOL for this biasing scheme as shown in Fig. A.3. Care should be taken to ensure that the "Rotated System 2" is selected in the "Coordinate Systems Selection" drop-down menu.

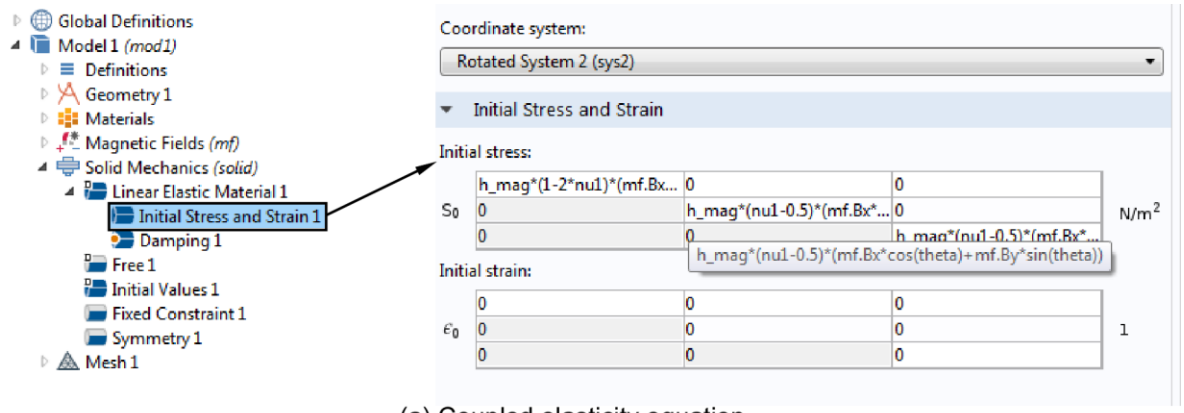


(a) Coupled elasticity equation

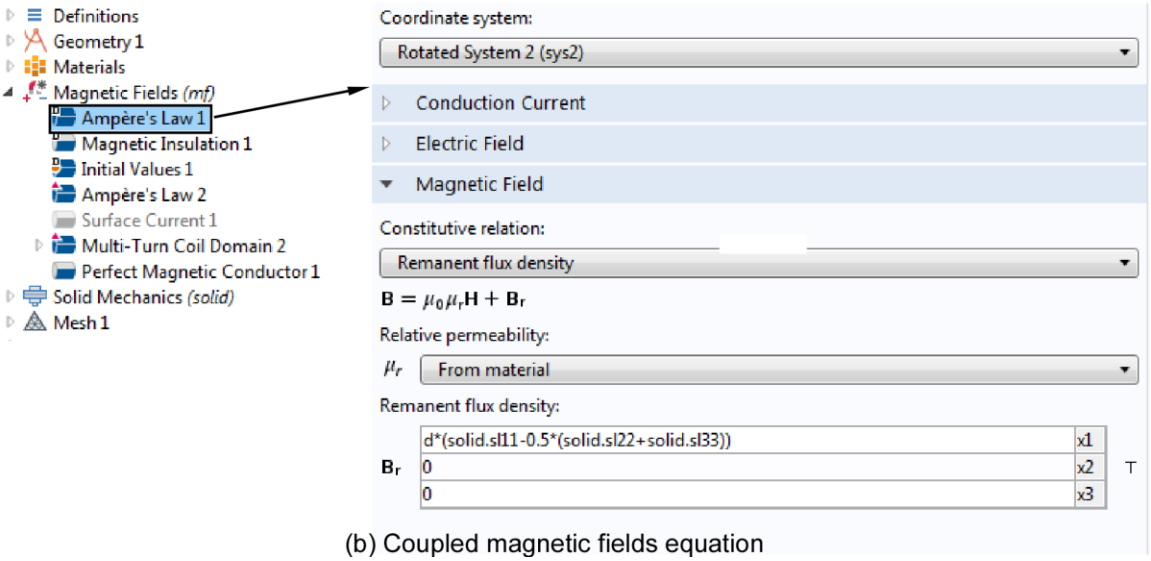


(b) Coupled magnetic fields equation

**Fig. A.3:** Defining the coupled terms in a rotated system. (a) Elasticity equation in "Linear Elastic Material" node under "Solid Mechanics" physics. (b) Magnetic fields equation in "Ampere's Law" node under "Magnetic Fields" physics. The parameter $h\_mag$ is defined to be equal to $\frac{E^B}{\mu^\sigma(1+\nu)(1-2\nu)}$.

## A.5 Damping and Environmental Mass Loading

A magnetelastic resonator is subject to damping through multiple energy loss mechanisms – magnetomechanical losses [Erc08], anchor losses, and losses to the surrounding medium. In

COMSOL, damping can be modeled using several methods. The simplest approach is to use Rayleigh damping in which fitted damping parameters are defined to replicate experimental data. Since it is based on empirical data only, any kind of damping can be modeled using this method.

Viscous and thermal losses to the surrounding medium can be explicitly modeled using the "Thermoacoustics" physics interface in COMSOL. For this, viscous damping and thermal constants of the medium must be defined in COMSOL. Other damping losses (i.e. magnetomechanical and anchor losses) must be defined separately (as Rayleigh damping parameters, for instance).

A second aspect of coupled physics that must be considered in the equivalent mass loading due to the surrounding fluid – known as hydrodynamic loading. This is a fluid-structure interaction (FSI) problem and much more prominent in transverse mode resonances in liquids. "Acoustic-Structure Interaction" and "Thermoacoustic-Structure Interaction" physics can be used to model FSI in COMSOL.

### A.5.1 Rayleigh damping

Rayleigh damping is defined in terms of mass and stiffness damping constants. This damping model is a derivative a simple mass-spring-dashpot system where the characteristic equation is given as:

$$M\frac{d^2y}{dt^2} + D\frac{dy}{dt} + Ky = 0 \tag{A.14}$$

where $y$ is the displacement, $M$ is the equivalent mass, $D$ is the equivalent damping, and $K$ is the equivalent spring constant. The damping, $D$, can be modeled as the sum of equivalent mass and stiffness proportional damping terms:

$$M\frac{d^2y}{dt^2} + (\alpha M + \beta K)\frac{dy}{dt} + Ky = 0 \tag{A.15}$$

$$\frac{d^2y}{dt^2} + (\alpha + \beta\omega_n^2)\frac{dy}{dt} + \omega_n^2 y = 0 \tag{A.16}$$

where $\omega_n$ is the radial resonant frequency of the $n^{th}$ mode, $\alpha$ is the mass damping and $\beta$ is the stiffness damping parameters. Comparing with the general form of the characteristic equation, a relation between the Rayleigh damping parameters and the damping ratio $\zeta_n$ is obtained:

$$\alpha + \beta\omega_n^2 = 2\omega_n\zeta_n \tag{A.17}$$

$$\zeta_n = \frac{\alpha}{2\omega_n} + \frac{\beta\omega_n}{2} \tag{A.18}$$

Thus, any damping can be modeled by the mass and stiffness damping parameters of a Rayleigh damping model. For simplicity in this work, however, only the mass damping parameter $\alpha$ is used to model the damping. This improves the computation time without compromising the accuracy of the model. From equation (A.17), assuming $\beta = 0$:

$$\alpha = 2\omega_n\zeta_n \tag{A.19}$$

For instance, in air, a quality factor ($Q$) of 137 is measured for the actuator described in Chapter 3. The equivalent damping ratio is:

$$\zeta = \frac{1}{2Q} = 2.5 \times 10^{-3} \tag{A.20}$$

From equation (A.19), $\alpha$ is equal to $0.005\omega_n$. Similarly, for water with a quality factor of 13, the mass damping parameter $\alpha$ is equal to $0.08\omega_n$. Here, $\omega_n$ is the radial resonant frequency of the mode being analyzed. This is important because damping parameters are dependent on the resonant mode. Appropriate precautions must be taken to ensure the suitability of parameters determined at one mode for a different resonant mode.

The "Damping" sub-node is in the "Linear Elastic Material" node under the "Solid Mechanics" physics interface. Rayleigh damping is selected under the "Damping Type".

### A.5.2 Modeling thermal and viscous damping

The thermoacoustics physics module can be used to model the damping due to the viscosity of the surrounding environment. This module includes thermal and viscous damping. To define these damping parameters, COMSOL requires the values of bulk and dynamic viscosity of the liquid, as well as the thermal conductivity and heat capacity. For water at 25℃, the bulk viscosity is $2.47\times10^{-3}$ Pa.s [Hol10], the dynamic viscosity is $1\times10^{-3}$ Pa.s [Kes78], and the thermal conductivity is 0.6 W/(m.K) [Ram95]. The heat capacity of water is 4186 J/kg℃.

The "Solid Mechanics" and "Magnetic Fields" physics interfaces remain the same as earlier, and must be defined for the magnetoelastic material. The internal magnetomechanical and anchor losses still need to be defined using Rayleigh damping parameters as shown in Appendix A.5.1.

### A.5.3 Hydrodynamic Loading

The environment surrounding a vibrating structure essentially acts as an added mass. This leads to a reduction in resonant frequency: an effect akin to added load in the structure. Previous work on estimating the virtual mass loading effect on the resonant frequencies of vibrating structures has mostly involved regular shapes such as thin rods, beams and plates [Cox12, Kwa96, Sad98, Dar01]. Approximate expressions can be derived for such structures. The virtual mass loading on complex vibrating structures of the kind studied in Chapter 3 is hard to analytically model.

COMSOL's functionality to model FSI can be used for this purpose. "Acoustic-Structure Interaction" or "Thermoacoustic-Structure Interaction" physics can be used to model this behavior. The difference between the two is that "Thermoacoustic-Structure Interaction" can explicitly model viscous and thermal damping losses. Both the physics interfaces have built-in "Solid

Mechanics" physics that can be used to define the coupled elasticity equation and the mechanical boundary conditions. The "Magnetic Fields" physics interface must still be defined to model the coupled magnetization equation.

## A.7 Simulation Parameters in COMSOL Multiphysics

The numerical values of the parameters used in the simulation model are defined in Table A.2. It should be noted that the parameters $E^B$ and $d$ are dependent on the DC bias magnetization which can show local variations within the same device. As such, the equivalent values must be used to ensure compliance with experimental results.

TABLE A.2: MATERIAL CONSTANTS FOR METGLAS 2826MB USED IN COMSOL SIMULATION

| Parameter | Value |
|---|---|
| Young's modulus, $E^B$ | 80 GPa |
| Poisson's ratio, $\nu$ | 0.22 |
| Density, $\rho$ | 7900 kg/m$^3$ |
| Magnetostrictivity, $d$ | 1.25e-8 m/A |
| Relative permeability, $\mu^\sigma$ | 1000 |

## B. DC Magnetization of Metglas 2826MB by Applied Bias Field

Bias magnetization plays an important role in determining the strength of resonant response and, in the case of magnetoelastic strain sensors, the dynamic range  In this section, the range of magnetization values of Metglas 2826MB over which there is a strong resonant response is established using COMSOL simulations and experiments.  Also, the magnetization levels of the strain sensors (described in Chapter 2) due to the permanent magnets is ascertained.

### B.1 Defining the material properties in COMSOL

It should be noted that while Appendix A dealt with modeling the resonant behavior under small signal AC magnetic field excitation, this section deals with modeling behavior in comparatively large fields used for bias magnetization.  Due to the non-linear nature of magnetic materials used, special consideration should be given to their definitions in the COMSOL environment.

#### B.1.1 Metglas 2826MB

The magnetization curve for Metglas 2826MB is shown in Fig. B.1.  The BH curve can be defined in the "Materials" section of the COMSOL simulation environment and used in the "Ampere's Law" nodes in the "Magnetic Fields, No Currents" physics interface under the "Constitutive Relation" section.  Alternatively, the "Magnetic Fields" physics can also be used: the difference being that the HB curve needs to be defined and used in the "Ampere's Law" node. This is a consequence of the manner in which COMSOL handles the variables for the particular physics.

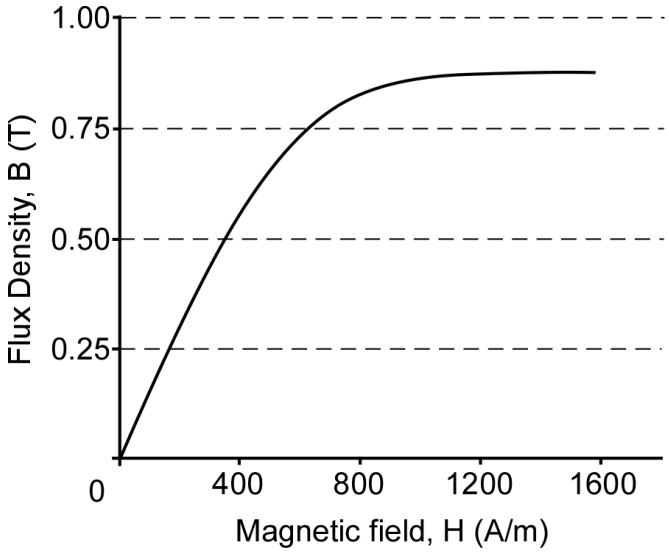


**Fig. B.1:** Magnetization curve for Metglas 2826MB [Gut13].

The values used in the BH curve for Metglas 2826MB in COMSOL is defined in Table B.1. Linear extrapolation is used beyond the limits of *H* specified here.

TABLE B.1: MAGNETIZATION DATA FOR METGLAS 2826MB [GUT13]

| H (A/m) | B (T) | H (A/m) | B (T) |
|---|---|---|---|
| 0 | 0 | 796 | 0.82 |
| 80 | 0.15 | 875 | 0.85 |
| 159 | 0.27 | 955 | 0.86 |
| 239 | 0.37 | 1035 | 0.865 |
| 318 | 0.46 | 1114 | 0.87 |
| 399 | 0.54 | 1194 | 0.875 |
| 477 | 0.64 | 1273 | 0.878 |
| 557 | 0.7 | 1353 | 0.88 |
| 637 | 0.75 | 1432 | 0.88 |
| 716 | 0.79 | 1512 | 0.88 |

### B.1.2 Biasing magnets

Setting the properties of a permanent magnet in COMSOL requires some care. Permanent magnet materials are defined by the coercivity ($H_c$), remanence ($B_r$), and the shape of the BH

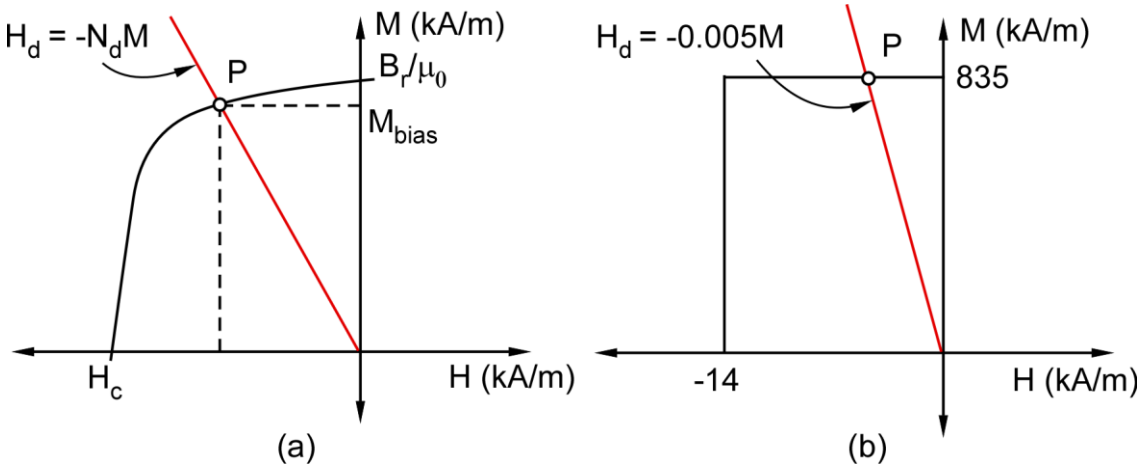


**Fig. B.2:** (a) Operating point, P, of a permanent magnet. (b) Approximating the operating point of an Arnokrome 3 magnet.

curve. Due to the presence of demagnetizing fields, the magnetization of a permanent magnet material also depends on its physical shape. The demagnetizing field in a magnetic material, $H_d$ is given by the equation:

$$H_d = -N_d M \tag{B.1}$$

The values of $N_d$ for different shapes are available in literature [Che05, Cul09b]. This equation sets the load line on the magnetization curve. The operating point of a permanent magnet is the intersection of the BH curve in the second quadrant and the load line (Fig. B-1) [Cul09c]. The corresponding value of magnetization, $M_{bias}$ is the magnetization that should be used in simulations.

For example, Arnokrome 3 has a remanence of 0.9-1.2 T and a coercivity of 4-24 kA/m, while the exact BH curve is not reported in the data sheet [Arn00]. An approximate rectangular BH curve can be assumed in its place. Suppose the magnet measures 18×6 mm$^2$ and has a thickness of 100 μm. From [Che05], assuming a high susceptibility, the demagnetizing factor $N_d$ along the long axis is approximately 0.005. Also assuming a remanence of 1.05 T and a coercivity

of 14 kA/m, which are the averages of the ranges provided in the data sheet, the intersection of the load line and the BH curve is at 835 kA/m. This is the longitudinal magnetization level.

The magnetization can be defined in the "Ampere's Law" node for the permanent magnet domain in the "Constitutive Relation" section. Since the magnetization is assumed to be one-dimensional, the value is only defined along the axis of induced magnetization.

## B.2 Estimating magnetization for strong resonance

A study of this aspect of resonator performance is performed using a combination of simulation and experimental data. COMSOL simulation is used to estimate the magnetization of a magnetoelastic element in the presence of a varying DC field, while the corresponding resonant response is experimentally measured. By comparing the two results, the magnetization values that result in strongest resonance is determined.

Two rectangular strips of Metglas 2826MB measuring 36×6 $mm^2$ and 18×6 $mm^2$ are studied. The strips are biased by Arnokrome 3 magnets of the same size as the corresponding Metglas strips. The magnets measure 100 μm thick and are magnetized along their long axis. Figure B.3 shows the model used in the simulation. Only half of the cylindrical air domain is used for simulation; a symmetry boundary condition – "Magnetic Insulation" is used on the "cut" surface of the cylinder. The separation between the magnet and the Metglas resonator is varied from 1 mm to 11 mm and the average magnetization along the long axis of the Metglas resonator is estimated. The average magnetization is estimated by integrating the longitudinal magnetization over the resonator volume and divided by the total volume.

The separation, *d*, between the magnet and the resonator is experimentally increased in steps of 1 mm and the corresponding resonant response is measured in the frequency domain. A

coaxial coil setup with 10 turns each of transmit and receive coil is used. Figure B.4 shows the resonance amplitude as a function of separation, $d$.

A minimum magnetization of 100 kA/m is needed to generate a response from the resonator. Possibly lower magnetization levels can generate a response from the larger device. The maximum response is obtained at a magnetization value of approximately 300 kA/m for both the devices.

The saturation B field $(B_s)$ of Metglas 2826MB is 0.88 T (Fig. B.1). Because of the high permeability, the magnetization level at this saturated value can be approximated to $B_s/\mu_0$. The saturation magnetization is therefore approximately 700 kA/m. This value corresponds well with the experimental results. From the data shown in Fig. B-4, it is clear that the strength of resonance drops as the material gets biased closer to the saturation.

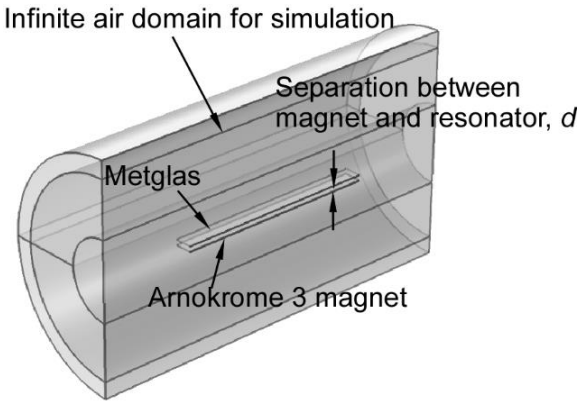


**Fig. B.3:** Model geometry in COMSOL used in bias field simulation.

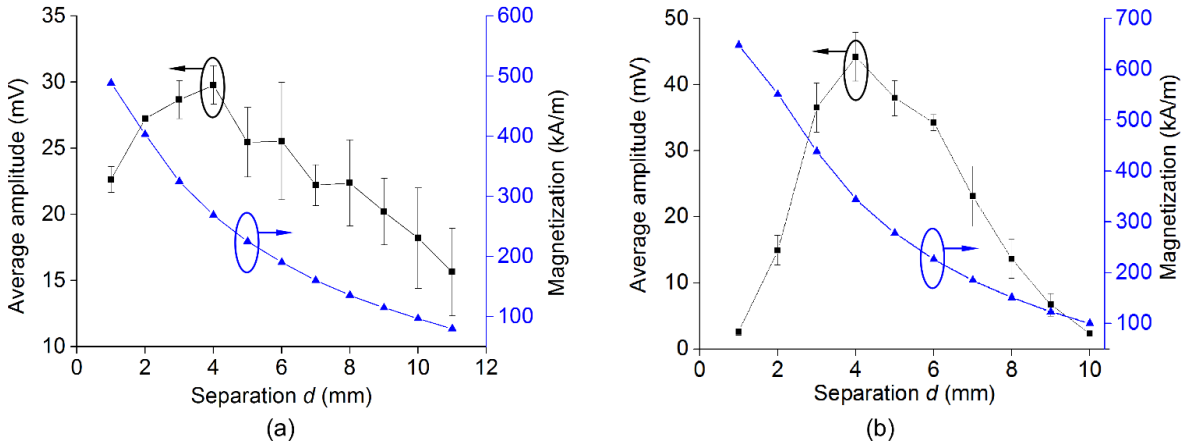


**Fig. B.4:** Magnetization state and experimental resonance amplitude as a function of separation between the magnet and the resonator. The magnets and the resonator measure (a) 36×6 mm$^2$ and (b) 18×6 mm$^2$.

## B.3 Magnetization of wireless strain sensors

Using similar concepts those outlined in Section B.2, the magnetization state of the strain sensors described in Chapter 2 due to bias magnets can be determined. The simulation model is the similar to the one shown in Fig. B.3, with the Metglas resonator replaced by the strain sensor and the biasing magnet made of Arnokrome 5 (as was used for the strain sensors). The remanence

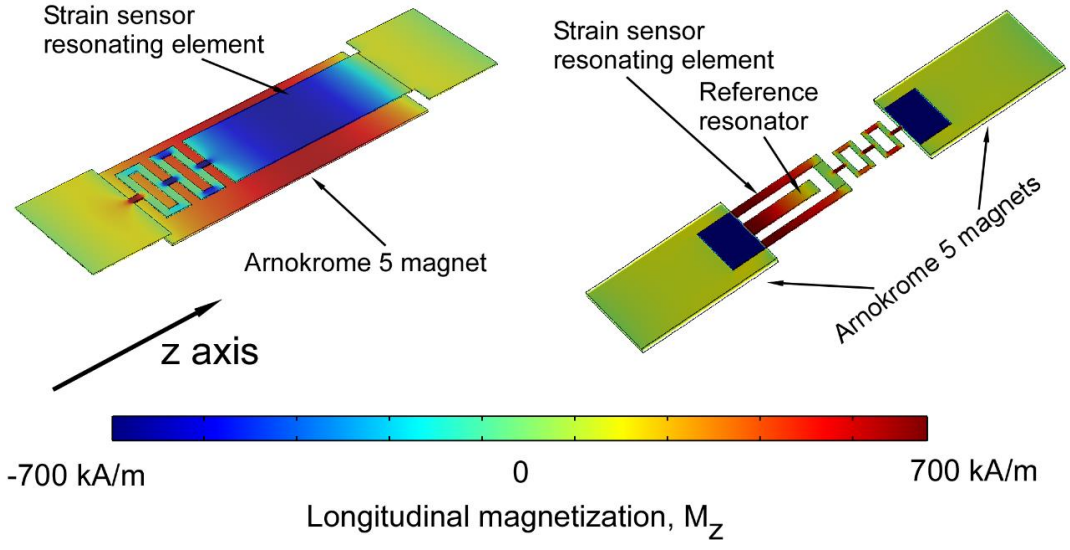


**Fig. B.5:** Longitudinal magnetization of single and differential strain sensors.

of Arnokrome 5 is taken to be 14 kG, and the coercive field is taken as 35 Oe. Using principles outlined in Appendix B.1.2 a magnetization of 900 kA/m can be assumed for the magnets.

Figure B.5 shows the magnetization for the two strain sensor designs. The resonating element of the single strain sensor has an average longitudinal magnetization of 550 kA/m. The strain sensing resonating element of the differential sensor has an average longitudinal magnetization of 640 kA/m, while that for the reference resonating element, it is 630 kA/m. The relationship between stress/strain and magnetization is derived in Appendix C.

# Appendix C

## Stress-Dependent Magnetization of Amorphous Magnetoelastic Alloys

### C.1 Stress and magnetization

Strain sensors described in Chapter 2 transduce applied strain to a change in stiffness through the ΔE effect. This effect is a consequence of change in magnetization state of the material under applied stress. The saturation magnetization of the material imposes an upper limit to the stress that can effectively result in a change in material stiffness. Thus, the dynamic range of the strain sensor, which is based on the principle of change in resonant frequency due to change in stiffness, is limited by the saturation magnetization.

Application of stress to a magnetoelastic material changes its energy state. For amorphous materials it introduces a uniaxial anisotropy [Cul09a]. The stress anisotropy energy (i.e. magnetoelastic energy) for such materials is given by:

$$E_{me} = -\frac{3}{2}\lambda_s \sigma \cos^2(\theta) \tag{C.1}$$

where $E_{me}$ is the stress induced anisotropy energy, $\lambda_s$ is the saturation magnetostriction, $\sigma$ is the applied stress, and $\theta$ is the angle between applied stress and the direction of magnetization. For positive $\sigma\lambda_s$, energy is minimized when the direction of magnetization coincides with direction of applied stress. For negative $\sigma\lambda_s$, energy is minimized when the two are orthogonal.

In amorphous materials, with domains initially oriented randomly, the magnetoelastic energy under applied stress is given as:

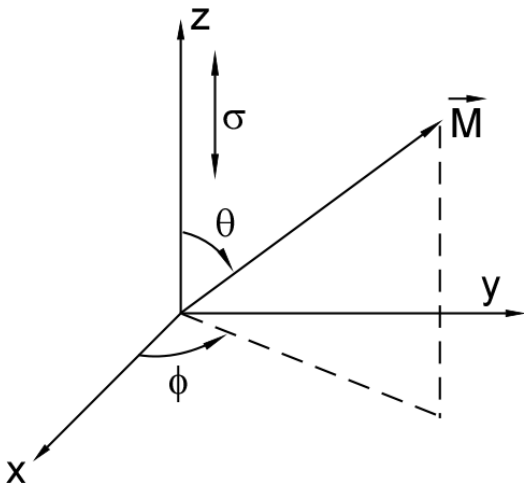


**Fig. C.1:** Stress and magnetization vectors defined in a spherical coordinate system.

$$E_{me} = -\frac{3}{2}\lambda_s \sigma \overline{\cos^2(\theta)} \tag{C.2}$$

where $\overline{\cos^2(\theta)}$ is the average over all orientations in space. Consider the stress being applied along the *z* axis in Fig. C.1, while the magnetization is defined by the polar angle $\theta$ with the *z* axis. The average value of $\cos^2(\theta)$ is given by:

$$\overline{\cos^2(\theta)} = \frac{1}{4\pi}\int_{\theta=0}^{\pi}\int_{\phi=0}^{2\pi}\cos^2(\theta)\sin(\theta)d\theta d\phi = \frac{1}{3} \tag{C.3}$$

Therefore, magnetoelastic energy in a randomly oriented magnetoelastic material under stress is:

$$E_{me,i} = -\frac{1}{2}\lambda_s \sigma \tag{C.4}$$

When all domains are oriented along the axis of applied stress, the magnetoelastic energy is given by:

$$E_{me,f} = -\frac{3}{2}\lambda_s \sigma \tag{C.5}$$

The change in magnetoelastic energy is:

$$\Delta E_{me} = -\lambda_s \sigma \tag{C.6}$$

Since the energy is reduced, a positive $\sigma\lambda_s$ results in magnetization aligning to the axis of applied stress. This energy change should be equal to the magnetization energy of the material.

The magnetization energy of a material, $E_{mag}$, that is magnetized to saturation under an applied magnetic field $H$ is given as:

$$E_{mag,sat} = \mu_0 \int_0^{M_s} H dM \tag{C.7}$$

where $H$ is the magnetic field intensity, $M$ is the magnetization, and $M_s$ is the saturation magnetization. Equating change in energy given by equation (C.6) and (C.7), we get:

$$\sigma = \frac{2\mu_0 \int_0^{M_s} H dM}{\lambda_s} \tag{C.8}$$

This is the maximum range of stress (for a positive $\sigma\lambda_s$) that can be theoretically transduced to change in magnetization in an amorphous material.

It should be noted, however, that Equation (C.6) represents the energy change when the magnetic moments align along the axis of applied stress. There is no net magnetization of the material. Figure C.2 shows a representative image of the magnetic domains aligned along the axis of stress due to stress-induced anisotropy in a material with positive magnetostriction. For the material to magnetize along a single axis, there should be a domain wall motion which requires

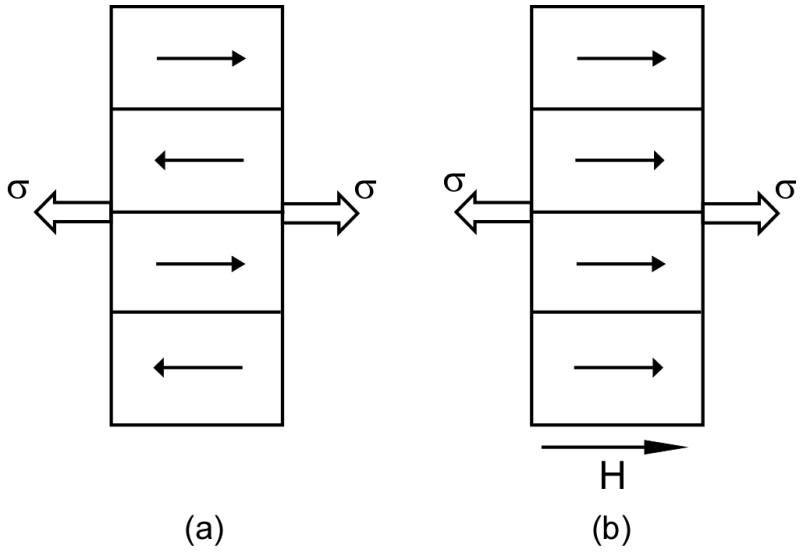


**Fig. C.2:** (a) Moment rotation due to stress-induced anisotropy in a magnetoelastic material. (b) Applied magnetic field magnetizes the material due to domain wall motion.

additional energy. This energy is, however, much smaller compared to the total magnetization energy and hence is neglected.

## C.2 Theoretical stress range of ΔE effect for Metglas 2826MB

The ΔE effect is the consequence of coupling between the magnetization and elastic strain. As a result, the ΔE effect saturates when the material is magnetized to saturation. Equation (C.8) can be used to determine the maximum strain that a magnetoelastic strain sensor can transduce to a change in magnetization and correspondingly, a change in stiffness through the ΔE effect.

The magnetization energy for Metglas 2826MB can be found from Equation (C.7). Since it has a high permeability:

$$E_{mag,sat} = \mu_0 \int_0^{M_s} HdM \approx \int_0^{B_s} HdB \tag{C.9}$$

where $B_s$ is the saturation flux density. The value of $E_{mag,sat}$ can be determined from the data in Fig. B.1; it is equal to approximately 300 J/m$^3$. Saturation magnetostriction of Metglas 2826MB is 12 ppm. Using these values in equation (C.8), the stress that would lead to saturation magnetization is found to be 50 MPa, which corresponds to a strain of 500 μstrain (assuming a Young's modulus of 100 GPa for Metglas 2826MB).

The above value is for material that is not biased. The strain sensors reported in Chapter 2 are subject to a bias magnetization, which limits the stress that can be applied before Metglas 2826MB saturates. As a result, the dynamic range is much lower than the theoretical estimate derived here. The magnetization of the sensors due to the biasing magnets is estimated via simulations described in Appendix B.3.

# Appendix D

## Safety of Magnetoelastic Materials During Magnetic Resonance Imaging

Magnetic resonance imaging (MRI) is an important diagnostic tool for imaging body tissue. However, implantable devices made of conductive and magnetic materials pose risks when exposed to the magnetic fields of an MRI device. The most significant concern is electromagnetic heating due to RF magnetic fields. This appendix describes a method of estimating the heating of a magnetoelastic material in an MRI environment using finite element analysis (FEA).

### D.1 Overview

The core concept of MRI involves the detection of signals generated by hydrogen atoms under a strong DC magnetic field when excited with an RF magnetic field. The strong DC bias field, known as the B0 field, aligns the nuclear spin of the hydrogen atoms in the direction of the field. Application of a circularly polarized RF field, known as the B1 field, rotating at the resonant frequency (also known as Larmor frequency) of the nuclei forces the magnetic moments to tip perpendicular to the direction of applied field. When the B1 field is removed the moments rotate while realigning to the direction of bias field. The signal generated by this is at the resonant frequency of the hydrogen nuclei (which depends on the magnitude of B0 field) and can be picked up by the receive coils. For a B0 field of 1.5 T, the resonant frequency of the hydrogen nuclei is approximately 64 MHz, and rises to 300 MHz for a B0 field of 7 T.

Exposure to the RF magnetic field results in heating of body tissue due to eddy current generation. The effect is more pronounced in implanted conductive devices. With respect to

magnetoelastic implantable devices, temperature rise is a result of radiofrequency heating due to eddy current and hysteresis losses in the material. The heating is also maximized for devices measuring odd multiples of half-wavelength of the RF field due to the antenna effect [Woo07, Dem01].

## D.2 Safety guidelines

Power dissipation in the body is quantified in terms of specific absorption rate (SAR) in watts per kilogram. The United States Food and Drug Administration (FDA) and the International Electrotechnical Commission (IEC) have published guidelines on the safety limits with respect to heating of body tissues [FDA14, IEC10]. The guidelines are given in terms of maximum local and whole body SARs or maximum localized temperature rise over a particular volume of body tissue. Table D.1 shows the whole body and local SAR limits as specified in the FDA and IEC guidelines. The SAR ratings are averaged over specified durations. Local SAR ratings are averaged over 1 g of tissue for the FDA guidelines and over 10 g of tissue for the IEC guidelines. In addition, IEC recommends temperature rise to be limited to 0.5℃ in the normal level of use over 6 minutes.

TABLE D.1: FDA AND IEC SAR GUIDELINES FOR TISSUE HEATING IN MRI [FDA14, IEC10]

| | **Whole body** | **Averaged in head** | **Head/torso (Local)** | **Extremities (Local)** |
|---|---|---|---|---|
| **FDA** | 4 W/kg over 15 minutes | 3 W/kg over 10 minutes | 8 W/kg over 5 minutes in 1 g tissue | 12 W/kg over 5 minutes in 1 g tissue |
| **IEC (normal level)** | 2 W/kg over 6 minutes | 3.2 W/kg over 6 minutes | 10 W/kg over 6 minutes in 10 g tissue | 20 W/kg over 6 minutes in 10 g tissue |

## D.3 Simulating eddy current heating in body tissue

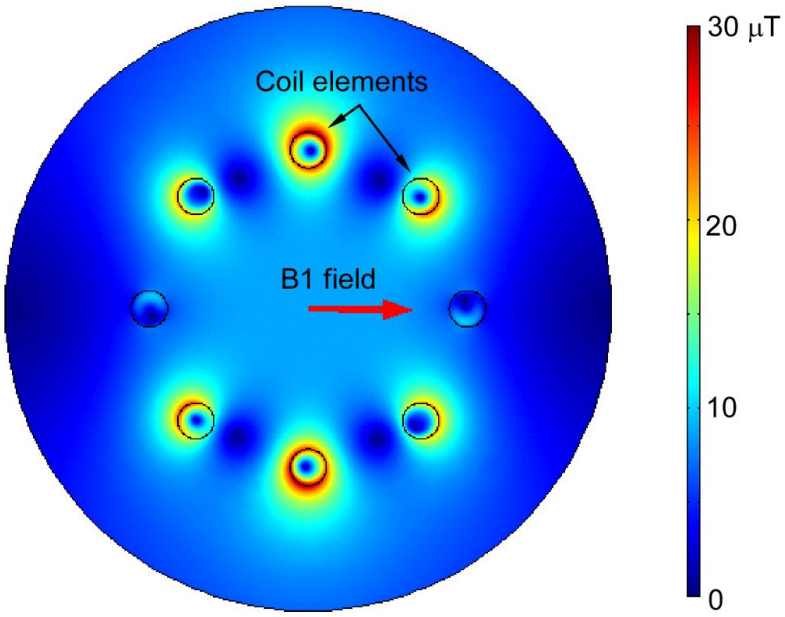


**Fig. D.1:** Circularly polarized B1 field that rotates at the Larmor frequency of hydrogen nuclei.

A 2D simulation is used to simplify the FEA model. Figure D.1 shows the circularly polarized B1 magnetic field generated by a birdcage coil design. Such a coil design is used in MRI machines to generate uniform magnetic fields [Hay85, Wat88]. The circularly polarized field is generated by separating the currents in the coil elements in phase by 45°. The amplitude of the B1 field is 10 μT in this simulation. The field rotates at 64 MHz which is the Larmor frequency of the hydrogen atom at 1.5 T B0 field.

The Metglas 2826MB test strip is assumed to be $2 \times 0.03$ cm$^2$ and is located at the center of the coil (Fig. D.2). The material properties of the surrounding environment resemble that of American Society of Testing and Materials (ASTM) phantom that mimics a human body [Liu13]. A transient simulation is performed in COMSOL using coupled heat transfer and magnetic fields physics. The electrical and thermal properties used for these studies for both Metglas 2826MB and the surrounding environment are shown in Table D.2.

TABLE D.2: PROPERTIES OF METGLAS 2826MB AND SURROUNDING TISSUE, AS USED IN COMSOL SIMULATION [LIU13].

| Property | ASTM phantom | Metglas 2826MB |
|---|---|---|
| Electrical conductivity (S/m) | 0.448 | 724000 |
| Relative permittivity | 80 | 1 |
| Relative permeability | 1 | 1000 |
| Heat capacity (J/(kg.K)) | 4160 | 80 |
| Thermal conductivity (W/(m.K)) | 0.42 | 450 |
| Density (kg/m$^3$) | 1000 | 8000 |

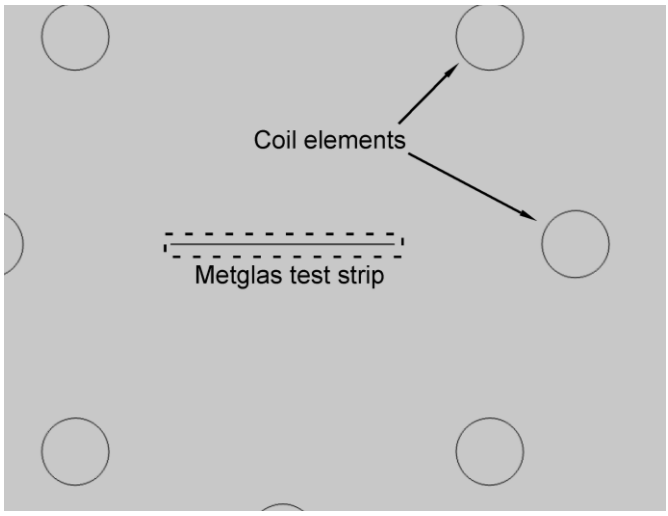


**Fig. D.2:** Location of the Metglas 2826MB test strip in the coil

Figure D.3 shows the simulated isotherm plot after 10 minutes of B1 field exposure. A maximum temperature of 310.43 K is estimated, indicating a rise of 0.43 K (0.43℃) over normal body temperature (i.e. 310 K, 38℃). This is within the IEC guideline for temperature rise.

Figure D.4 plots the temperature at the edge of the test strip over time. The electric field tends to concentrate in the sharper regions. As a result the maximum temperature rise is observed in the edges of the material.

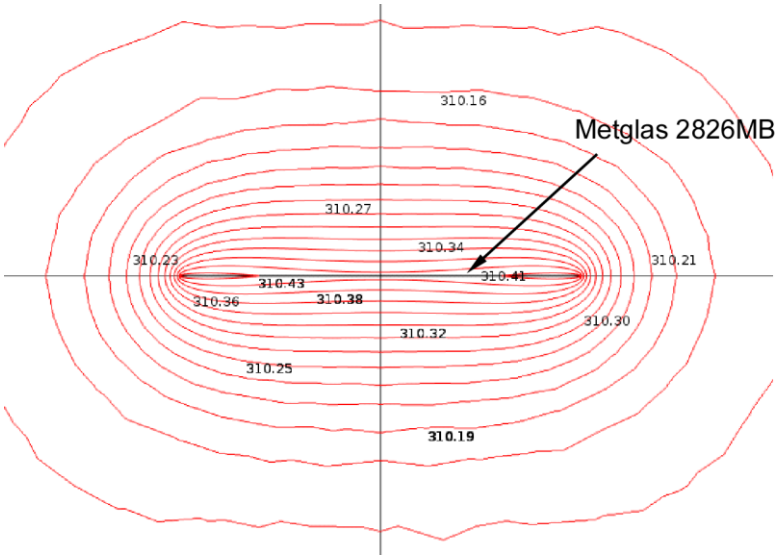


**Fig. D.3:** Simulated isotherms after 10 minutes of B1 field exposure.

Since the simulation is over a small volume and not the entire body, only local SAR values can be estimated. Averaging over 10 g of tissue surrounding the test strip (i.e. a cube 2.15 cm on the side), the local SAR value is simulated to be 2 W/kg. This is well under the local SAR limit of 8 W/kg defined by the FDA and 10 W/kg defined by the IEC.

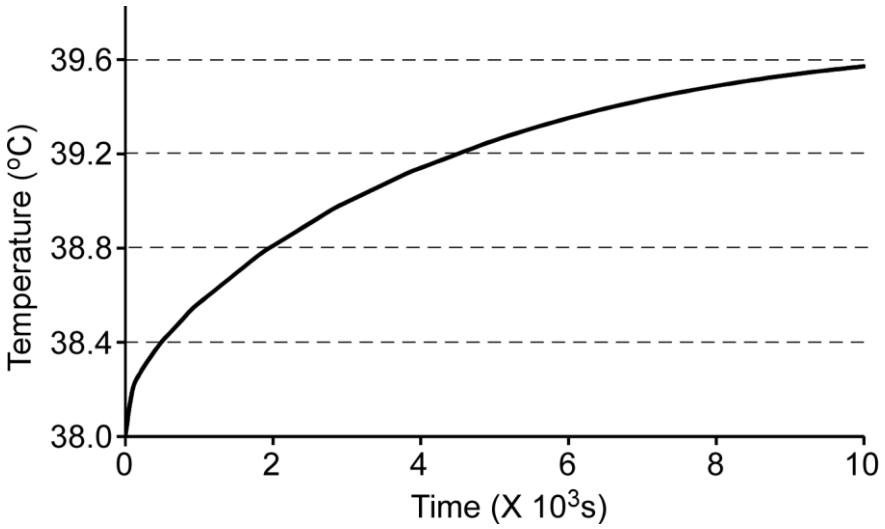


**Fig. D.4:** Temperature rise over time at the edge of the test Metglas 2826MB strip.

## D.4 Hysteresis losses

The hysteresis loss over one cycle is equal to the area enclosed by the BH curve under oscillating magnetic field. This loss is dissipated as heat in the material. Hysteresis in Metglas 2826MB occurs at fields less than 5 μT. In an MRI, the large B0 biasing magnetic field ensures Metglas 2826MB is strongly saturated. At this level any oscillating magnetic field would not produce hysteresis. As a result, the heating due to hysteresis in Metglas 2826MB can be neglected in an MRI.

# Appendix E

## Aqueous Humor Flow Dynamics

The high intraocular pressure (IOP) associated with glaucoma is a result of increased resistance to the outflow of aqueous humor (AH). A study of the elements in the AH outflow pathway would enable better understanding of the working of glaucoma drainage devices (GDDs) as well as pave the way towards actuator design for improved performance. Furthermore, parameters derived from such a study would find application in more complex simulation models that would incorporate fluid flow in the GDDs. Such simulations would provide a more complete estimation of actuator performance in *in vivo* environments.

### E.1 Flow in a normal eye

The aqueous humor outflow and pressure can be modeled as a simple circuit with resistance being used to model flow resistance of the tissue in the trabecular meshwork. AH outflow can be considered as a current equivalent and pressure is the voltage equivalent. Figure E.1 shows the outflow pathways in a normal eye and a circuit equivalent for this flow.

The intraocular pressure (IOP) acts against the episcleral venous pressure (EVP) through the resistance offered by the trabecular meshwork. Different studies have measured EVP ranging from 7.6 mmHg to 11.4 mmHg [Sit11]. The outflow through the trabecular meshwork is the conventional outflow, $V$ in Figure 3.1 (also known as trabecular outflow). In addition to trabecular outflow through the meshwork, there is a constant pressure insensitive uveoscleral outflow. The uveoscleral outflow, by itself, is not enough the keep up with the generation of AH and is found

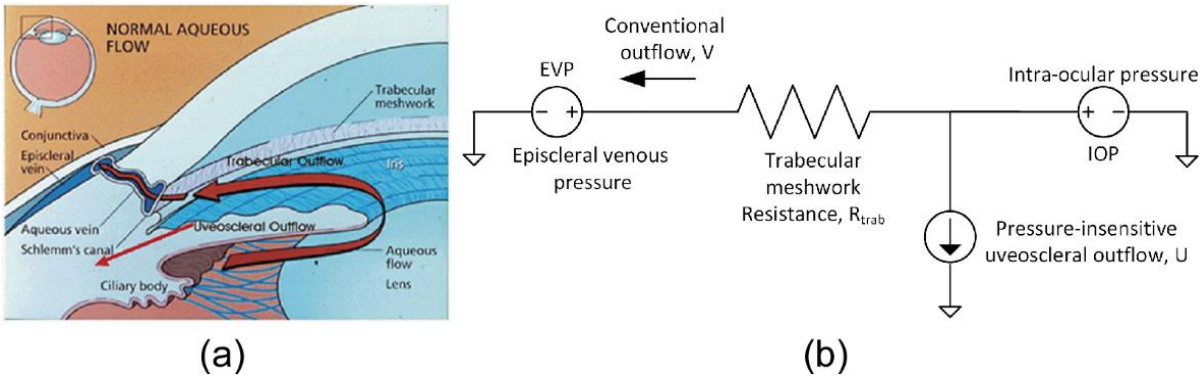


**Fig. E.1:** (a) Outflow pathways in a human eye [Ada05]. (b) Circuit equivalent of AH outflow in a normal eye.

to vary between 3% to 35% of the total AH with older subjects having a lower uveoscleral flow rate [Nil97]. The trabecular outflow rate,*V*, can be expressed as:

$$V = \frac{IOP - EVP}{R_{trab}} \tag{E.1}$$

Aqueous humor is generated at a rate of 2-3 µl/min. An increase in trabecular meshwork resistance means that IOP has to increase to accommodate the AH generation. This leads to higher IOP in the anterior and posterior chambers of the eye.

## E.2 Flow in an Eye with Ahmed Glaucoma Drainage Device

The Ahmed glaucoma drainage device (AGDD) is implanted by inserting its tube in the anterior chamber of the eye, bypassing the trabecular meshwork. The equivalent circuit for the AH flow in this case is shown in Figure E.2. The individual elements in the flow pathway are now described.

### *E.2.1 Tube resistance*

The pressure drop along the tube can be calculated using the Hagen-Poiseuille equation for pressure drop in a long cylindrical tube with a thin diameter:

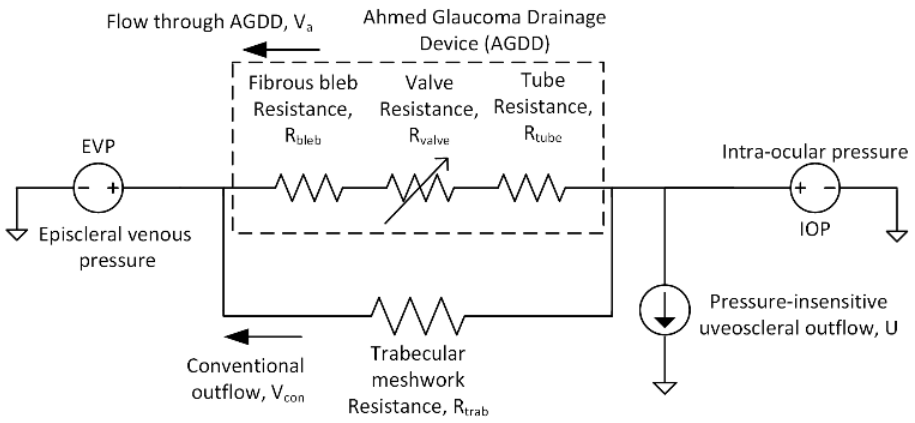


**Fig. E.2:** Circuit equivalent of AH outflow in an eye with implanted Ahmed valve.

$$\Delta P_{tube} = \frac{8\mu L V_a}{\pi r^4} \tag{E.2}$$

where $\Delta P_{tube}$ is the pressure drop along the tube, $\mu$ is the dynamic viscosity, $L$ is the tube length, $V_a$ is the volumetric flow rate through the tube, and $r$ is the tube radius.

Assuming a flow rate of 2 µl/min, tube length of 1 cm, dynamic viscosity of $7.5\times10^{-4}$ Pa.s [Hey01], and a tube radius of 0.15 mm for an Ahmed valve, the pressure drop, $\Delta P_{tube}$ is found to be 1.25 N/m$^2$ ($9.37\times10^{-3}$ mmHg). This is negligible when compared the IOP of the human eye. The resistance $R_{tube}$ is $\Delta P_{tube}/V_a$ and is equal to $4.68\times10^{-3}$ mmHg/(µl/min).

### *E.2.2 Valve resistance*

The pressure drop across the valve formed by the leaflets of the Ahmed valve is a function of the flow rate (Fig. E.3) [Sta05]. With a flow rate of 2 µl/min, the pressure drop is reported to be about 6 mmHg. Assuming linearity, which is appropriate for flow rates from 0-3 µl/min, the resistance of the valve, $R_{valve}$, is 3 mmHg/(µl/min).

### *E.2.3 Fibrous bleb resistance*

Formation of a fibrous bleb, as explained in section 1.4.2, is a natural reaction to the implantation of a glaucoma drainage implant and forms an important component in determining

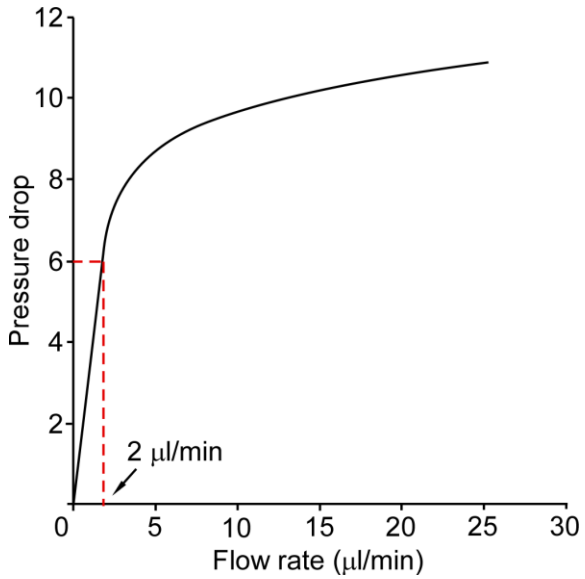


**Fig. E.3:** Pressure drop as a function of the flow rate for the valve in an AGDD [Sta05].

the final IOP. This bleb will impart a resistance to the flow of AH against the episcleral venous pressure. The flow resistance of the bleb can be estimated from experimental data of flow rate as a function of applied pressure.

The flow rates against pressures applied in the anterior chamber of the eyeball of a Molteno implant has been previously determined in monkeys [Min87]. The Molteno implant is a valveless glaucoma drainage implant where the resistance to AH outflow is generated purely through a

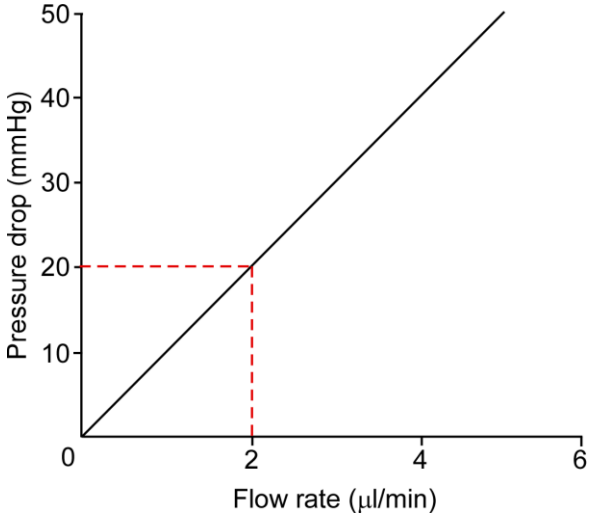


**Fig. E.4:** Pressure as a function of the flow rate for an implanted Molteno device [Min87].

fibrous bleb formed within a few weeks of the implantation. For a flow rate of 2 μl/min, the pressure drop is reported to be about 20 mmHg. Therefore, the resistance of the bleb for the Molteno implant plate is 10 mmHg/(μl/min). (Fig. E.4).

It can be assumed that resistance of the fibrous bleb is inversely proportional to the plate area. The plate area of the Molteno implant is 147 $mm^2$, while for the AGDD it is 185 $mm^2$. Correspondingly, the resistance of the bleb in an AGDD can be estimated to be approximately 8 mmHg/(μl/min). This corresponds to a pressure drop of 16 mmHg for a flow of 2 μl/min.

From the above analysis, it is clear that the valve and the fibrous bleb form the largest components of resistance to the AH outflow in an AGDD. The resistance of the fibrous bleb derived here can be used in simulation models to estimate the performance of actuators in the glaucoma drainage devices. A more complete model can also include the tube and the valve, the parameters of which can be derived using the method outlined here.

# Appendix F

## Three Dimensional Force Measurements During Rapid Palatal Expansion in *Sus scrofa*[1]

Dental implants such as palatal expanders present an application space where wireless magnetoelastic strain sensors can significantly improve current treatment methodologies. This appendix details preliminary studies on the use of conventional strain sensors to quantify the forces of expansion in a palatal expander. In the future, wireless strain sensors of the type described in Chapter 2 can be used to improve treatment outcomes of rapid palatal expansion.

### F.1 Overview

Rapid palatal expansion is a common procedure in orthodontics used to increase maxillary arch length and width by separating the maxillary bones along the midpalatal suture [Haa61]. The opening of the midpalatal suture is also accompanied by distraction of bones at other facial sutures and changes at the cranial base [Gho10, Leo10]. Generally, rapid maxillary expansion is most successful in growing children who have patent or unfused sutures. While several different designs of tooth- and bone-borne expanders are available, the most commonly used appliance is the hyrax rapid palatal expander (RPE) that is typically attached to two teeth on each side of the maxillary arch.

Although RPEs are largely thought to deliver force vectors in two rather than three dimensions – a postulate that remains to be examined – they function within a complex three-

[1] This work was performed in collaboration with Dr. Kelly Goeckner, Dr. Jeanne Nervina, and Dr. Sunil Kapila of the School of Dentistry, University of Michigan, Ann Arbor, MI.

dimensional (3D) craniofacial structure composed of a number of bones that are separated by sutures that, in turn, reside within an environment that includes active muscles and soft tissues [Ner14]. Furthermore, the RPE is attached to teeth that undergo dental movements due to the forces that also result in the modeling of bone. Together these lead to shortcomings in treatment with RPE that include dental movements as opposed to preferred skeletal movements, dental tipping, lack of optimal expansion in different areas of the palate, and the development of boney fenestrations and post-treatment relapse [Gho10, Bal09, Gar06, Gar08, Gau11, Kar10]. This complex and dynamic environment contributes to a lack of a detailed understanding of how tissues respond to RPE expansion forces and compromises the predictability of the planned treatment outcomes.

Given these complexities, many variables must be taken into account in planning treatment with an RPE. These include, but are not limited to, sutural maturation, soft tissue and/or scar tissue resistance, the magnitude and types of movement of teeth to which the RPE is anchored, the location of the RPE in all three dimensions relative to the maxilla and teeth, and expected relapse after expansion [Ner14, Har01, Sch01, Zuc13]. All of these variables would determine the magnitude and direction of forces required to obtain predictable, efficient, and stable expansion of the maxilla. Unfortunately, little is known about the precise nature of forces needed to optimally expand the palate during RPE treatment. Instead, treatment is typically rendered on the basis of the desired magnitude of expansion for each patient rather than the expected responses to the expander and regardless of the forces experienced by the maxillary structures.

In addition to measuring the total expansion force, it is critical to understand the forces generated in all three spatial dimensions ($x$, $y$ and $z$). Isaacson, *et al.*, measured maxillary expansion force in humans and concluded that there is high variability in both the expansion force

and its temporal evolution [Isa64a, Isa64b, Zim65]. However, this investigation only reported total expansion force and did not resolve the force in three dimensions. Knowing the expansion forces exerted in three dimensions with a conventional RPE will allow for custom designs and individualized treatment planning to generate optimal forces in the desired directions. Optimizing the expansion force requires knowledge of the magnitude and direction of expansion generated by the RPE specifically for each patient. This can be achieved by accurately measuring the expansion force generated by the activation of the RPE using an integrated sensor to provide the orthodontist access to real-time data for each patient, thus facilitating customized force levels and treatment modalities. Such real-time information would enable the clinician to determine whether optimal forces for sutural expansion have been achieved, the magnitude and rate of force decay following activation, and optimal timing and amount of reactivation of the appliance specific to each individual.

Specific animal models have been utilized to study and refine protocols and technology for maxillary expansion prior to utilizing these approaches on humans. *Sus scrofa* and Yucatan minipigs are often chosen as experimental models for RPE studies because their midpalatal suture anatomy and chewing patterns, and the resulting transmission of force, are similar to humans [Pap10]. Porcine bone is also physiologically and metabolically similar to human bone in terms of bone mineral density, bone mineral concentration and bone remodeling [Ste12]. When using pigs for RPE studies, the age of the pig is important because enough tooth structure must be fully erupted into the maxillary arch to stably affix the tooth-borne RPE, while still having an appropriately immature maturational status to ensure that a patent midpalatal suture that will respond favorably to expansion forces.

Although a tooth-borne RPE is expected to have the applied force manifest in three dimensions that would be expressed as a combination of dental tipping (orthodontic expansion) and sutural (skeletal) expansion along the midpalatal suture, currently no established methodology exists to assess the magnitude and breakdown of these forces. The aim of this study is to assess the feasibility of devising an appliance with sensors to facilitate the extraction of real-time information on forces in three dimensions expressed by activation of a hyrax RPE.

## F.2 Methods

### *A. Appliance Fabrication and Incorporation of Sensor*

A hyrax RPE (OrthoXPAND™ 7 mm jackscrew, Lakeville, IN) was fabricated to fit the dentition and palate of the maxilla of a freshly euthanized 5-month old *Sus scrofa* (Swine Teaching and Research Center, Michigan State University, Lansing, MI). Custom pinched bands were fitted

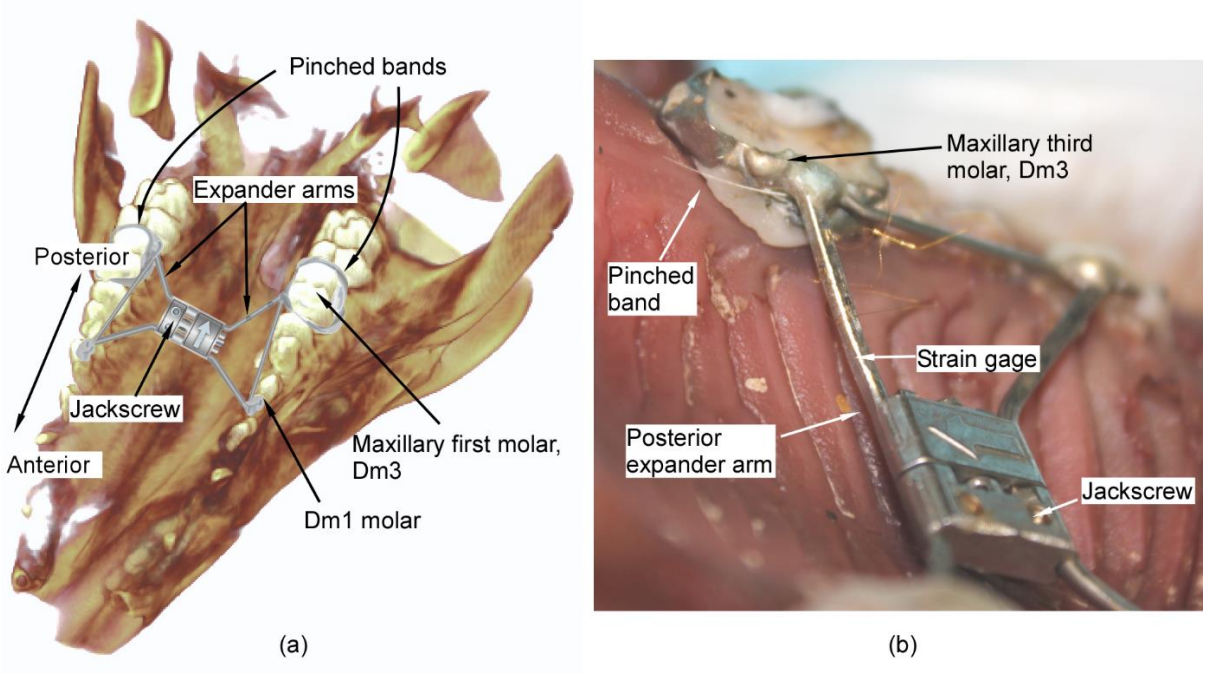


**Fig. F.1:** (a) Illustration of the hyrax-design RPE and the attachment of the expander arms superimposed on the maxillofacial structures of the pig head. (b) Location of the strain sensor attached to the posterior expander arm, prior to the use of dental composite.

on the maxillary third molars (Dm3) (Fig. F.1(a)). The bands were then soldered to the posterior arms of the RPE and to the corresponding anterior arms using a 316 stainless steel extension arm. The maxillary first molars (Dm1) molar on which the anterior arms would be typically anchored for a four-banded hyrax RPE were not banded due to inadequate eruption of these teeth. As a result, the anterior arms rested against the lingual surface of Dm1, but were not anchored to the teeth.

The posterior arm of the expander was affixed with a single axis, U-shaped p-doped silicon semiconductor strain gage (SS-018-011-3000PU, Micron instruments, Simi Valley, CA). To house the strain gage, a flat surface was machined on the arm using micro-electrodischarge machining (μEDM). The strain gage was attached using cyanoacrylate adhesive (Fig. F.1(b)) and then covered with light-cure Transbond XT (3M Unitek, Monrovia, CA) dental composite. The custom hyrax-design expander was then cemented into place using light-cure OptiBand Ultra (Ormco Corporation, Orange County, CA) dental composite. Leads were soldered to the sensors to measure resistance during expansion. The strain gage resistances were read in real-time using data acquisition device NI6341 and LabVIEW (National Instruments Corporation, Austin, TX) at a sampling rate of 10 samples/s.

The deformation of the arms under applied activation of the jackscrew was measured using a strain gage, the data from which was used to estimate the expansion forces. The relationship between the arm deformation (and consequently, the strain on the arms) and the expansion forces was determined using finite element analysis (FEA). From this relationship and the measured strain data, the expansion forces on the arms could be estimated.

The validity of this approach was first confirmed on a simple cantilever instrumented with the strain gage. The cantilever was a metal bar with $1.5 \times 5$ mm$^2$ cross section and 30 mm length.

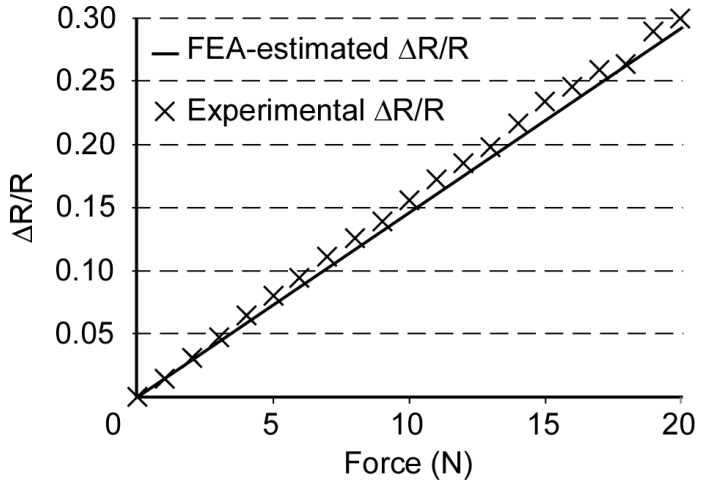


**Fig. F.2:** Comparison of experimental and FEA-estimated resistance change for an applied load on a test cantilever.

The strain gage was attached to the cantilever which was then deflected with a prescribed load. The strains the cantilever was subject to were similar to those expected in a palatal expander. The change in resistance of the strain gage was recorded under this applied load. This measured change in resistance was compared to an FEA-estimated change in resistance. COMSOL Multiphysics software was used for the FEA to simulate the strains on a fixed cantilever under an applied load. The corresponding change in resistance of the strain gage was calculated using the gage factor data provided by the manufacturer. Figure F.2 shows the experimentally measured and FEA-estimated change in resistance values. The similarity between these validates the approach. In addition, this experiment also verifies the strain gage performance and a linear response is observed for up to 30% change in resistance.

*B. Force Relationships*

In a palatal expander, the force applied to the expander arms can be resolved along three Cartesian coordinates. Building on the approach described in the previous section for the uniaxial case, the three-dimensional response is a simple superposition of these uniaxial responses. The

relationship between the strain on the posterior expander arm and the expansion forces on the arms is determined using a 3D FEA. A 3D model of the expander was created in Dassault Solidworks and imported into COMSOL Multiphysics. As illustrated in Fig. F.3(a), the expansion force acts outward axially from the central block of the expander where the jackscrew is located.

TABLE F.I: DIMENSIONS OF THE EXPANDER ARMS

| Arm number | Angle with XY plane | Angle with XZ plane | Length (mm) |
|---|---|---|---|
| 1 | 29° | 21° | 13.8 |
| 2 | 21° | 29° | 12.3 |
| 3 | 24° | 33° | 16.5 |
| 4 | 25° | 43° | 16.9 |
| Cross section (all arms) | | $1.2 \times 1.2$ mm$^2$ | |

TABLE F.2: MATERIAL PROPERTIES (316 STAINLESS STEEL)

| | |
|---|---|
| Young's modulus | 193 GPa |
| Poisson's ratio | 0.27 |
| Density | 8000 kg/m$^3$ |

The dimensions and material properties of the expander are listed in Tables F.1 and F.2. The mechanical forces and strains effected by the jackscrew in an expansion were emulated by a thermally induced expansion. In this method, which follows commonly accepted practice, an artificial temperature rise combined with an assumed expansion coefficient in the constituent material are used to mimic strain resulting from other forms of actuation that cannot be replicated in the model. The boundary conditions on the expander arms replicated the test conditions in the pig head; the posterior arms were attached to fixed supports, while the unbanded anterior arms were assumed to be unconstrained.

In the simulation model, the strain gage was attached 11 mm away from the fixed end (which is anchored to the tooth) on the sensor arm (Fig. F.3(a)). The strain along the beam axis of the sensor arm, i.e. arm 1, instrumented with the strain gage, for an arbitrary expansion is plotted in Fig. F.3(b). Figure F.3(c) shows the variation of strain along the surface of the beam as a function of the distance from the fixed anchor for an arbitrary expansion. The strain gage was attached at a location that undergoes compressive strain upon jackscrew activation. The strain

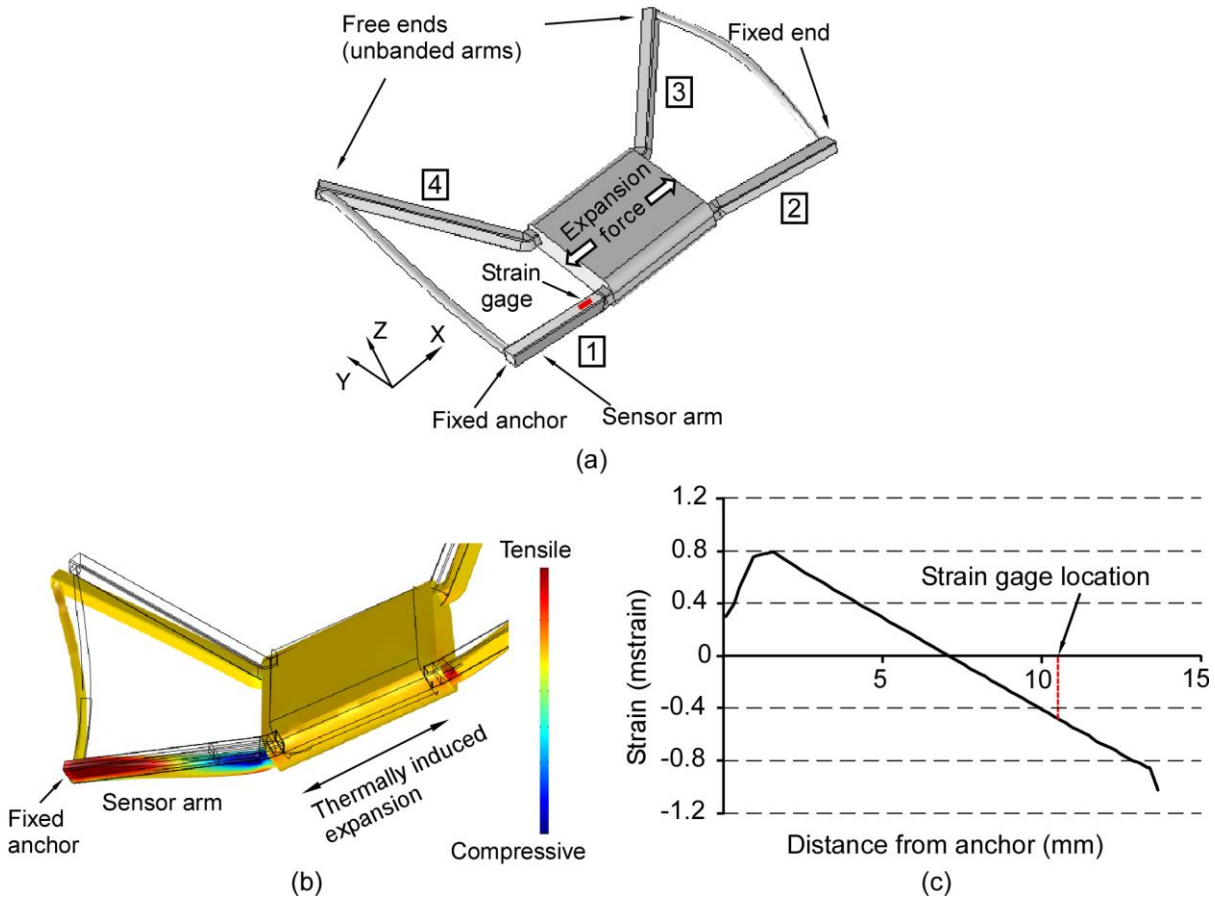


**Fig. F.3:** (a) 3D model of the expander used for FEA. The individual expander arms have been numbered. Arm 1 is instrumented with the strain gage. (b) FEA of strain along the expander arm for an arbitrary expansion. Compressive strain is observed at the location of the strain gage on the sensor arm (arm 1). (c) Strain on the top surface of the sensor arm as a function of distance from the fixed anchor.

gage was attached in the region where the strain was high, on the part of the beam which was straight and away from the bend (where it was attached to the jackscrew). The region of the beam (near the center) where the strain is estimated to be zero is avoided. Based on this simulation, the empirical relations between the magnitude of strain at the location of the sensor and the expansion forces are approximately:

$$F_{total} = 4.74 \times 10^4 \times e_{gage} \tag{F.1}$$

$$F_x = 4.72 \times 10^4 \times e_{gage} \tag{F.2}$$

$$F_y = 1.35 \times 10^2 \times e_{gage} \tag{F.3}$$

$$F_z = 3.60 \times 10^3 \times e_{gage} \quad \text{(F.4)}$$

Here, $F_{total,}$ $F_x$, $F_y$, and $F_z$ are the total force and forces along the *x*, *y* and *z* axes respectively, whereas $e_{gage}$ is the strain measured by the sensor.

Although the simulation assumed the arms to be anchored to fixed constraints, in reality, the dental tipping and skeletal expansion results in movement of these anchors as well. Hence, the expansion assumed in simulation would, in actuality, correspond to the difference between the jackscrew activation and the combined result of dental tipping and skeletal expansion.

The expander was subjected to a total of 8 quarter-turns of activation of the jackscrew over a duration of 1900 s (totaling 2.0 mm), separated by 200-300 s intervals. The activation of the RPE's jackscrew depends on the number of turns applied to it. The compression of the arms ($d_{arms}$) is the difference between the RPE's jackscrew activation ($d_{act}$) and resulting expansion ($d_{exp}$), and is reflected in the strain gage reading. The FEA yields an empirical formula for $d_{arms}$:

$$d_{arms}\,(in\,mm) = 165 \times\ e_{gage} \quad \text{(F.5)}$$

The resulting expansion for a given jackscrew activation can now be expressed as:

$$d_{exp} = d_{act} - d_{arms} \quad \text{(F.6)}$$

*C. Outcome Evaluation*

Three-dimensional imaging with cone beam computed tomography (CBCT) was used to quantify the post-expansion changes in the midpalatal suture and rebound in the dentition. CBCT was performed with 3D Accuitomo 170 (J Morita USA, Irvine, CA) on the fresh pig maxillofacial structures just after the expander was removed and again after three days of relapse. The CBCT images were captured using the following settings: 17 × 12 $cm^2$ field of view, high-fidelity (360°) scan mode, 90 kV and 5 mA for 30.8 s with a voxel size of 0.25 mm.

## F.3 Results

The expander was subjected to a total of 2 mm of activation, over a duration of 1900 s. Using LabVIEW, the strain measurements were recorded for the entire duration of the experiment. The strain measurements were translated to expansion forces using equations (1)-(4) and plotted as a function of time (Fig. F.4).

Figure F.4(a) shows the total force ($F_{total}$) and $F_x$, which is the expansion force in the transverse dimension across the midpalatal suture. This figure confirms that $F_x$ is the overwhelming contributor to the total expansion force, and the two are indistinguishable in the plot. In each quarter-turn, $F_x$ first spikes by an average of 34 N and then reduces by an average of 24 N in the 200-300 s interval between turns. At the end of the activation sequence, $F_x$ builds up to a peak of 98 N. In contrast to $F_x$, $F_y$ and $F_z$ are the expansion forces in the anterior-posterior dimension and the vertical dimension, respectively. These forces are much smaller than $F_x$, with $F_z$ peaking at 7 N (Fig. F.4(b)). Force $F_y$ is negligibly small because the anterior arms of the expander are not anchored.

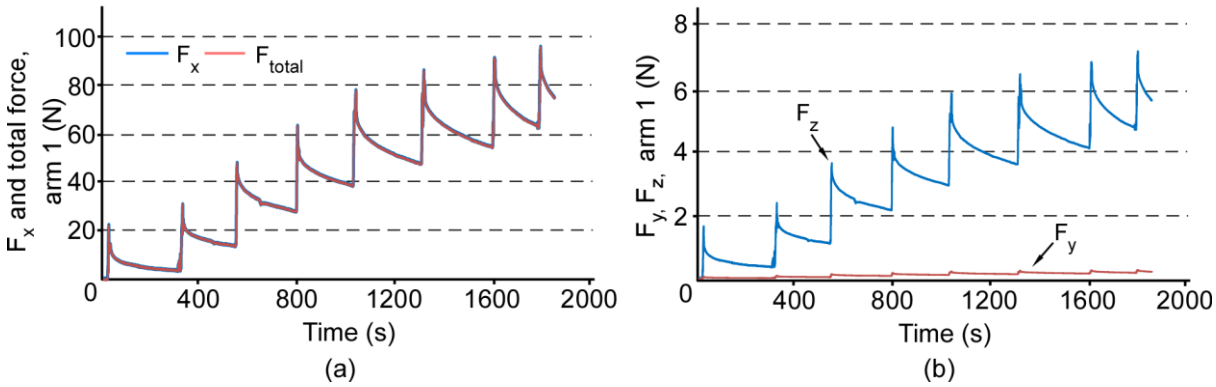


**Fig. F.4:** (a) Total force ($F_{total}$) and force along $x$ axis ($F_x$), and (b) $F_y$ and $F_z$ on the sensor arm (arm 1) for a total of eight turns of the jackscrew. $F_x$ is dominant component of the total force and $F_y$ is negligibly small.

The resulting expansion, $d_{exp}$, is determined using the strain gage readings and equations (5) and (6) (Fig. F.5). Almost 85% of the activation is immediately transferred to the palate and teeth.

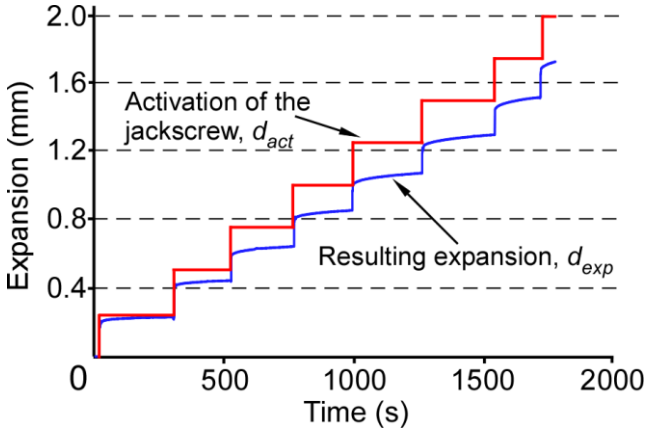


**Fig. F.5:** Comparison of the activation of the jackscrew ($d_{act}$) and resulting expansion ($d_{exp}$) as a function of time for eight turns of the jackscrew (2.0 mm total activation).

A comparison of the suture at the level of the palate immediately after removal of the RPE and three days post-removal is presented in Fig. F.6(a). These two axial slices from the different time points are superimposed in Fig. F.6(b) using a regional superimposition of the maxilla. As evident from the lack of suture closure in the three day time period, there was little skeletal relapse. This is consistent with the non-responsive nature of the fresh carcass. Although the skeletal relapse is negligible, the dental relapse is evident. As shown in Fig. F.6(c), this varies from 0.4 mm at the third molar to 0.82 mm at the first.

## F.4 Discussion

The acute activation of the expander accounts for the high force (almost 100 N) observed in the experiments. Generally, 24 hours is prescribed between activations of one quarter-turn or 0.25 mm of expansion of the expander. This is in contrast to the 200-300 s delays in our experiment. The total force of this experiment cannot be directly compared with that of Isaacson *et al*. [Isa64b] because of the differing species and experimental methods. However, the rapid rise

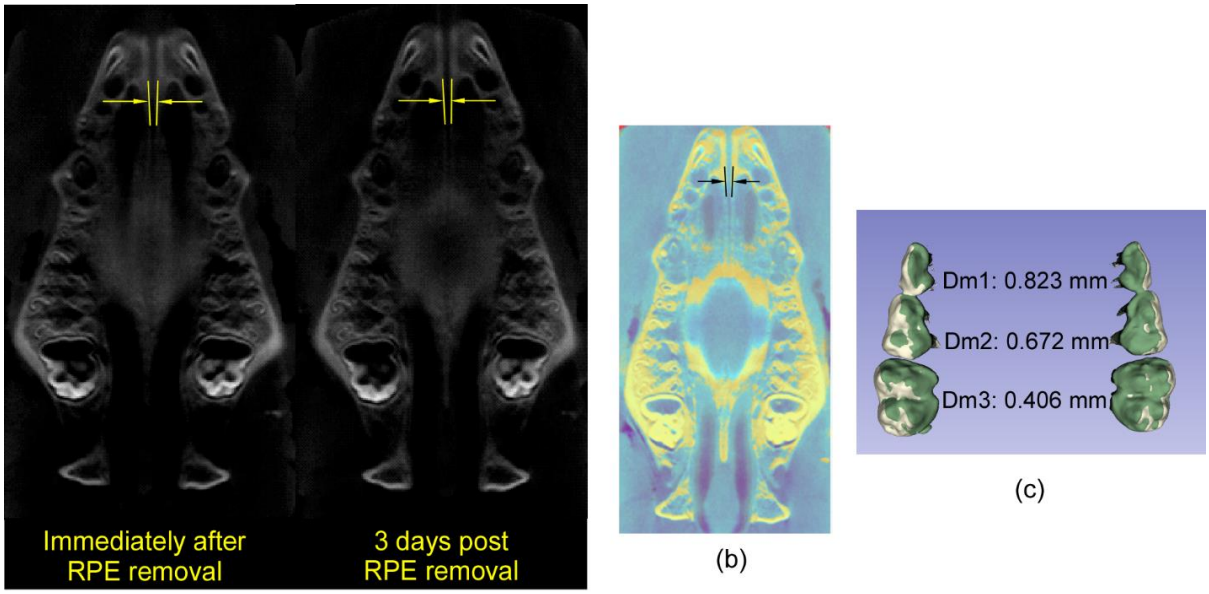


**Fig. F.6:** (a) Axial slices of CBCT images obtained immediately after RPE removal (left) and after three days of relapse (right) showing sutural separation demarcated by lines and yellow arrows). (b) Generalized superimposition of the palate immediately after RPE removal (cyan) and after three days of relapse (yellow) showing minimal changes in midpalatal suture separation. (c) Generalized superimposition of the maxillary dentition immediately after RPE removal (white) and after three days of relapse (green) showing the magnitude of relapse at the first (Dm1); second (Dm2) and third (Dm3) molars.

in force levels with a non-linear decay pattern is consistent with previous findings. Since this was a proof of concept study, the interval between activations and the high magnitude of forces of the experimental time frame was considered less critical to the analyses than determining the expression of forces in three dimensions.

As evident from Fig. F.5, a portion of the given activation of the jackscrew results in immediate expansion which is then followed by a gradual increase in the expansion. Consequently, the difference between the applied activation and resulting expansion progressively decreases in the time intervals following an activation. An interval of sufficient duration will permit the expansion to plateau before the next activation.

The dental relapse observed in Fig. F.6(c) shows that dental tipping is a component of total expansion, in addition to the skeletal expansion, confirming previous observations [Gho10, Gar08, Kar10]. This is expected as the RPE used is a tooth-borne device. Taken together, the sutural patency and dental rebound demonstrate that resistance to expansion offered by skeletal and periodontal tissues contribute to the total expansion force.

From a clinical perspective, these results represent a significant step toward detailing the force distributions of a conventional tooth-borne RPE. From an engineering perspective, the results demonstrate a means of measuring the transactivation force of a RPE *in situ* and the resulting expansion. Taken together, these findings provide the basis for further development of smart orthodontic appliances that provide real-time readouts of forces and movements, which will allow personalized, optimal treatment for the first time.

## F.5 Summary

This work describes the first real-time quantitative measurements of three-dimensional forces associated with RPE in all three planes of space. This is accomplished using a single sensor, which minimizes the challenge of sensor integration and electronic read-out. The simulation itself can be expanded to include a complete 3D model of the skull and variations in the type of expander used to predict the treatment outcomes for a given expansion protocol. Real-time force measurement during the treatment can then be used to track the patient response and modify the protocol, if needed. In a broader sense, this work develops the methodology and establishes a proof of concept towards achieving the basic foundations needed for our longer-term goal of developing customized expanders whose activation can be individualized both in magnitude and direction for each patient.

A complete force measurement system for this application would include a wireless readout circuit. Alternatively, a passive strain sensing solution of the type described in Chapter 2 can be devised. Fully integrated wireless sensing systems with packaging for compatibility and sterilization have been previously developed for other applications [Che11]. Biocompatibility of the transducer can be enhanced by coating it with Parylene – a biocompatible polymer [Loe77].

Commercially available expanders also include bone-anchored RPEs, which eliminate the dental movement component of expansion seen with tooth-borne RPEs. Future studies will include determination of forces and movements generated with these devices without the complexities of dental movements. Future research will also include *in vivo* testing incorporating CBCT imaging before, immediately after and post-expansion with a longer decay interval between expander activations to better simulate human biological responses to expansion forces.

## REFERENCES


[Ada05] F. A. Adatia and K. F. Damji, "Chronic open-angle glaucoma. Review for primary care physicians," *Can. Fam. Physician*, vol. 51, pp. 1229–37, Sep. 2005.

[Aga95] M. Agarwala, D. Bourell, J. Beaman, H. Marcus, and J. Barlow, "Direct selective laser sintering of metals," *Rapid Prototyp. J.*, vol. 1, no. 1, pp. 26–36, 1995.

[All05] M. G. Allen, "Micromachined endovascularly-implantable wireless aneurysm pressure sensors: from concept to clinic*," The 13th International Conference on Solid-State Sensors, Actuators and Microsystems, 2005. Digest of Technical Papers. TRANSDUCERS '05*, 2005, vol. 1, pp. 275–278.

[Amo06] A. Ben Amor, T. Budde, and H. H. Gatzen, "A magnetoelastic microtransformer-based microstrain gauge," *Sensors Actuators A Phys.*, vol. 129, no. 1–2, pp. 41–44, May 2006.

[And82] P. M. Anderson III, "Magnetomechanical coupling, ΔE effect, and permeability in FeSiB and FeNiMoB alloys," *J. Appl. Phys.*, vol. 53, no. 11, p. 8101, 1982.

[And85] P. M. Anderson, III, G. R. Bretts, and J. E. Kearney, "Surveillance system having magnetomechanical marker," United States patent 4510489, 1985.

[Arm90] J. C. Armour, J. Y. Lucisano, B. D. McKean, and D. A. Gough, "Application of chronic intravascular blood glucose sensor in dogs," *Diabetes*, vol. 39, no. 12, pp. 1519–26, Dec. 1990.

[Arn00] Arnold Magnetic Technologies Corporation, "Rolled Products Strip & Foil Catalogs & Literature." [Online]. Available: http://www.arnoldmagnetics.com/Thin_Gauge_Strip_and_Foil_Literature.aspx. Accessed: Oct 12, 2015

[Ayy98] R. S. Ayyala, D. Zurakowski, J. A. Smith, R. Monshizadeh, P. A. Netland, D. W. Richards, and W. E. Layden, "A clinical study of the Ahmed glaucoma valve implant in advanced glaucoma," *Ophthalmology*, vol. 105, no. 10, pp. 1968–1976, 1998.

[Ayy99] R. S. Ayyala, L. E. Harman, B. Michelini-Norris, L. E. Ondrovic, E. Haller, C. E. Margo, and S. X. Stevens, "Comparison of different biomaterials for glaucoma drainage devices," *Arch. Ophthalmol.*, vol. 117, no. 2, pp. 233–6, Feb. 1999.

[Ayy00] R. S. Ayyala, B. Michelini-Norris, A. Flores, E. Haller, and C. E. Margo, "Comparison of different biomaterials for glaucoma drainage devices: Part 2.," *Arch. Ophthalmol.*, vol. 118, no. 8, pp. 1081–4, Aug. 2000.

[Bal09] F. Ballanti, R. Lione, E. Fanucci, L. Franchi, T. Baccetti, and P. Cozza, "Immediate and post-retention effects of rapid maxillary expansion investigated by computed tomography in growing patients," *Angle Orthod.*, vol. 79, pp. 24–29, 2009.

[Bar00] J. M. Barandiaran, J. Gutierrez, and C. Gómez-Polo, "New sensors based on the magnetoelastic resonance of metallic glasses," *Sensors Actuators A Phys.*, vol. 81, no. 1–3, pp. 154–157, Apr. 2000.

[Ber76] B. S. Berry and W. C. Pritchet, "Magnetoelastic Phenomena in Amorphous Alloys," *AIP Conf. Proc.*, vol. 292, no. 1, pp. 292–297, 1976.

[Ber88] G. Bergmann, F. Graichen, J. Siraky, H. Jendrzynski, and A. Rohlmann, "Multichannel strain gauge telemetry for orthopaedic implants," *J. Biomech.*, vol. 21, no. 2, pp. 169–176, Jan. 1988.

[Bhu14] A. K. Bhunia, M. S. Kim, and C. R. Taitt, Eds., *High Throughput Screening for Food Safety Assessment*. Amsterdam: Elsevier B.V., 2014, p. 370.

[Boy09] J. W. Boyle and P. A. Netland, "Surgical Technique 3 (Ahmed Glaucoma Valve Drainage Implant)," Glaucoma Volume 2: Surgical Management, C, T. M. Shaarawy, M. B. Sherwood, R. A. Hitchings, and J. G. Crowston, Eds., Amsterdam: Elsevier B.V., 2009, pp. 425–435.

[Boz93] R. M. Bozorth, "Stress and Magnetostriction," Ferromagnetism, New York: IEEE Press, 1993, p. 684.

[Bra97] E. T. Den Braber, J. E. De Ruijter, and J. A. Jansen, "The effect of a subcutaneous silicone rubber implant with shallow surface microgrooves on the surrounding tissues in rabbits," *J. Biomed. Mater. Res.*, vol. 37, no. 4, pp. 539–547, 1997.

[Bro79] M. Brouha and J. van der Borst, "The effect of annealing conditions on the magneto-mechanical properties of Fe-B-Si amorphous ribbons," *J. Appl. Phys.*, vol. 50, no. B11, p. 7594, 1979.

[Bur00] F. Burny, M. Donkerwolcke, F. Moulart, R. Bourgois, R. Puers, K. Van Schuylenbergh, M. Barbosa, O. Paiva, F. Rodes, J. B. Bégueret, and P. Lawes, "Concept, design and fabrication of smart orthopedic implants," *Med. Eng. Phys.*, vol. 22, no. 7, pp. 469–479, 2000.

[Cai68] J. E. Cairns, "Trabeculectomy. Preliminary report of a new method," *Am. J. Ophthalmol.*, vol. 66, no. 4, pp. 673–9, Oct. 1968.

[Cam88] J. D. Cameron and T. C. White, "Clinico-histopathological correlation of a successful glaucoma shunt implant," *Ophthalmology*, vol. 95, no. 9, pp. 1189–1194, 1988.

[Che05] D.-X. Chen, E. Pardo, and A. Sanchez, "Demagnetizing factors for rectangular prisms," *IEEE Trans. Magn.*, vol. 41, no. 6, pp. 2077–2088, Jun. 2005.

[Che11] G. Chen, H. Ghaed, R. Haque, M. Wieckowski, Y. Kim, G. Kim, D. Fick, D. Kim, M. Seok, K. Wise, D. Blaauw, and D. Sylvester, "A Cubic-Millimeter Energy-Autonomous Wireless Intraocular Pressure Monitor," *International Solid-State Circuits Conference, 2011*, pp. 138–139.

[Cho10] L. Choritz, K. Koynov, G. Renieri, K. Barton, N. Pfeiffer, and H. Thieme, "Surface topographies of glaucoma drainage devices and their influence on human tenon fibroblast adhesion," *Invest. Ophthalmol. Vis. Sci.*, vol. 51, no. 8, pp. 4047–53, Aug. 2010.

[Chu02] P. Chu, "Plasma-surface modification of biomaterials," *Mater. Sci. Eng. R Reports*, vol. 36, no. 5–6, pp. 143–206, 2002.

[Chu05] J. Chuang, D. J. Thomson, and G. E. Bridges, "Embeddable wireless strain sensor based on resonant RF cavities," Rev. Sci. Instrum., vol. 76, no. 9, p. 094703, 2005.

[Cla80] A. E. Clark, "Magnetostrictive rare-earth Fe2 compounds," Ferromagnetic Materials, Volume 1, E.P. Wohlfarth,Ed., Amsterdam: North-Holland, 1980, p. 577.

[Cla97] F. Claeyssen, N. Lhermet, R. Le Letty, and P. Bouchilloux, "Actuators, transducers and motors based on giant magnetostrictive materials," *J. Alloys Compd.*, vol. 258, no. 1–2, pp. 61–73, Aug. 1997.

[Col67] C. C. Collins, "Miniature passive pressure transensor for implanting in the eye," *IEEE Trans. Biomed. Eng.*, vol. BME-14, no. 2, pp. 74–83, Apr. 1967.

[Col13] A. E. Colvin and H. Jiang, "Increased in vivo stability and functional lifetime of an implantable glucose sensor through platinum catalysis," *J. Biomed. Mater. Res. A*, vol. 101, no. 5, pp. 1274–82, May 2013.

[Cos04] V. P. Costa, A. Azuara-Blanco, P. A. Netland, M. R. Lesk, and E. S. Arcieri, "Efficacy and safety of adjunctive mitomycin C during Ahmed Glaucoma Valve implantation: a prospective randomized clinical trial," *Ophthalmology*, vol. 111, no. 6, pp. 1071–6, Jun. 2004.

[Cox12] R. Cox, F. Josse, S. M. Heinrich, O. Brand, and I. Dufour, "Characteristics of laterally vibrating resonant microcantilevers in viscous liquid media," *J. Appl. Phys.*, vol. 111, no. 1, 2012.

[Cul09a] B. D. Cullity and C. D. Graham, "Magnetostriction and the effects of stress," Introduction to Magnetic Materials, New York: IEEE Press, 2009, pp. 241–272.

[Cul09b] B. D. Cullity and C. D. Graham, "Experimental methods," Introduction to Magnetic Materials, New York: IEEE Press, 2009, pp. 23–86.

[Cul09c] B. D. Cullity and C. D. Graham, "Hard magnetic materials," Introduction to Magnetic Materials, New York: IEEE Press, 2009, pp. 477–504.

[Cur12] J. T. Curran, G. Lachapelle, and C. C. Murphy, "Improving the design of frequency lock loops for GNSS receivers," *IEEE Trans. Aerosp. Electron. Syst.*, vol. 48, no. 1, pp. 850–868, 2012.

[D'Li05] D. D. D'Lima, C. P. Townsend, S. W. Arms, B. A. Morris, and C. W. Colwell, "An implantable telemetry device to measure intra-articular tibial forces," *J. Biomech.*, vol. 38, no. 2, pp. 299–304, Feb. 2005.

[Dar01] C. M. Darvennes and S. J. Pardue, "Boundary effect of a viscous fluid on a longitudinally vibrating bar: Theory and application," *J. Acoust. Soc. Am.*, vol. 110, no. 1, p. 216, 2001.

[Dea13] R. N. Dean and A. K. Rane, "A digital frequency-locked loop system for capacitance measurement," *IEEE Trans. Instrum. Meas.*, vol. 62, no. 4, pp. 777–784, 2013.

[DeC98] N. DeCristofaro, "Amorphous Metals in Electric-Power Distribution Applications," *MRS Bull.*, vol. 23, no. 5, pp. 50–56, 1998.

[Dem01] M. F. Dempsey and B. Condon, "Thermal injuries associated with MRI," *Clin. Radiol.*, vol. 56, no. 6, pp. 457–65, Jun. 2001.

[Des10] S. Deshmukh and H. Huang, "Wireless interrogation of passive antenna sensors," *Meas. Sci. Technol.*, vol. 21, no. 3, p. 035201, Mar. 2010.

[Dob82] H. S. Dobbs, "Fracture of titanium orthopaedic implants," *J. Mater. Sci.*, vol. 17, no. 8, pp. 2398–2404, 1982.

[Dow05] P. R. Downey and A. B. Flatau, "Magnetoelastic bending of Galfenol for sensor applications," *J. Appl. Phys.*, vol. 97, no. 10, p. 10R505, 2005.

[Eib05] M. Eibschitz-Tsimhoni, R. M. Schertzer, D. C. Musch, and S. E. Moroi, "Incidence and management of encapsulated cysts following Ahmed glaucoma valve insertion," J. *Glaucoma*, vol. 14, no. 4, pp. 276–9, Aug. 2005.

[Eng00] G. Engdahl, Handbook of Giant Magnetostrictive Materials. San Diego, CA: Academic Press, 2000.

[Eps59] E. Epstein, "Fibrosing response to aqueous: Its relation to glaucoma," *Br. J. Ophthalmol.*, vol. 43, no. 11, pp. 641–647, 1959.

[Erc08] A. Ercuta, "Magnetomechanical damping in stress-relieved Ni: the effect of the dc magnetic field," *J. Phys. Condens. Matter*, vol. 20, no. 32, p. 325227, 2008.

[Ess04] D. W. Esson, "Expression of Connective Tissue Growth Factor after Glaucoma Filtration Surgery in a Rabbit Model," *Invest. Ophthalmol. Vis. Sci.*, vol. 45, no. 2, pp. 485–491, Feb. 2004.

[Etr00] Etrema Products Inc., "Terfenol-D data sheet" [Online]. Available: http://www.etrema.com/terfenol-d. Accessed: Oct 12, 2015

[Eva09] A. Evans, S. Chiravuri, and Y. Gianchandani "Transdermal power transfer for recharging implanted drug delivery devices via the refill port," *Biomed. Microdevices*, vol. 12, no. 2, pp. 179–185, 2010.

[FDA14] Food and Drug Administration, “Criteria for Significant Risk Investigations of Magnetic Resonance Diagnostic Devices Guidance for Industry and Food and Drug Administration Staff Public Comment,” 2014.

[Fle89] W. J. Fleming, “Magnetostrictive torque sensor performance – nonlinear analysis,” *IEEE Trans. Veh. Technol.*, vol. 38, no. 3, pp. 159–167, 1989.

[Frie89] H. Friedman, “Photochemical machining,” ASM Handbook, Volume 16: Machining, ASM International, 1989, pp. 587–593.

[Fuj83] H. Fujimori, “Magnetic anisotropy,” Amorphous Metallic Alloys, London: Butterworths, 1983, pp. 300–316.

[Gar06] D. G. Garib, J. F. C. Henriques, G. Janson, M. R. de Freitas, and A. Y. Fernandes, “Periodontal effects of rapid maxillary expansion with tooth-tissue-borne and tooth-borne expanders: A computed tomography evaluation,” *Am. J. Orthod. Dentofac. Orthop.*, vol. 129, pp. 749–758, 2006.

[Gar08] B. J. Garrett, J. M. Caruso, K. Rungcharassaeng, J. R. Farrage, J. S. Kim, and G. D. Taylor, “Skeletal effects to the maxilla after rapid maxillary expansion assessed with cone-beam computed tomography,” *Am. J. Orthod. Dentofac. Orthop.*, vol. 134, no. 1, pp. 8–9, 2008.

[Gau11] C. Gauthier, R. Voyer, M. Paquette, P. Rompré, and A. Papadakis, “Periodontal effects of surgically assisted rapid palatal expansion evaluated clinically and with cone-beam computerized tomography: 6-month preliminary results,” *Am. J. Orthod. Dentofac. Orthop.*, vol. 139, pp. S117–S128, 2011.

[Ged07] S. J. Gedde, J. C. Schiffman, W. J. Feuer, L. W. Herndon, J. D. Brandt, and D. L. Budenz, “Treatment outcomes in the tube versus trabeculectomy study after one year of follow-up,” *Am. J. Ophthalmol.*, vol. 143, no. 1, pp. 9–22, Jan. 2007.

[Ger00] R. Germano, G. Ausanio, V. Iannotti, L. Lanotte, and C. Luponio, “Direct magnetostriction and magnetoelastic wave amplitude to measure a linear displacement,” *Sensors Actuators A Phys.*, vol. 81, no. 1–3, pp. 134–136, Apr. 2000.

[Gho07] M. Ghovanloo and S. Atluri, “A Wide-Band Power-Efficient Inductive Wireless Link for Implantable Microelectronic Devices Using Multiple Carriers,” *IEEE Trans. Circuits Syst. I Regul. Pap.*, vol. 54, no. 10, pp. 2211–2221, 2007.

[Gho10] A. Ghoneima, E. Abdel-Fattah, F. Eraso, D. Fardo, K. Kula, and J. Hartsfield, “Skeletal and dental changes after rapid maxillary expansion: a computed tomography study,” *Aust. Orthod. J.*, vol. 26, pp. 141–148, 2010.

[Gol99] J. H. Goldie, M. J. Gerver, J. Oleksy, G. P. Carman, and T. A. Duenas, “Composite Terfenol-D Sonar Transducers,” *Proc. SPIE 3675, Smart Structures and Materials 1999: Smart Materials Technologies, 1999*, vol. 3675, no. March, pp. 223–234.

[Gra75] K. F. Graff, “Longitudinal waves in thin rods,” Wave Motion in Elastic Solids, Mineola, New York: Dover Publications, 1975, pp. 75–107.

[Gra09] M. Graefe, T. Goettsche, P. Osypka, K. Trieu, H. Fassbender, W. Mokwa, U. Urban, T. Hilbel, R. Becker, W. Coenen, and R. Glocker, “HYPER-IMS: A Fully Implantable Blood Pressure Sensor for Hypertensive Patients,” *SENSOR+TEST Conference, 2009*, vol. 7, pp. 145–149.

[Gre91] W. Greatbatch and C. F. Holmes, “History of implantable devices.,” *IEEE Eng. Med. Biol. Mag.*, vol. 10, no. 3, pp. 38–41, Jan. 1991.

[Gre09a] S. R. Green and Y. B. Gianchandani, “Wireless Magnetoelastic Monitoring of Biliary Stents,” *J. Microelectromechanical Syst.*, vol. 18, no. 1, pp. 64–78, 2009.

[Gre09b] S. R. Green, “Wireless Magnetoelastic Monitoring of Biliary Stents,” Ph.D. dissertation, University of Michigan, Ann Arbor, MI, 2009.

[Gre10] S. R. Green and Y. B. Gianchandani, “Tailored magnetoelastic sensor geometry for advanced functionality in wireless biliary stent monitoring systems,” *J. Micromechanics Microengineering*, vol. 20, no. 7, p. 075040, Jul. 2010.

[Gre13] S. R. Green, R. S. Kwon, G. H. Elta, and Y. B. Gianchandani, “In vivo and in situ evaluation of a wireless magnetoelastic sensor array for plastic biliary stent monitoring,” *Biomed. Microdevices*, vol. 15, no. 3, pp. 509–517, 2013.

[Gri11] C. A. Grimes, S. C. Roy, S. Rani, and Q. Cai, “Theory, instrumentation and applications of magnetoelastic resonance sensors: a review,” *Sensors*, vol. 11, no. 3, pp. 2809–44, Jan. 2011.

[Gut13] J. Gutiérrez, A. Lasheras, J. M. Barandiarán, J. L. Vilas, and M. S. Sebastián, “Improving the magnetoelectric response of laminates containing high temperature piezopolymers,” *IEEE Trans. Magn.*, vol. 49, no. 1, pp. 42–45, 2013.

[Haa61] A. J. Haas, “Rapid expansion of the maxillary dental arch and nasal cavity by opening the midpalatal suture,” *Angle Orthod.*, vol. 31, no. 2, pp. 73–90, 1961.

[Har01] J. E. Harrison and D. Ashby, “Orthodontic treatment for posterior crossbites.,” *Cochrane Database Syst. Rev.*, p. CD000979, 2001.

[Has78] R. Hasegawa, M. C. Narasimhan, and N. DeCristofaro, “A high permeability Fe-Ni base glassy alloy containing Mo,” *J. Appl. Phys.*, vol. 49, no. 3, p. 1712, 1978.

[Hau78] G. Hausch and E. Török, “Elastic, magnetoelastic, and thermal properties of some ferromagnetic metallic glasses,” *Phys. Status Solidi*, vol. 50, no. 1, pp. 159–164, Nov. 1978.

[Hay85] C. E. Hayes, W. A. Edelstein, J. F. Schenck, O. M. Mueller, and M. Eash, “An efficient, highly homogeneous radiofrequency coil for whole-body NMR imaging at 1.5 T,” *J. Mag. Resonance*, vol. 628, pp. 622–628, 1985.

[Haz06] Z. Hazan, J. Zumeris, H. Jacob, H. Raskin, G. Kratysh, M. Vishnia, N. Dror, T. Barliya, M. Mandel, and G. Lavie, "Effective prevention of microbial biofilm formation on medical devices by low-energy surface acoustic waves," *Antimicrob. Agents Chemother.*, vol. 50, no. 12, pp. 4144–52, Dec. 2006.

[Her81] J. Herschler, "The inhibitory factor in aqueous humor," *Vision Res.*, vol. 21, no. 1, p. 1981, 1981.

[Her01] A. Hernando, E. Pina, E. Burgos, C. Prados, and J. M. Gonza, "Magnetoelastic sensor as a probe for muscular activity: an in vivo experiment," *Sensors and Actuators A Phys.*, vol. 91, pp. 99–102, 2001.

[Her03] G. Herzer, "Magnetic materials for electronic article surveillance," *J. Magn. Magn. Mater.*, vol. 254–255, pp. 598–602, Jan. 2003.

[Hey01] J. J. Heys, V. H. Barocas, and M. J. Taravella, "Modeling passive mechanical interaction between aqueous humor and iris," *J. Biomech. Eng.*, vol. 123, no. 6, p. 540, 2001.

[Hol10] M. J. Holmes, N. G. Parker, and M. J. W. Povey, "Temperature dependence of bulk viscosity in water using acoustic spectroscopy," *J. Phys.: Conf. Ser.*, vol. 012011, p. 7, 2010.

[Hon93] T. Honda, Y. Hayashi, K. I. Arai, K. Ishiyama, and M. Yamaguchi, "Magnetostriction of sputtered Sm-Fe thin films," *IEEE Trans. Magn.*, vol. 29, no. 6, pp. 3126–3128, 1993.

[Hon94] T. Honda, K. I. Arai, and M. Yamaguchi, "Fabrication of actuators using magnetostrictive thin films," *Proceedings of IEEE Micro Electro Mechanical Systems: An Investigation of Micro Structures, Sensors, Actuators, Machines and Robotic Systems, 1994*, pp. 51–56.

[Hon05] C.-H. Hong, A. Arosemena, D. Zurakowski, and R. S. Ayyala, "Glaucoma drainage devices: a systematic literature review and current controversies," *Surv. Ophthalmol.*, vol. 50, no. 1, pp. 48–60, 2005.

[Hua11] K. Huang and D. D. Wentzloff, "A 60 GHz antenna-referenced frequency-locked loop in 0.13 μm CMOS for wireless sensor networks," *IEEE J. Solid-State Circuits*, vol. 46, no. 12, pp. 2956–2965, Dec. 2011.

[Hub12] T. Huber, B. Bergmair, C. Vogler, F. Bruckner, G. Hrkac, and D. Suess, "Magnetoelastic resonance sensor for remote strain measurements," *Appl. Phys. Lett.*, vol. 101, no. 4, 2012.

[Hug72] A. N. Hughes and B. A. Jordan, "Metallurgical observations on some metallic surgical implants which failed *in vivo*," *J. Biomed. Mater. Res.*, vol. 6, no. 2, pp. 33–48, 1972.

[IEC10] International Electrotechnical Commission, "Medical Electrical Equipment—Part 2-33: Particular Requirements for the Basic Safety and Essential Performance of MR Equipment for Medical Diagnosis," 2010.

[IEE91] Institute of Electrical and Electronics Engineers, “IEEE Standard on Magnetostrictive Materials: Piezomagnetic Nomenclature,” 1991.

[Isa64a] R. J. Isaacson, J. L. Wood, and A. H. Ingram, “Forces produced by rapid maxillary expansion I. Design of the force measuring system,” *Angle Orthod.*, vol. 34, no. 4, pp. 256–260, 1964.

[Isa64b] R. J. Isaacson, J. L. Wood, and A. H. Ingram, “Forces produced by rapid maxillary expansion II. Forces present during treatment,” *Angle Orthod.*, vol. 34, no. 4, pp. 261–270, 1964.

[Ito11] Y. Ito, T. Kimura, Y. Ago, K. Nam, K. Hiraku, K. Miyazaki, T. Masuzawa, and A. Kishida, “Nano-vibration effect on cell adhesion and its shape,” *Biomed. Mater. Eng.*, vol. 21, no. 3, pp. 149–58, Jan. 2011.

[Jai01] M. K. Jain, Q. Cai, and C. A. Grimes, “A wireless micro-sensor for simultaneous measurement of pH, temperature, and pressure,” *Smart Mater. Struct.*, vol. 10, no. 2, pp. 347–353, Apr. 2001.

[Jan13] S.-D. Jang, B.-W. Kang, and J. Kim, “Frequency selective surface based passive wireless sensor for structural health monitoring,” *Smart Mater. Struct.*, vol. 22, no. 2, p. 025002, Feb. 2013.

[Jen12] C. Jensen, L. Gurevich, A. Patriciu, J. J. Struijk, V. Zachar, and C. P. Pennisi, “Increased connective tissue attachment to silicone implants by a water vapor plasma treatment,” *J. Biomed. Mater. Res. Part A*, vol. 100A, no. 12, pp. 3400–3407, 2012.

[Jia06] Y. Jia, K. Sun, F. J. Agosto, and M. T. Quiñones, “Design and characterization of a passive wireless strain sensor,” *Meas. Sci. Technol.*, vol. 17, no. 11, pp. 2869–2876, Nov. 2006.

[Joh88] J. Johnston, S. Reich, A. Bailey, and J. Sluetz, “Shiley INFUSAID Pump technology.,” *Ann. N. Y. Acad. Sci.*, vol. 531, pp. 57–65, Jan. 1988.

[Joh08] M. L. Johnson, J. Wan, S. Huang, Z. Cheng, V. A. Petrenko, D.-J. Kim, I.-H. Chen, J. M. Barbaree, J. W. Hong, and B. A. Chin, “A wireless biosensor using microfabricated phage-interfaced magnetoelastic particles,” *Sensors Actuators A Phys.*, vol. 144, no. 1, pp. 38–47, May 2008.

[Joy07] J. Joy, J. Kroh, M. Ellis, M. Allen, and W. Pyle, “Communicating with implanted wireless sensor,” United States patent 7245117, 2007.

[Kar00] W. J. Karl, A. L. Powell, R. Watts, M. R. J. Gibbs, and C. R. Whitehouse, “A micromachined magnetostrictive pressure sensor using magneto-optical interrogation,” *Sensors Actuators A Phys.*, vol. 81, no. 1–3, pp. 137–141, Apr. 2000.

[Kar10] A. Kartalian, E. Gohl, M. Adamian, and R. Enciso, “Cone-beam computerized tomography evaluation of the maxillary dentoskeletal complex after rapid palatal expansion,” *Am. J. Orthod. Dentofac. Orthop.*, vol. 138, pp. 486–492, 2010.

[Kat59] H. W. Katz, Ed., “Electrostrictive and Magnetostrictive Systems,” Solid State Magnetic and Dielectric Devices, New York: John Wiley and Sons, 1959.

[Kes78] J. Kestin, M. Sokolov, and W.A. Wakeham, “Viscosity of liquid water in the range -8 °C to 150 °C,” *J. Phys. Chem. Ref. Data*, vol. 7, no. 3, p. 941, 1978.

[Kha11] W. Khalil, S. Shashidharan, T. Copani, S. Chakraborty, S. Kiaei, and B. Bakkaloglu, “A 700-µA 405-MHz all-digital fractional-N frequency-locked loop for ISM band applications,” *IEEE Trans. Microw. Theory Tech.*, vol. 59, no. 5, pp. 1319–1326, 2011.

[Kim96] C. K. Kim and R. C. O’Handley, “Development of a magnetoelastic resonant sensor using iron-rich, nonzero magnetostrictive amorphous alloys,” *Metall. Mater. Trans. A*, vol. 27, no. 10, pp. 3203–3213, 1996.

[Kim99] M. H. Kim, K. S. Lee, and S. H. Lim, “Magnetostriction measurements of metallic glass ribbon by fiber-optic Mach–Zehnder interferometry,” *J. Magn. Magn. Mater.*, vol. 191, no. 1–2, pp. 107–112, Jan. 1999.

[Kla09] O. Klaus and Z. Bernhard, “A novel magneto–elastic force sensor design based on Terfenol–D,” *SENSOR+TEST Conference 2009*, 2009, pp. 77–82.

[Kle60] W. Klement, R. H. Willens, and P. Duwez, “Non-crystalline Structure in Solidified Gold–Silicon Alloys,” *Nature*, vol. 187, no. 4740, pp. 869–870, Sep. 1960.

[Ko77] W. H. Ko, S. P. Liang, and C. D. Fung, “Design of radio-frequency powered coils for implant instruments,” *Med. Biol. Eng. Comput.*, vol. 15, no. 6, pp. 634–40, Nov. 1977.

[Kom05] R. D. Komistek, T. R. Kane, M. Mahfouz, J. a. Ochoa, and D. a. Dennis, “Knee mechanics: A review of past and present techniques to determine in vivo loads,” *J. Biomech.*, vol. 38, no. 2, pp. 215–228, 2005.

[Kon07] R. Konno, M. Mitsui, and H. Kuwano, “A highly sensitive strain sensor using surface acoustic wave and itevaluation for wireless batteryless sensor network,” *Sensors*, 2007, pp. 796–799.

[Kou00a] D. Kouzoudis and C. A. Grimes, “Remote query fluid-flow velocity measurement using magnetoelastic thick-film sensors (invited),” *J. Appl. Phys.*, vol. 87, no. 9, p. 6301, 2000.

[Kou00b] D. Kouzoudis and C. Grimes, “The frequency response of magnetoelastic sensors to stress and atmospheric pressure,” *Smart Mater. Struct.*, vol. 9, no. 6, pp. 885–889, Dec. 2000.

[Koy14] H. C. Koydemir, H. Kulah, and C. Ozgen, “Solvent compatibility of parylene C film layer,” *J. Microelectromechanical Syst.*, vol. 23, no. 2, pp. 298–307, 2014.

[Kro12] J. Kroh, F. Cros, and C. Courcimault, “Strain monitoring system and apparatus,” United States patent 8278941, 2012.

[Kur05] E. Kurnaz, A. Kubaloglu, Y. Yilmaz, A. Koytak, and Y. Özertürk, "The effect of adjunctive Mitomycin C in Ahmed glaucoma valve implantation," *Eur. J. Ophthalmol.*, vol. 15, no. 1, pp. 27–31, 2005.

[Kwa96] M. K. Kwak, "Hydroelastic vibration of rectangular plates," *J. Appl. Mech.*, vol. 63, no. 1, p. 110, 1996.

[Law09] S. K. Law, K. Shih, D. H. Tran, A. L. Coleman, and J. Caprioli, "Long-term outcomes of repeat vs initial trabeculectomy in open-angle glaucoma," *Am. J. Ophthalmol.*, vol. 148, no. 5, pp. 685–695.e1, 2009.

[Led12] E. H. Ledet, D. D'Lima, P. Westerhoff, J. A. Szivek, R. A. Wachs, and G. Bergmann, "Implantable sensor technology: from research to clinical practice," *J. Am. Acad. Orthop. Surg.*, vol. 20, no. 6, pp. 383–92, Jun. 2012.

[Lee07] H.-S. Lee, C. Cho, and M.-W. Cho, "Magnetostrictive micro mirrors for an optical switch matrix," *Sensors*, vol. 7, no. 10, pp. 2174–2182, Oct. 2007.

[Lee14] J. W. Lee, W. Y. Park, E. A. Kim, and I. H. Yun, "Tissue response to implanted Ahmed glaucoma valve with adjunctive amniotic membrane in rabbit eyes," *Ophthalmic Res.*, vol. 51, no. 3, pp. 129–39, Jan. 2014.

[Lei06] M. Lei, A. Baldi, E. Nuxoll, R. A. Siegel, and B. Ziaie, "A hydrogel-based implantable micromachined transponder for wireless glucose measurement," *Diabetes Technol. Ther.*, vol. 8, no. 1, pp. 112–122, 2006.

[Leo10] R. Leonardi, A. Cutrera, and E. Barbato, "Rapid maxillary expansion affects the spheno-occipital synchondrosis in youngsters a study with low-dose computed tomography," *Angle Orthod.*, vol. 80, pp. 106–110, 2010.

[Les89] J. C. Lesho and A. F. Hogrefe, "Ingestible size continuously transmitting temperature monitoring pill," United States patent 4844076, 1989.

[Li09] P.-Y. Li, T. K. Givrad, D. P. Holschneider, J.-M. I. Maarek, and E. Meng, "A parylene MEMS electrothermal valve," *J. Microelectromechanical Syst.*, vol. 18, no. 6, pp. 1184–1197, Dec. 2009.

[Lia07] C. Liang, "Development of bulk-scale and thin film magnetostrictive sensor," Ph.D. dissertation, Auburn University, Auburn, AL, 2007.

[Lig78] J. Lighthill, "Acoustic streaming", *J. Sound Vibration*, vol. 61, no. 3, pp. 391-418, 1978.

[Lim98] K. S. Lim, B. D. Allan, A. W. Lloyd, A. Muir, and P. T. Khaw, "Glaucoma drainage devices; past, present, and future," *Br. J. Ophthalmol.*, vol. 82, no. 9, pp. 1083–9, Sep. 1998.

[Liu10] W. Liu, X. Jia, F. Wang, and Z. Jia, "An in-pipe wireless swimming microrobot driven by giant magnetostrictive thin film," *Sensors Actuators A Phys.*, vol. 160, no. 1–2, pp. 101–108, May 2010.

[Liu13] Y. Liu, J. Shen, W. Kainz, S. Qian, W. Wu, and J. Chen, "Numerical investigations of MRI RF field induced heating for external fixation devices," *Biomed. Eng. Online*, vol. 12, p. 12, Jan. 2013.

[Liv81] J. Livingston and W. Morris, "SEM studies of magnetic domains in amorphous ribbons," *IEEE Trans. Magn.*, vol. 17, no. 6, pp. 2624–2626, Nov. 1981.

[Liv82] J. D. Livingston, "Magnetomechanical properties of amorphous metals," *Phys. Status Solidi*, vol. 70, no. 2, pp. 591–596, Apr. 1982.

[Loe77] G. E. Loeb, A. E. Walker, S. Uematsu, and B. W. Konigsmark, "Histological reaction to various conductive and dielectric films chronically implanted in the subdural space.," *J. Biomed. Mater. Res.*, vol. 11, no. 2, pp. 195–210, 1977.

[Loe88] K. U. Loeffler and J. L. Jay, "Tissue response to aqueous drainage in a functioning Molteno implant," *Br. J. Ophthalmol.*, vol. 72, no. 1, pp. 29–35, 1988.

[Loh07] K. J. Loh, J. P. Lynch, and N. A. Kotov, "Passive wireless strain and pH sensing using carbo nanotube-gold nanocomposite thin films," *The 14th International Symposium on: Smart Structures and Materials & Nondestructive Evaluation and Health Monitoring. International Society for Optics and Photonics*, 2007, vol. 6529, p. 652919.

[Luo11] Z. Luo, M. Kaye, C. Diduch, and L. Chang, "Frequency measurement using a frequency locked loop," *IEEE Energy Convers. Congr. Expo.*, no. 1, pp. 917–921, 2011.

[Mac07] P. J. Mackenzie, R. M. Schertzer, and C. M. Isbister, "Comparison of silicone and polypropylene Ahmed glaucoma valves?: two-year follow-up," *Can. J. Ophthalmol.*, vol. 42, no. 2, pp. 227–232, 2007.

[Mas90] T. Masaki, K. Kawata, and T. Masuzawa, "Micro electro-discharge machining and its applications," *Proceedings of IEEE International Workshop on Micro Electro Mechanical Systems*, 1990, pp. 21–26.

[Med00] Medtronic Inc., "Synchromed II infusion pump." [Online]. Available: http://professional.medtronic.com/pt/neuro/itb/prod/synchromed-ii/features-specifications/index.htm. Accessed: Oct 12, 2015.

[Met00] Metglas Inc., "Magnetic Alloy 2826MB (nickel-based) Technical Bulletin." [Online]. Available: http://www.metglas.com. Accessed: Apr 26, 2015.

[Mig86] C. Migdal and R. Hitchings, "Control of chronic simple glaucoma with primary medical, surgical and laser treatment," *Trans. Ophthalmol. Soc. U. K.*, vol. 105, no. 6, pp. 653–6, Jan. 1986.

[Min87] D. S. Minckler, A. Shammas, M. Wilcox, and T. E. Ogden, "Experimental studies of aqueous filtration using the Molteno implant," *Trans. Am. Ophthalmol. Soc.*, vol. 85, pp. 368–92, Jan. 1987.

[Mol69] A. C. Molteno, “New implant for drainage in glaucoma. Animal trial,” *Br. J. Ophthalmol.*, vol. 53, no. 3, pp. 161–8, Mar. 1969.

[Mol03] A. C. B. Molteno, M. Fucik, A. G. Dempster, and T. H. Bevin, “Otago Glaucoma Surgery Outcome Study: factors controlling capsule fibrosis around Molteno implants with histopathological correlation,” *Ophthalmology*, vol. 110, no. 11, pp. 2198–206, Nov. 2003.

[Mou09] D. E. Mouzakis, D. Dimogianopoulos, and D. Giannikas, “Contact-free magnetoelastic smart microsensors with stochastic noise filtering for diagnosing orthopedic implant failures,” *IEEE Trans. Ind. Electron.*, vol. 56, no. 4, pp. 1092–1100, Apr. 2009.

[Ner14] J. M. Nervina, S. D. Kapila, and C. F. Mir, “Assessment of maxillary transverse deficiency and treatment outcomes by cone-beam computed tomography,” Cone Beam Computed Tomography in Orthodontics: Indications, Insights and Innovations, S. Kapila, Ed., Ames, IA: Wiley Blackwell, 2014, pp. 383–409.

[Nil97] S. F. Nilsson, “The uveoscleral outflow routes,” *Eye (London)*, vol. 11, pp. 149–54, Jan. 1997.

[O’De82] T. H. O’Dell, “Measurement of magnetomechanical coupling factor in amorphous ribbons,” *Phys. Status Solidi*, vol. 74, p. 565, 1982.

[Odu96] H. Oduncu and T. Meydan, “A novel method of monitoring biomechanical movements using the magnetoelastic effect,” *J. Magn. Magn. Mater.*, vol. 160, pp. 233–236, Jul. 1996.

[Oes09] N. P. Oess, B. Weisse, and B. J. Nelson, “Magnetoelastic strain sensor for optimized assessment of bone fracture fixation,” *IEEE Sens. J.*, vol. 9, no. 8, pp. 961–968, Aug. 2009.

[Ong02] K. G. Ong and C. Grimes, “Tracking the harmonic response of magnetically-soft sensors for wireless temperature, stress, and corrosive monitoring,” *Sens. Actuators. A. Phys.*, vol. 101, no. 1–2, pp. 49–61, Sep. 2002.

[Pap10] M. E. Papadaki, M. J. Troulis, J. Glowacki, and L. B. Kaban, “A minipig model of maxillary distraction osteogenesis,” *J. Oral Maxillofac. Surg.*, vol. 68, no. 11, pp. 2783–2791, 2010.

[Par02] J. a T. C. Parker, X. F. Walboomers, J. W. Von Den Hoff, J. C. Maltha, and J. a. Jansen, “Soft tissue response to microtextured silicone and poly-L-lactic acid implants: Fibronectin pre-coating vs. radio-frequency glow discharge treatment,” *Biomaterials*, vol. 23, no. 17, pp. 3545–3553, 2002.

[Pay09] J. Payne, K. D. Song, S. Y. Yang, J. Kim, Y. Park, and S. H. Choi, “Wireless power transmission for medical applications,” *Proceedings of SPIE*, 2009, p. 72910X–72910X–9.

[Phi90] W. Philipp, G. Klima, and K. Miller, “Clinicopathological findings 11 months after implantation of a functioning aqueous-drainage silicone implant,” *Graefe’s Arch. Clin. Exp. Ophthalmol.*, vol. 228, no. 5, pp. 481–486, 1990.

[Pic96] G. J. Picha and R. F. Drake, “Pillared-surface microstructure and soft-tissue implants: Effect of implant site and fixation,” *J. Biomed. Mater. Res.*, vol. 30, no. 3, pp. 305–312, 1996.

[Pra95] J. A. Prata, R. C. R. Santos, L. LaBree, and D. S. Minckler, “Surface area of glaucoma implants and perfusion flow rates in rabbit eyes,” *J. Glaucoma*, vol. 4, pp. 274–280, 1995.

[Qua95] E. Quandt and K. Seemann, “Fabrication of giant magnetostrictive thin film actuators,” *Proceedings IEEE Micro Electro Mechanical Systems*, 1995, p. 273.

[Qui06] H. A. Quigley and A. T. Broman, “The number of people with glaucoma worldwide in 2010 and 2020,” *Br. J. Ophthalmol.*, vol. 90, no. 3, pp. 262–7, Mar. 2006.

[Raa98] I. Raad, “Intravascular-catheter-related infections,” *Lancet*, vol. 351, no. 9106, pp. 893–898, Mar. 1998.

[Rah10] S. Rahimi, E. H. Sarraf, G. K. Wong, and K. Takahata, “Implantable drug delivery device using frequency-controlled wireless hydrogel microvalves,” *Biomed. Microdevices*, vol. 13, no. 2, pp. 267–277, Dec. 2010.

[Ram95] M. L. V. Ramires, C. A. Nieto de Castro, Y. Nagasaka, A. Nagashima, M. J. Assael, and W. A. Wakeham, “Standard reference data for the thermal conductivity of water,” *J. Phys. Chem. Ref. Data*, vol. 24, no. 3, p. 1377, 1995.

[Raa83] D. Raskin and C. H. Smith, “Applications of amorphous metals: progress and prospects,” Amorphous Metallic Alloys, F. E. Luborsky, Ed., London: Butterworths, 1983, p. 397.

[Rec95] A. F. von Recum and T. G. van Kooten, “The influence of micro-topography on cellular response and the implications for silicone implants,” *J. Biomater. Sci. Polym. Ed.*, vol. 7, no. 2, pp. 181–198, 1995.

[Res04] S. Resnikoff, D. Pascolini, D. Etya’ale, I. Kocur, R. Pararajasegaram, G. P. Pokharel, and S. P. Mariotti, “Global data on visual impairment in the year 2002,” *Bull. World Health Organ.*, vol. 82, no. 11, pp. 844–51, Nov. 2004.

[Riz07] C. S. Rizal, “Study of magnetic anisotropy and magnetoresistance effects in ferromagnetic Co/Au multilayer films prepared by oblique incidence evaporation method,” *J. Magn. Magn. Mater.*, vol. 310, no. 2, pp. e646–e648, Mar. 2007.

[Ros10] T. G. Rosenbaum Chou, C. A. Petti, J. Szakacs, and R. D. Bloebaum, “Evaluating antimicrobials and implant materials for infection prevention around transcutaneous osseointegrated implants in a rabbit model,” *J. Biomed. Mater. Res. - Part A*, vol. 92, no. 3, pp. 942–952, 2010.

[Ros03] E. A. Ross, C. D. Batich, W. L. Clapp, J. E. Sallustio, and N. C. Lee, “Tissue adhesion to bioactive glass-coated silicone tubing in a rat model of peritoneal dialysis catheters and catheter tunnels,” *Kidney Int.*, vol. 63, no. 2, pp. 702–708, 2003.

[Sad98] J. E. Sader, “Frequency response of cantilever beams immersed in viscous fluids with applications to the atomic force microscope,” *J. Appl. Phys.*, vol. 84, no. 1, p. 64, 1998.

[Sau12] S. Sauer, U. Marschner, B. Adolphi, B. Clasbrummel, and W.-J. Fischer, “Passive wireless resonant Galfenol sensor for osteosynthesis plate bending measurement,” *IEEE Sens. J.*, vol. 12, no. 5, pp. 1226–1233, May 2012.

[Sav88] H. T. Savage and C. Adler, “Effects of magnetostriction in amorphous ferromagnets,” *Mater. Sci. Eng.*, vol. 99, pp. 13–18, 1988.

[Sch88] E. M. Schmidt, J. S. McIntosh, and M. J. Bak, “Long-term implants of Parylene-C coated microelectrodes,” *Med. Biol. Eng. Comput.*, vol. 26, no. 1, pp. 96–101, 1988.

[Sch01] P. H. Schiffman and O. C. Tuncay, “Maxillary expansion: A meta analysis,” *Clin. Orthod. Res.*, vol. 4, pp. 86–96, 2001.

[Sch15] I. Schmale, B. Gleich, J. Rahmer, C. Bontus, J. Schmidt, and J. Borgert, “MPI Safety in the View of MRI Safety Standards,” *IEEE Trans. Magn.*, vol. 51, no. 2, pp. 18–21, 2015.

[She07] C. H. Sherman and J. L. Butler, *Transducers and Arrays for Underwater Sound*. Berlin: Springer, 2007, pp. 554–555.

[She10] W. Shen, Z. Zhang, S. Horikawa, A. Zhang, J. Teng, L. C. Mathison, and B. A. Chin, “Time domain characterization of magnetoelastic sensors: A pulse method for resonance frequency determination,” *Rev. Sci. Instrum.*, vol. 81, no. 8, p. 084702, Aug. 2010.

[Shi99] K.-H. Shin, M. Inoue, and K.-I. Arai, “Strain sensitivity of highly magnetostrictive amorphous films for use in microstrain sensors,” *J. Appl. Phys.*, vol. 85, no. 8, p. 5465, 1999.

[Sil12] R. M. Silva, G. Chesini, C. J. Gouveia, A. B. Lobo Ribeiro, O. Frazão, C. M. B. Cordeiro, and P. A. S. Jorge, “Magnetic field sensor with Terfenol-D thin-film coated FBG,” *International Conference on Optical Fiber Sensors*, 2012, vol. 8421, p. 84213C.

[Sit11] A. J. Sit and J. W. McLaren, “Measurement of episcleral venous pressure,” *Exp. Eye Res.*, vol. 93, no. 3, pp. 291–8, Sep. 2011.

[Sta05] M. S. Stay, T. Pan, J. D. Brown, B. Ziaie, and V. H. Barocas, “Thin-film coupled fluid-solid analysis of flow through the Ahmed glaucoma drainage device,” *J. Biomech. Eng.*, vol. 127, no. 5, p. 776, May 2005.

[Ste12] J. Stembirek, M. Kyllar, I. Putnova, L. Stehlik, and M. Buchtova, “The pig as an experimental model for clinical craniofacial research,” *Lab. Anim.*, vol. 46, pp. 269–279, 2012.

[Tak02] K. Takahata and Y. B. Gianchandani, “Batch mode micro-electro-discharge machining,” *J. Microelectromechanical Syst.*, vol. 11, no. 2, pp. 102–110, Apr. 2002.

[Tan12] E. L. Tan, A. J. DeRouin, and K. G. Ong, “Magnetoelastic-harmonic stress sensors with tunable sensitivity,” *IEEE Sens. J.*, vol. 12, no. 6, pp. 1878–1883, Jun. 2012.

[Tan13] J. Tang, S. R. Green, and Y. B. Gianchandani, “Miniature wireless magnetoelastic resonant motor with frequency selectable bidirectional rotation,” *J. Microelectromechanical Syst.*, vol. 22, no. 3, pp. 730–738, Jun. 2013.

[Tan14] J. Tang, S. R. Green, and Y. B. Gianchandani, “Scalable, high-performance magnetoelastic tags using frame-suspended hexagonal resonators,” *J. Micromechanics Microengineering*, vol. 24, no. 6, p. 065006, Jun. 2014.

[TasA10] V. Tas, S. Olcum, M. D. Aksoy, and A. Atalar, “Reducing anchor loss in micromechanical extensional mode resonators,” *IEEE Trans. Ultrason. Ferroelectr. Freq. Control*, vol. 57, no. 2, pp. 448–454, 2010.

[Tei12] S. H. Teixeira, L. M. Doi, A. L. De Freitas Silva, K. D. Silva, Â. T. Paes, F. S. Higa, M. Mendonça, J. A. Prata, and A. Paranhos, “Silicone Ahmed glaucoma valve with and without intravitreal triamcinolone acetonide for neovascular glaucoma,” *J. Glaucoma*, vol. 21, no. 5, pp. 342–348, 2012.

[The13] M. Theodor, D. Ruh, J. Fiala, K. Förster, C. Heilmann, Y. Manoli, F. Beyersdorf, H. Zappe, and A. Seifert, “Subcutaneous blood pressure monitoring with an implantable optical sensor,” *Biomed. Microdevices*, vol. 15, no. 5, pp. 811–20, Oct. 2013.

[Thi11] H. Thieme, L. Choritz, C. Hofmann-Rummelt, U. Schloetzer-Schrehardt, and U. B. Kottler, “Histopathologic findings in early encapsulated blebs of young patients treated with the ahmed glaucoma valve,” *J. Glaucoma*, vol. 20, no. 4, pp. 246–51, 2011.

[Tho82] J. V Thomas, R. J. Simmons, and C. D. Belcher, “Argon laser trabeculoplasty in the presurgical glaucoma patient,” *Ophthalmology*, vol. 89, no. 3, pp. 187–97, Mar. 1982.

[Tit12] I. R. Titze, S. A. Klemuk, and X. Lu, “Adhesion of a monolayer of fibroblast cells to fibronectin under sonic vibrations in a bioreactor,” *Ann. Otol. Rhinol. Laryngol.*, vol. 121, no. 6, pp. 364–374, 2012.

[Tor78] E. Torok and G. Hausch, “Magnetoelastic effects of some ferromagnetic metallic glasses,” *Rapidly Quenched Metals III*, 1978, pp. 105–108.

[Tor10] C. B. Toris, “Pharmacotherapies for Glaucoma,” *Curr. Mol. Med.*, vol. 10, no. 9, pp. 824–840, Dec. 2010.

[Tra08] S. Traxler, J. Kosel, H. Pfützner, E. Kaniusas, L. Mehnen, and I. Giouroudi, “Contactless flow detection with magnetostrictive bilayers,” *Sensors Actuators A Phys.*, vol. 142, no. 2, pp. 491–495, Apr. 2008.

[Tru90] G. A. Truskey and J. S. Pirone, “The effect of fluid shear stress upon cell adhesion to fibronectin-treated surfaces,” *J. Biomed. Mater. Res.*, vol. 24, no. 10, pp. 1333–1353, 1990.

[Uch03] K. Uchino, “Introduction to piezoelectric actuators and transducers,” *5th Int. Conf. Intelligent Mat.*, State Park, PA, 2003.

[Vis13] A. Viswanath, S. R. Green, J. Kosel, and Y. B. Gianchandani, “Metglas–Elgiloy bi-layer, stent cell resonators for wireless monitoring of viscosity and mass loading,” *J. Micromechanics Microengineering*, vol. 23, no. 2, p. 025010, Feb. 2013.

[Vla11] E. Vlaisavljevich, L. P. Janka, K. G. Ong, and R. M. Rajachar, “Magnetoelastic materials as novel bioactive coatings for the control of cell adhesion,” *IEEE Trans. Biomed. Eng.*, vol. 58, no. 3, pp. 698–704, Mar. 2011.

[Wan11] Z. Wang, R. Mills, H. Luo, X. Zheng, W. Hou, L. Wang, S. I. Brown, and A. Cuschieri, “A micropower miniature piezoelectric actuator for implantable middle ear hearing device,” *IEEE Trans. Biomed. Eng.*, vol. 58, no. 2, pp. 452–8, Mar. 2011.

[Wat88] J. C. Watkins and E. Fukushima, “High-pass bird-cage coil for nuclear-magnetic resonance,” *Rev. Sci. Instrum.*, vol. 59, no. 6, p. 926, 1988.

[Wes09] P. Westerhoff, F. Graichen, A. Bender, A. Rohlmann, and G. Bergmann, “An instrumented implant for in vivo measurement of contact forces and contact moments in the shoulder joint,” *Med. Eng. Phys.*, vol. 31, no. 2, pp. 207–13, Mar. 2009.

[Wil07] M. Wilcox and O. A. Kadri, “Force and geometry determine structure and function of glaucoma filtration capsules,” *Ophthalmologica*, vol. 221, no. 4, pp. 238–43, Jan. 2007.

[Woo07] T. O. Woods, “Standards for medical devices in MRI: present and future,” *J. Magn. Reson. Imaging*, vol. 26, no. 5, pp. 1186–9, Nov. 2007.

[Yos05] N. Yoshizawa, I. Yamamoto, and Y. Shimada, “Magnetic field sensing by an electrostrictive/magnetostrictive composite resonator,” *IEEE Trans. Magn.*, vol. 41, no. 11, pp. 4359–4361, Nov. 2005.

[Zen02] K. Zeng, K. G. Ong, C. Mungle, and C. A. Grimes, “Time domain characterization of oscillating sensors: Application of frequency counting to resonance frequency determination,” *Rev. Sci. Instrum.*, vol. 73, no. 12, p. 4375, 2002.

[Zha14] B. G. X. Zhang, D. E. Myers, G. G. Wallace, M. Brandt, and P. F. M. Choong, “Bioactive coatings for orthopaedic implants-recent trends in development of implant coatings,” *Int. J. Mol. Sci.*, vol. 15, no. 7, pp. 11878–11921, 2014.

[Zim65] J. F. Zimring and R. J. Isaacson, “Forces produced by rapid maxillary expansion III. Forces present during retention,” *Angle Orthod.*, vol. 35, no. 3, pp. 178–186, 1965.

[Zor10] A. Zorab, “The reduction of tension in chronic glaucoma,” *The Ophthalmoscope*, vol. 10, pp. 258–261, 1910.

[Zuc13] G. Zuccati, S. Casci, T. Doldo, and C. Clauser, “Expansion of maxillary arches with crossbite: A systematic review of RCTs in the last 12 years,” *Eur. J. Orthodontics,* vol. 35. pp. 29–37, 2013.